UNIVERSITY OF CALIFORNIA SAN DIEGO

Detailed Finite Element of a Type II Bridge Column Shaft Reinforced with High-Strength Steel.

A Thesis submitted in partial satisfaction of the requirements

for the degree Master of Science

in

Structural Engineering

by

Valentina Alejandra Vásquez

Committee in charge:

Professor José I. Restrepo, Chair
Professor Joel P. Conte
Professor Chia-Ming Uang

2019

The Thesis of Valentina Alejandra Vásquez is approved, and it is acceptable in quality and form for publication on microfilm and electronically:

_____

_____

_____

Chair

University of California San Diego

2019

DEDICATION

To Ricardo,

for his constant support and encouragement.

TABLE OF CONTENTS

LIST OF SYMBOLS

μ_Δ	Displacement ductility
w_d	Critical compressive displacement
m	Frictional strength in Menétrey – Willam triaxial failure criteria
c	Cohesive strength in Menétrey – Willam triaxial failure criteria
e	Excentricity parameter out of roundness
$\varepsilon^{e,p,f}$	Elastic, plastic or fracture strain vector
E	Elastic stiffness vector
F^f	Failure surface
L_t	Element size projected in the direction of crack
f_c'	Uniaxial compressive strength
f_t'	Uniaxial tensile strength
ξ	Hydrostatic stress invariant
ρ	Deviatoric stress invariant
θ	Deviatoric stress angle
G_{fc}	Compressive fracture energy
G_{ft}	Tensile fracture energy
c_{ts}	Tension Stiffening Parameter ATENA ®
s_F	Shear Factor Parameter ATENA ®
f_U	Unloading Parameter ATENA ®
β	Direction of plastic flow ATENA ®

LIST OF ABBREVIATIONS

FEA	Finite Element Analysis
LVDT	Linear variable differential transformers
Caltrans	California Department of Transportation
UCSD	University of California San Diego
FE	Finite Element
DOT	Day of testing
RC	Reinforced concrete
FER	Fixed end rotation
PH	Plastic Hinge

LIST OF FIGURES

LIST OF TABLES

ACKNOWLEDGMENTS

I want to acknowledge Professor José I. Restrepo for his support as the chair of my committee. I would like to especially thank him for his leap of faith in trusting me with this study. His guidance made the pursuit of the master degree more valuable.

I would like to thank my friends Carolina Jauregui, Rodrigo Carreño, Douglas De Aquino, Divya Sharma, and all the others who made this journey enjoyable. I want to especially thank Koorosh Lotfizadeh who provided not only part of his valuable research, but for all his support and time spent answering my innumerable questions.

I want to thank Ricardo Bustamante for his constant encouragement, support, and patience. His advice has always helped me to become a better person.

I am grateful to Dr. Jan Cervenka, who invested his time helping in the developed and understanding of the analytical simulation.

The work here presented was supported by funding from the California Department of Transportation (Caltrans), contract number 65A0562. I am grateful for their financial support.

Finally, I want to thank the members of my committee for the time invested.

ABSTRACT OF THE THESIS

Detailed Finite Element of a Type II Bridge Column Shaft Reinforced with High-Strength Steel.

by

Valentina Alejandra Vásquez

Master of Science in Structural Engineering

University of California San Diego, 2019

Professor José I. Restrepo, Chair

The use of high-strength steel reinforcement in seismic design of bridges is currently under investigation. Several benefits will come from its use, which includes a reduction in the construction time, a reduction in congestion and cost savings, among others.

Lotfizadeh (2019) performed an experimental work at the University of California San Diego to study the use of large-diameter high-strength steel reinforcement in earthquake resisting

bridge elements. Part of the study considered a quasi-static test of a full-scale bridge column extending into a Type II shaft (enlarged diameter shaft) all reinforced with high-strength ASTM A706 Grade 80 reinforcement.

Data obtained from the study was used through this research to calibrate a detailed nonlinear finite element model. For this purpose, continuum 3D elements with fracture-plastic constitutive material law were used to represent the concrete and line elements with uniaxial constitutive materials to characterize the axial stress-strain response of high-strength steel reinforcement.

Calibration of the constitutive laws with the experimental data gave a good prediction of the overall and local behavior. The analysis was able to capture the opening and closure of flexural cracks by providing a lower limit to the tensile concrete stress, with smear tension stiffening.

The numerical simulation's state of the art can fit the overall response of analytical models with a pretest, but to our knowledge, the distribution of the spread plasticity is usually not addressed or shown. In this research, a comprehensive study of both responses is addressed. Even when the model captured the overall structural behavior, the spread plasticity did not match with the experimental data as well as it did with the overall response.

INTRODUCTION

Nowadays non-linear finite element analyses are often used to predict the behavior of single elements or entire structures. With constant improvements and updates, the capabilities of finite element analysis (FEA) software are regularly increasing, adding the necessary tools and settings to incorporate a broad spectrum of behaviors. A wide range of material models are available, from simplified and straightforward to complex and very sophisticated representations. However, one may ask if the predicted behavior observed from the analysis would represent well the actual response of a structure and its components, particularly when subjected to cyclic reversals.

Understanding how material models work is crucial. Many parameters are set to reflect these specific behaviors. Therefore, researchers should perform a calibration of the material model parameters prior to implementing them in the desired model. Simply assuming as a fact that the numerical simulation provides a fair prediction of the behavior reflects poor practice.

An experiment was performed at the University of California San Diego, as part of the project "*High-Strength Steel Reinforcement in Critical Regions of Earthquake-Resistant Bridge*" funded by the California Department of transportation (Caltrans) (Lotfizadeh, 2019), with a focus on columns extending into Type II shafts. A full-scale test specimen entirely reinforced with ASTM A706 Grade 80 reinforcement was designed, built and tested quasi-statically at the Charles Lee Powell Structural Laboratories. The test specimen was well instrumented with electrical-foil strain gages applied directly to the reinforcing bars, and externally mounted linear variable differential transformers (LVDT) to characterize the overall response, and observe the behavior of this new type of reinforcement.

The scope of this thesis is to develop a 3D non-linear detailed finite element model of the experiment. The model representing the test setup was done with the software ATENA® Studio from Cervenka Consulting. A comparison between the test specimen behavior and the numerical response obtained with the model is made, as well as parametric analyses to determine the relevance of the material parameters in the response obtained with the FEA.

CHAPTER 1: LITERATURE REVIEW

The literature review was focused on researches that used solid finite elements to described reversed cyclic loading of tests conducted quasi-statically or dynamically. Three studies will be reviewed, which were done by Rashid et al. (2000), Murcia-Delso (2013) and Moharrami et al. (2017).

1.1 ANACAP - RASHID J., DAMERON R. & DOWELL R.

The authors (Rashid et al., 2000) used the routine ANACAP within ABAQUS to assess the applicability of continuum based methods to predict the behavior of reinforced concrete structures.

The concrete model in ANACAP considers the tensile behavior with a smeared crack concept with no healing of cracks upon closure; the compression behavior accounts for softening. The yield surface used by the material is a function of the first and second invariants of the stress tensor and the effective stress position on the stress-strain curve. Figure 1–1(a) shows the possible stress-strain paths that the compression curve can take under cyclic loading. The model accounts for shear behavior by reducing the shear modulus as a function of the crack opening strain, the deficiencies of using such a model are corrected by adding a sub-model for shear retention in the open-crack regime (when the model over-estimates) and shear-shedding in the closed crack regime (when the model under-estimates).

For the steel model, a bond behavior is introduced to account for bond-slip. The model used is the one proposed by Dameron (1995), with a Priestley bond-failure criterion. Figure 1–1

(b) shows how the rooted bond-slip model changes the failure surface of the unloading and reloading curves when the local bond-failure criterion is met.

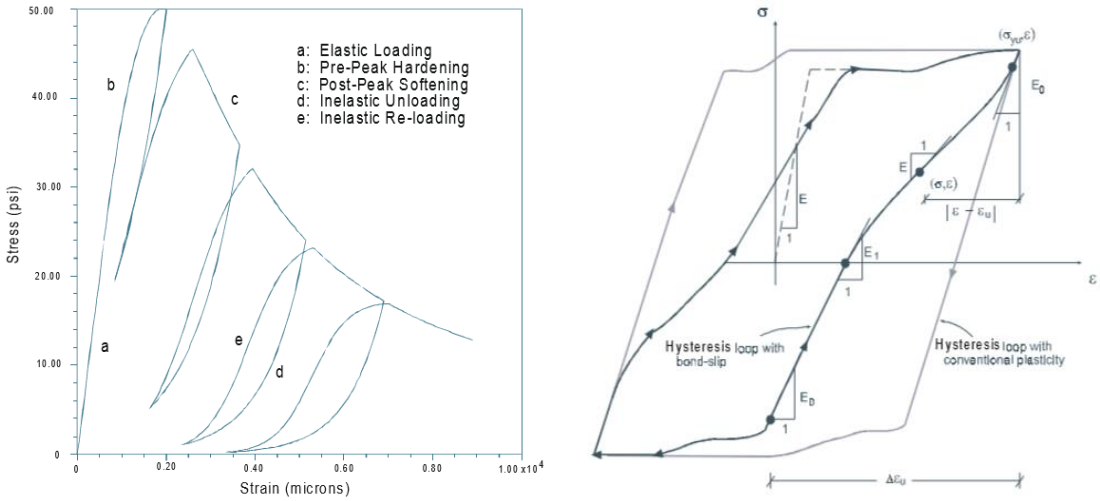

Figure 1–1: (a)Analytical cyclic stress-strain curve, (b) Rebar bond-slip model (Rashid et al., 2000).

The authors used dynamic and quasi-static experiments to review software capabilities. Hines et al. (1999) at UC San Diego performed the quasi-static tests used, and the dynamic experiment was part of the CAMUS International Benchmark.

The quasi-static test corresponded of a composite reinforced concrete wall with confined circular columns at the ends. The analysis performed used half-symmetry of the test setup, with 3D solid elements. As input parameters of the materials were the design concrete compressive strength and the stress-strain measured curves of the reinforcement. Figure 1–2 shows the results of the model and test for ductility ratios of one and six. The predictions of the program match well the results of the experiment, as well as the failure mode (fracture of the vertical reinforcement).

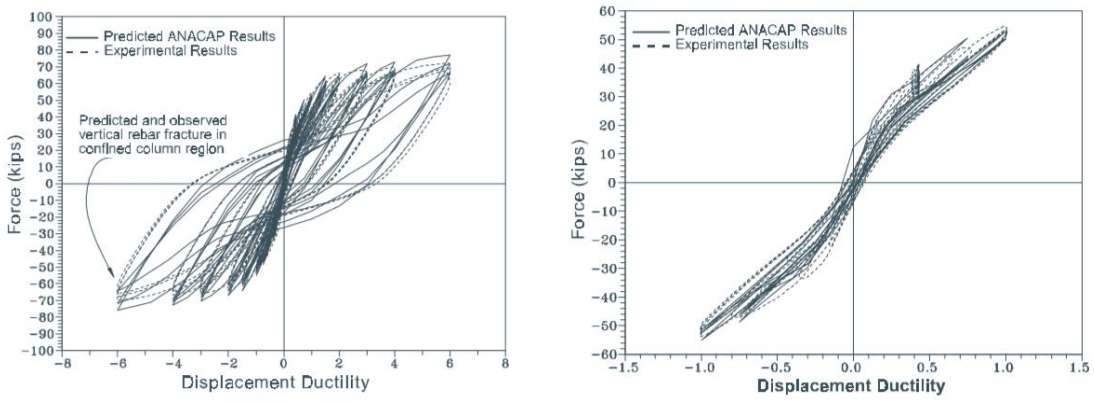

Figure 1–2: Quasi-static model and test hysteresis loops for ductility ratios of one and six (Rashid et al., 2000).

The authors discuss the results of two shaking table tests. The first corresponds to a five-story two-cantilever wall connected by floors at each level and the bottom by a heavily reinforced footing. The structure was 1/3 scale, design to the PS92 French code and tested at the Saclay French shaking table. The model used half symmetry, with 3D solid elements, and suggested material properties. Additionally, the shear-shedding formulation of the program was activated. The model also accounted for the geometry and mass of the shaking table. Figure 1–3 shows the time-history responses of the test and the prediction of the model, which fits quite well. Also, the model predicted the time and mode of failure.

The second test comprised a 1/10 scaled prestressed reactor containment. The structure was subjected to a series of design level earthquakes with increasing amplitude motion until failure. The experiments were performed at the Tadotsu Engineering Laboratory at Japan. Since the failure mode of the test was led by shear, the use of the shear stiffness for cracked concrete gave a better match of the overall behavior. Due to the comparisons of the test and model results a shear-failure criterion was developed. The criterion considers the failure of the structure when a shear strain reached 0.5% averaged in any cross-section. Also, an essential finding of the

analytical model was that assuming a fixed value of damping would give poor predictions. The authors developed a crack-consistent damping model to overcome this.

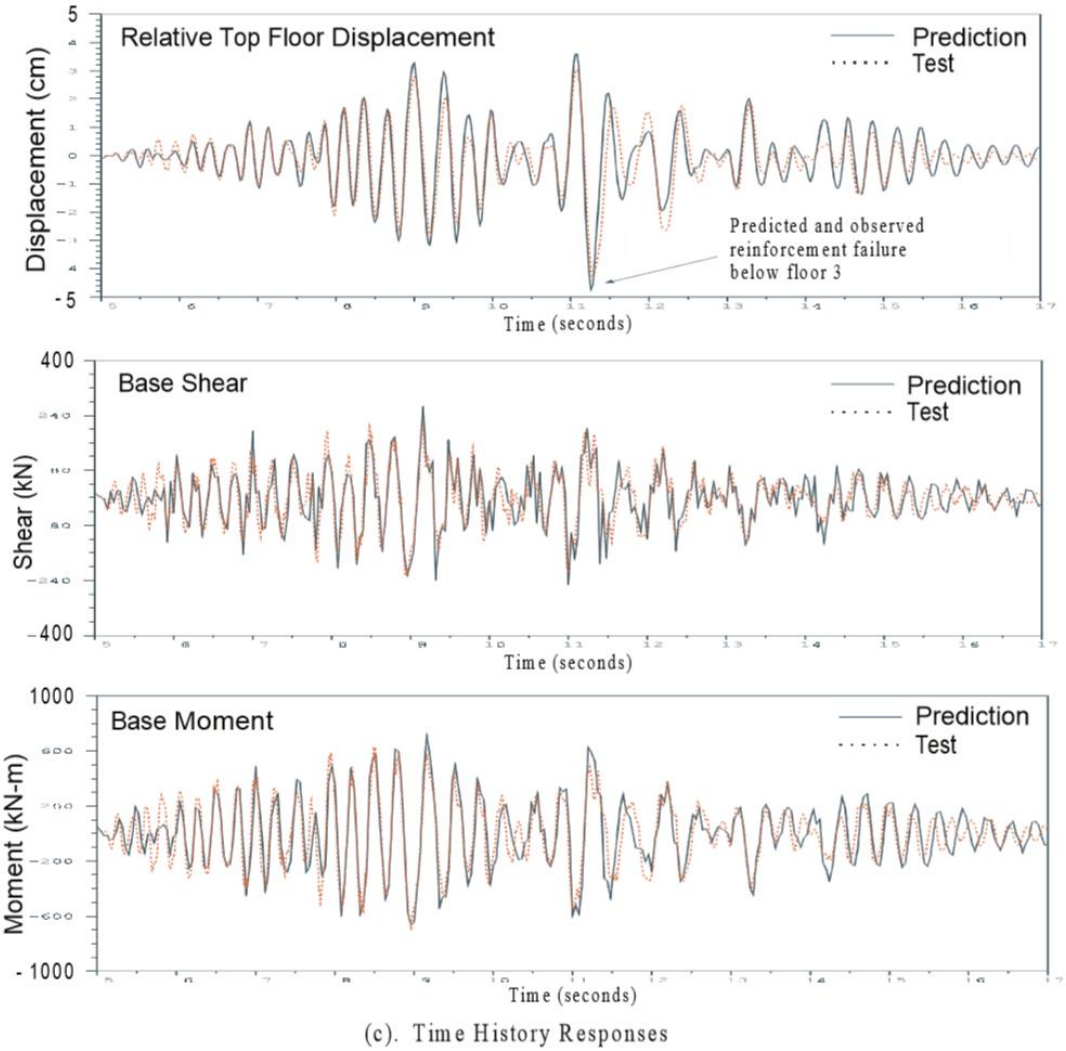

Figure 1–3: Dynamic model and test time-history responses (Rashid et al., 2000).

1.2 ABAQUS - MURCIA DELSO J.

Murcia-Delso (2013) did his doctoral dissertation focusing on bond-slip and development of longitudinal reinforcing bars in enlarges pile shafts, which is the subject of study. For this, the author used the finite element program ABAQUS to model large-scale tests of column-shaft assemblies.

The model considered a symmetry plane. Continuum 3D elements were used for concrete; beam elements for longitudinal reinforcement, and truss elements for the transverse reinforcement. Additionally, the author created a constitutive law for a contact element between the longitudinal bars and the concrete to account for bond-slip. Truss elements considered perfect bond. Even though the steel was modeled with beam elements, the program was not able to predict the buckling of the rebar.

Continuum elements had assigned a *concrete damage plasticity model* as constitutive law. This law considers the strain tensor divided into an elastic and plastic component. The stress tensor is related to the elastic stiffness, which to account for stiffness degradation a *d* scalar parameter is introduced.

$$\sigma = E : (\varepsilon - \varepsilon^p) \tag{1.1}$$

$$E = (1 - d)E_0 \tag{1.2}$$

The constitutive law uses a yield surface of the damage plasticity model, defined as a function of the invariants I_1 and J_2.

$$F = \frac{1}{1-\alpha}\left[\alpha I_1 + \sqrt{3J_2} + \beta\left(\tilde{\varepsilon}_c^p, \tilde{\varepsilon}_t^p\right)\langle\hat{\sigma}_{max}\rangle - \gamma\langle -\hat{\sigma}_{max}\rangle\right] - c_c\left(\tilde{\varepsilon}_c^p\right) \tag{1.3}$$

Where $\langle\cdot\rangle$ are the Macaulay brackets, α and γ are constants, β and c_c are variables that depend on the equivalent compression plastic strain ($\tilde{\varepsilon}_c^p$) and equivalent tension plastic strain ($\tilde{\varepsilon}_t^p$). B is defined as follows:

$$\beta = \frac{c_c\left(\tilde{\varepsilon}_c^p\right)}{c_t\left(\tilde{\varepsilon}_c^p\right)}(1-\alpha) - (1+\alpha) \tag{1.4}$$

With $c_c\left(\tilde{\varepsilon}_c^p\right)$ and $c_t\left(\tilde{\varepsilon}_c^p\right)$ are the tensile and compressive cohesion in the yield surface. Compression and tensile uniaxial tests calibrate these variables.

The plastic potential depends on the invariants and an additional parameter ψ which represents the dilatation angle of the concrete. Then the rate of the plastic strain is given in (1.5), where $\dot{\lambda}$ is the plastic multiplier.

$$G = \sqrt{3J_2} + \frac{I_1}{3}tan(\psi) \tag{1.5}$$

$$\dot{\varepsilon}^p = \dot{\lambda}\frac{\partial G}{d\sigma} \tag{1.6}$$

The rate of the history variables is given in (1.6).

$$\dot{\tilde{\varepsilon}}_c^p = r(\hat{\bar{\sigma}}_\cdot)\widehat{\dot{\varepsilon}^p}_{max} \text{ and } \dot{\tilde{\varepsilon}}_c^p = \left(1 - r(\hat{\bar{\sigma}}_\cdot)\right)\widehat{\dot{\varepsilon}^p}_{min} \tag{1.7}$$

$$r(\hat{\bar{\sigma}}_\cdot) = \begin{cases} 0 & if\ \hat{\bar{\sigma}}_\cdot = 0 \\ \frac{\sum_{i=1}^{3}\langle\hat{\bar{\sigma}}_i\rangle}{\sum_{i=1}^{3}|\hat{\bar{\sigma}}_i|} & otherwise \end{cases} \tag{1.8}$$

With $\widehat{\dot{\varepsilon}^p}_{max} = \dot{\varepsilon}_1^p$, $\widehat{\dot{\varepsilon}^p}_{min} = \dot{\varepsilon}_3^p$, where $\dot{\varepsilon}_1^p \geq \dot{\varepsilon}_2^p \geq \dot{\varepsilon}_3^p$.

The damage parameter d used to compute the stress tensor is a function of the damage parameter in tension (d_t) and compression (d_c).

$$(1-d) = \left(1 - s_t d_c\left(\tilde{\varepsilon}_c^{\dot{p}}\right)\right)\left(1 - s_c d_t\left(\tilde{\varepsilon}_t^{\dot{p}}\right)\right) \tag{1.9}$$

$$s_t = 1 - w_t r(\hat{\bar{\sigma}}) \text{ and } s_c = 1 - w_c\left(1 - r(\hat{\bar{\sigma}})\right) \tag{1.10}$$

Where w_c and w_t control the stiffness degradation in compression and tension, and uniaxial tests in compression or tension calibrate d_c and d_t.

Figure 1–4 presents the uniaxial representation of the model.

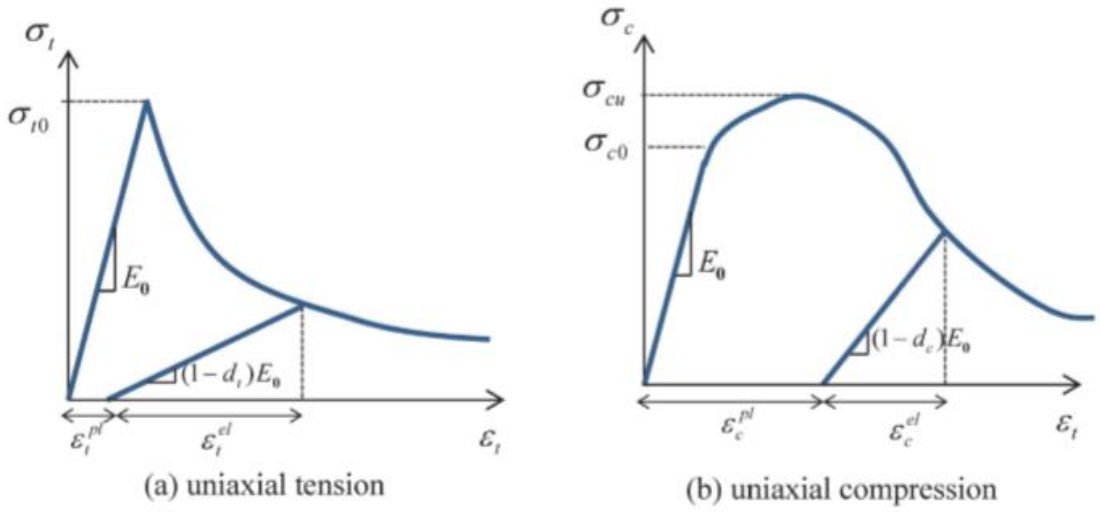

Figure 1–4: Uniaxial tension and compression in plastic damage concrete model (Murcia-Delso, 2013).

For the steel model, the author chooses to use a rate-independent elasto-plasticity model with linear kinematic hardening for the beam elements, and with exponential kinematic hardening for truss elements.

The model uses the Von Mises yield condition. Definition of the yield function and plastic flow has the same formulation given in (1.11), with σ' and α' are the deviatoric part of the stress tensor (σ) and the backstress tensor (α).

$$F(\sigma, \alpha) = \sqrt{\frac{3}{2}(\sigma' - \alpha'):(\sigma' - \alpha')} - \sigma_y \qquad (1.11)$$

The backstress tensor controls the translation of F in the stress space due to kinematic hardening.

The author, as already mentioned, developed the constitutive model for the contact element that considers the bond-slip relation. The model takes into account the normal and tangential relative displacements. The implementation can be found elsewhere (Murcia-Delso, 2013).

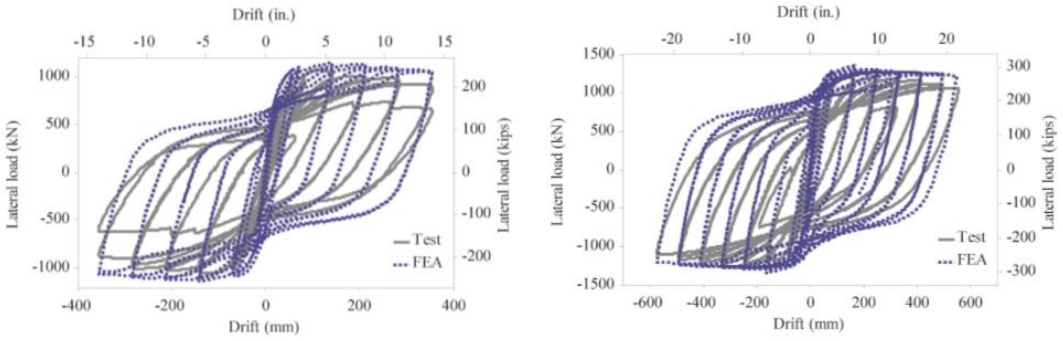

Lateral load vs. drift curves for Specimen 1

Lateral load vs. drift curves for Specimen 2

Figure 1–5: Comparison between test specimen and the analytical model of the lateral load versus displacement (Murcia-Delso, 2013).

Since the concrete model is not able to represent well the opening and closure of flexural cracks, the author provided a contact condition to the column-shaft and shaft-footing interfaces.

Figure 1–5 shows the overall behavior comparison between the analytical model and the two test specimens. The analytical model overestimated the maximum load carrying capacity by 7% and 10% for specimen one and two. The gradual drop of the load carrying capacity caused by P-delta effects was well represented. However, one of the major drawbacks of the model

prediction is the overestimation of the energy dissipation. This is mainly because the concrete model was not able to account for the open and closure of flexural cracks.

1.3 LS-DYNA - MOHARRAMI M. & KOUTROMANOS I.

Moharrami et al. (2017) implemented a constitutive model for reinforced concrete in LS-DYNA. For the concrete, it was based on a tri-axial constitutive model, and for the reinforcement steel, the model accounted for low cycle fatigue. The concrete was modeled as continuum 3D solid elements and the reinforcing bar as beam elements.

The concrete constitutive model combines an elastoplastic law with rotated smeared crack formulation, where the strain is divided into elastic, plastic and cracking strains. The yield surface is a function of the stress tensor and the hardening variable κ, that express the cumulative effect of inelastic deformation.

$$f(\{\hat{\sigma}\},\kappa) = \frac{1}{1-\alpha}\left[\alpha I_1 + r(\theta,e)\sqrt{3J_2}\right] - c_c(\kappa) = 0 \qquad (1.12)$$

Where $I_1$is the first invariant of the stress tensor, J_2 is the second deviatoric invariant. $r(\theta,e)$ describes the effect of the third deviatoric invariant, and α is a dimensionless material parameter.

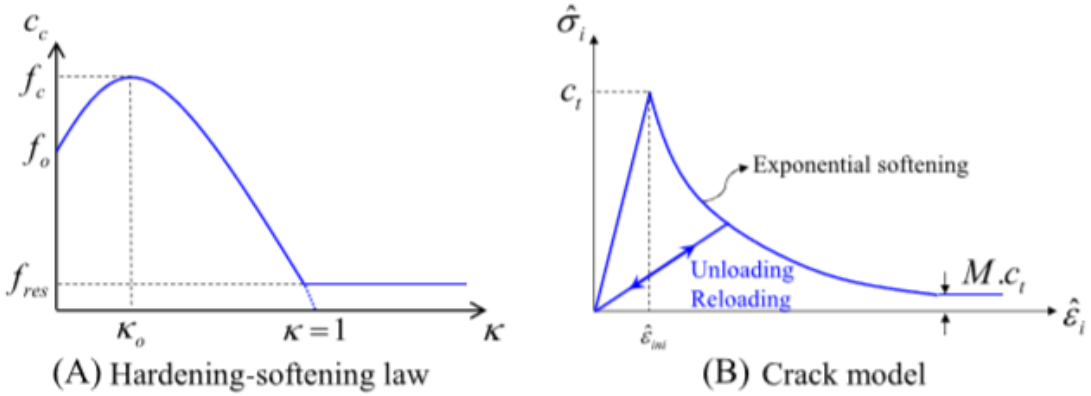

Figure 1–6: (a) Hardening-softening law. (b) Unloading direction of the crack model (Moharrami & Koutromanos, 2017).

The function c_c is represented in Figure 1–6 (a) and has the following formulation:

$$c_c(\kappa) = \frac{f_0}{a}\left[(1+a)\sqrt{(1+a(2+a)\kappa)} - (1+a(2+a)\kappa)\right] \geq f_{res} \qquad (1.13)$$

Where f_{res} is the residual compressive strength and f_0 and *a* are material constants.

In the evolution of κ, a confined parameter is introduced, *d*. Considering this parameter as zero will lead into under-estimation of ductility capacity and sooner strength degradation.

The rate ok κ is proportional to the plastic strain rate in the direction of the minimum principal stress $\left.\frac{\partial g}{\partial \hat{\sigma}}\right|_{\hat{\sigma} min}$. G_{fc} is the compressive fracture energy, *h* is the element size, *r* is a weight factor, and f_c is the uniaxial compressive strength.

$$\dot{\kappa} = (1-r)\cdot \frac{c_c}{\left({}^{G_{fc}}/_{h}\right)} \cdot \left.\frac{\partial g}{\partial \hat{\sigma}}\right|_{\hat{\sigma} min} \cdot e^{d\left(1+\left({}^{I_1}/_{\sqrt{3J_2}}\right)\right)^{\left({}^{-I_1}/_{3}\right)}/_{f_c}} \qquad (1.14)$$

A rotating smeared crack model is used to capture damage associated with tensile cracks. The formulation represented in Figure 1–6 (b) is given below.

$$\hat{\sigma}_i = c_t\left[(1-M)e^{-\lambda_t \frac{\hat{\varepsilon}_i - \hat{\varepsilon}_{ini}}{f_t}} + M\right] \quad i = 1,2,3 \qquad (1.15)$$

With M the ratio of residual tensile strength over tensile strength, and $\hat{\varepsilon}_{ini}$ the strain at the onset of softening (Figure 1–6 (b)).

$$c_t = \begin{cases} f_t & \kappa \leq \kappa_0 \\ \frac{c_c}{f_c} f_t & \kappa > \kappa_0 \end{cases} \text{ and } \lambda_t = \frac{(1-M)f_t^2}{{}^{G_{ft}}/_{h}} \qquad (1.16)$$

The model could capture bar buckling since a beam element was used. The element had 9 integration points along the cross-section, and one along the length. A Kim and Koutromanos constitutive law was used. This law is an enhancement of the Dodd and Restrepo material model.

Additionally, a rupture-criterion was introduced, based on the accumulation of a continuous quantity D. The rate of D is given below. The failure occurs when D becomes D_{cr}. Where D_{cr} and t are material parameters.

$$\dot{D} = \begin{cases} \left(\frac{f}{f_y}\right)^{2t} \dot{\varepsilon}_p & f > 0 \\ 0 & f \leq 0 \end{cases} \tag{1.17}$$

The continuum element and beam elements used different nodes to account for bond-slip. 1D contact elements connected the nodes, using springs in the axial direction and constraining the displacement of the nodes in the other directions. The springs had an elastoplastic constitutive material law, which was a bilinear approximation of the Murcia-Delso curve. Since the expected behavior would not be dominated by bond-failure and pullout of reinforcing bars, the use of the curve would work well.

The authors used dynamic and quasi-static experiments to validate material models. The analysis considered under quasi-static loading: RC post-tensioned walls tested under, U-shaped walls under bidirectional loading; and for the dynamic loading: a bridge pier. For the quasi-static, the following results consider damping. A comparative analysis to examine the effects of the damping in quasi-static problems was assessed. The results indicate that damping primarily affects the elastic behavior, and later the effect is negligible.

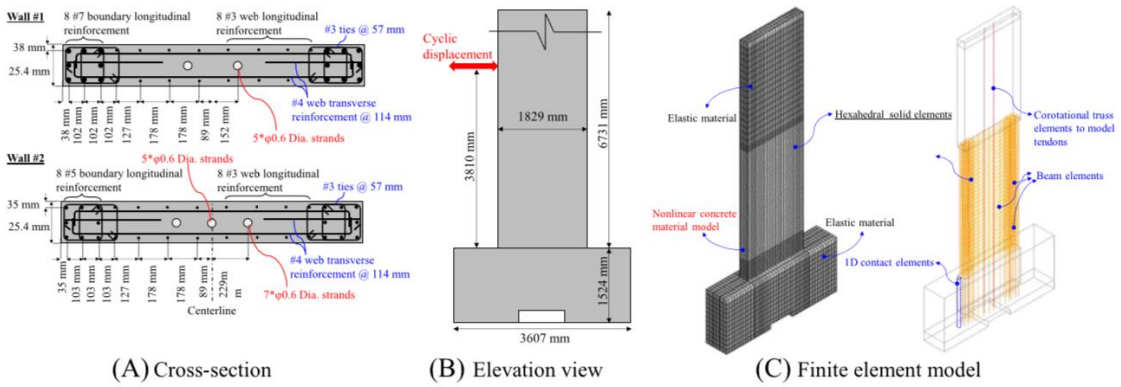

Figure 1–7: (a) Reinforcement detail, (b) elevation and geometric configuration, (c) computational model (Moharrami & Koutromanos, 2017).

The authors used test results on post-tension RC wall done by Pakiding et al. (2014). An elastoplastic constitutive law with kinematic hardening represented the tendons. Experimental data gave the yield strength and hardening slope. An autogenous strain introduced the pre-stressing. Figure 1–7 (a) and (b) show the detail of the reinforcement and geometric configuration of the test specimens. The comparison of the analytical results with the test specimen is presented in Figure 1–8. The predicted results give roughly the same strength for the positive and negative direction of loading. However, the test specimen had a higher strength for the positive cycles. The authors also indicate that the sequence of damage predicted by the model was in agreement with the one seen in the test.

The analytical model was able to capture the buckling of the reinforcement in the boundary elements. For the first specimen, the model predicted buckling at the same cycle as in the test. For the second wall, the analytical model predicted buckling during the second cycle, and in the experiment, it was seen during the last cycle.

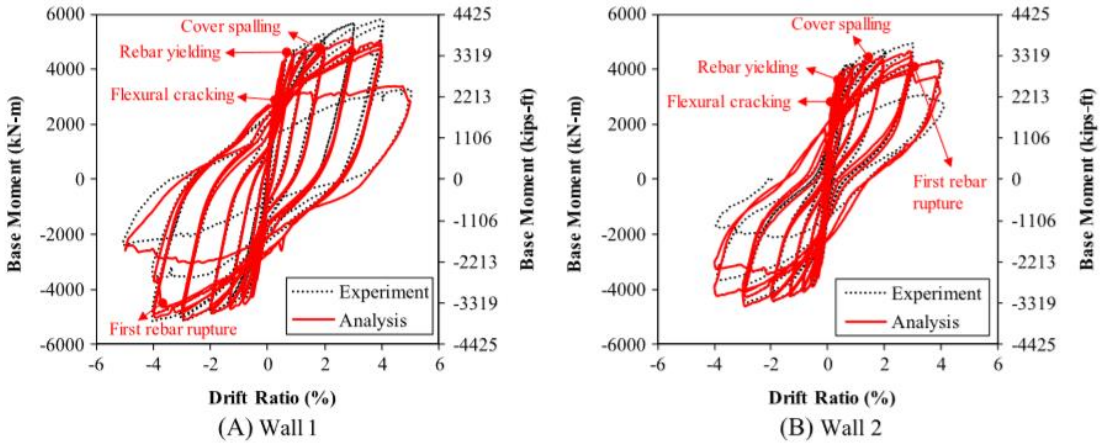

Figure 1–8: Comparison from experimental and analytical results (Moharrami & Koutromanos, 2017).

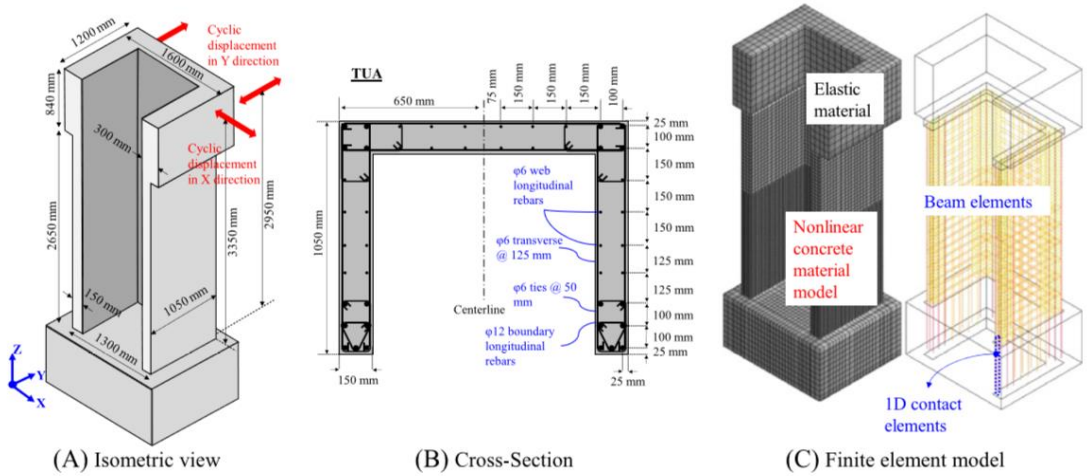

Figure 1–9: (a) elevation and geometric configuration (b) Reinforcement detail, (c) computational model (Moharrami & Koutromanos, 2017).

Beyer et al. (2008) tested the U-shaped walls used in the analysis. Figure 1–9 (a) and (b) shows the test setup and reinforcement details of the test specimen. The wall was loaded in the x and y direction. Figure 1–10 shows the comparison of the overall behavior of the test specimen and the analytical model for each direction. The initial stiffness and peak strengths are in agreement with the test specimen.

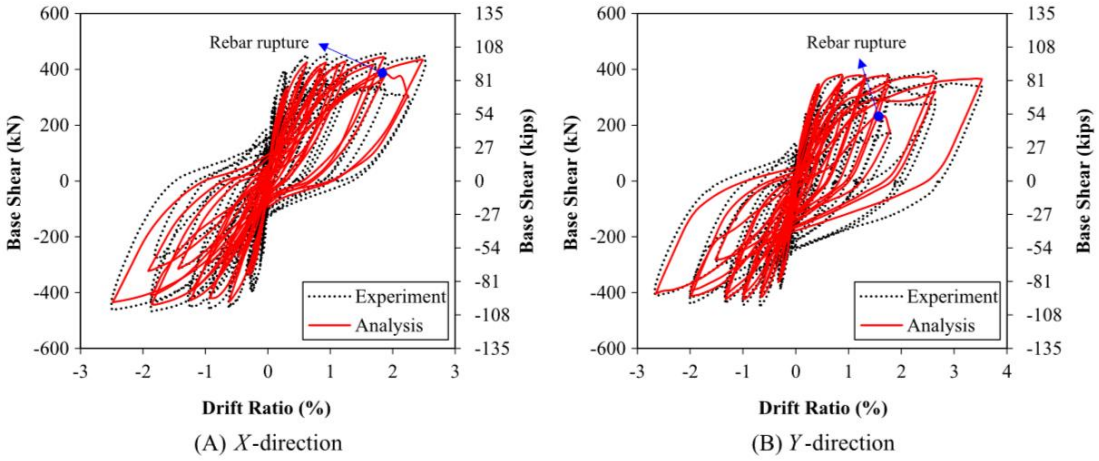

Figure 1–10: Comparison from experimental and analytical results (Moharrami & Koutromanos, 2017).

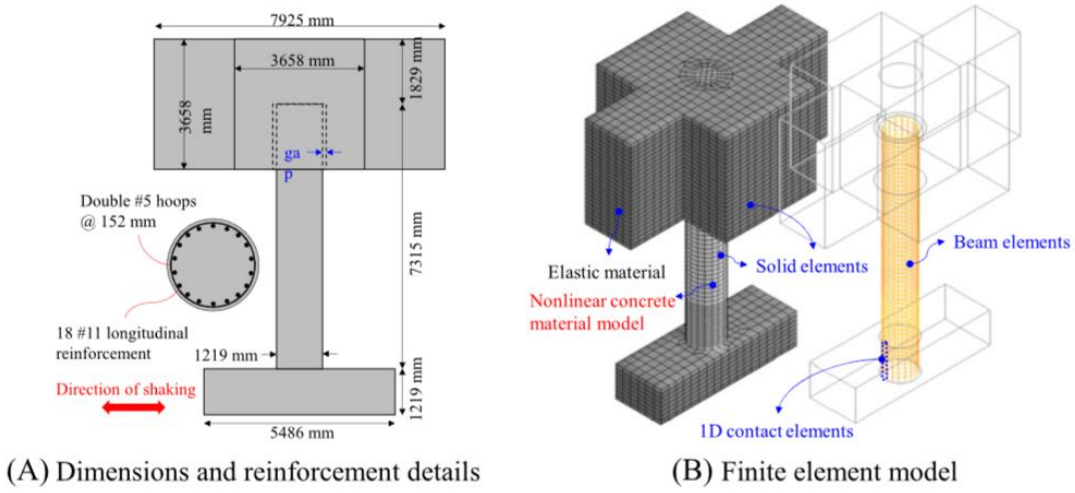

Figure 1–11: (a) elevation and geometric configuration with reinforcement detail, (b) computational model (Moharrami & Koutromanos, 2017).

Schoettler et al. (2012) tested a bridge column at the shake table of UCSD, which was subjected to a sequence of ten ground motions. Figure 1–11 (a) displays the test specimen and reinforcement detail.

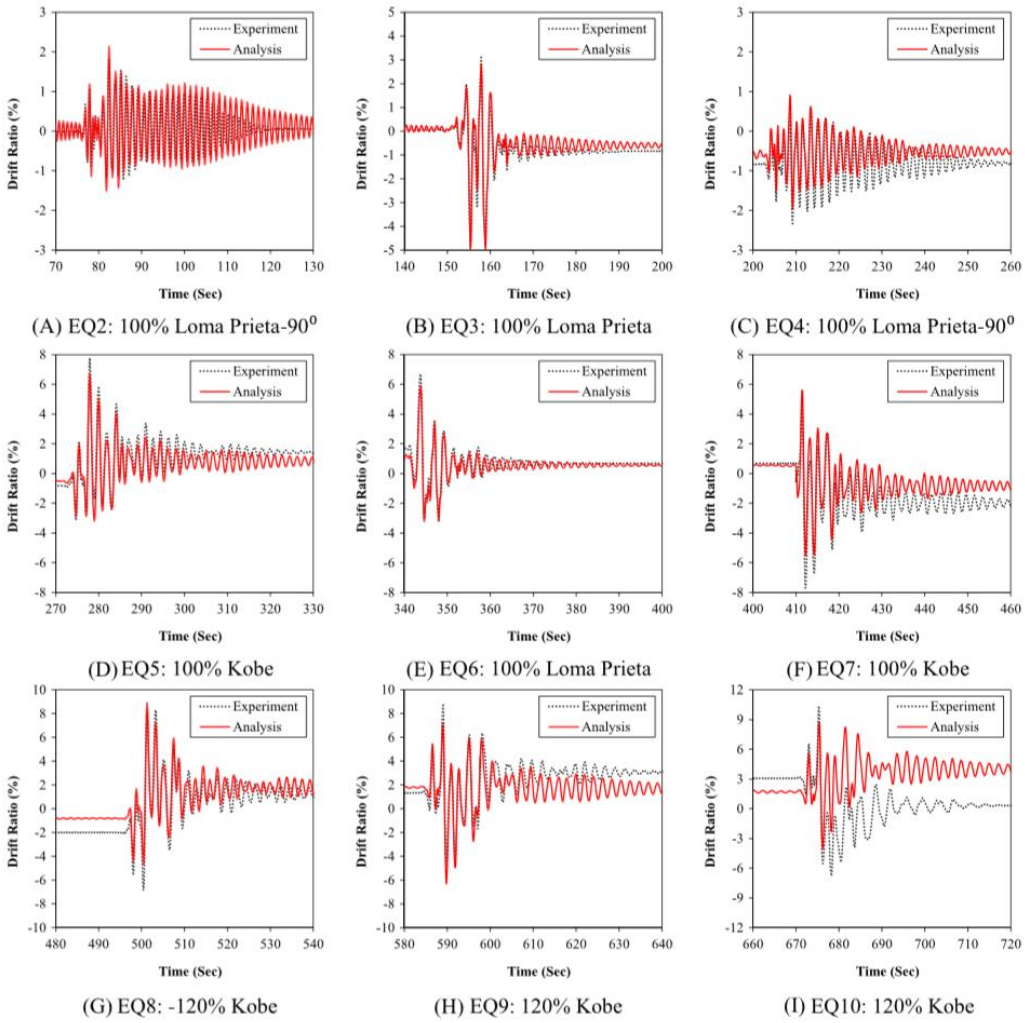

Figure 1–12: Comparison of analytical and experimental drift history for the subjected ground motions.

The model agrees with the experimental data at the first yielding. It also gives a reasonable agreement on the start of rebar buckling, and rupture. Figure 1–12 shows the drift ratio history for the subjected ground motions. The analytical response and experimental data are given. It is noticeable that the dynamic results of the models do not provide the same fit as the quasi-static models, but the prediction of important damage points matches well the experimental data.

The authors investigated the effects of strain penetration in modelling. The comparison of the overall behavior of the analytical model and the test specimen is depicted in Figure 1–13, and according to this it was stated that it has a minor impact and leads to higher stiffness and peak strength.

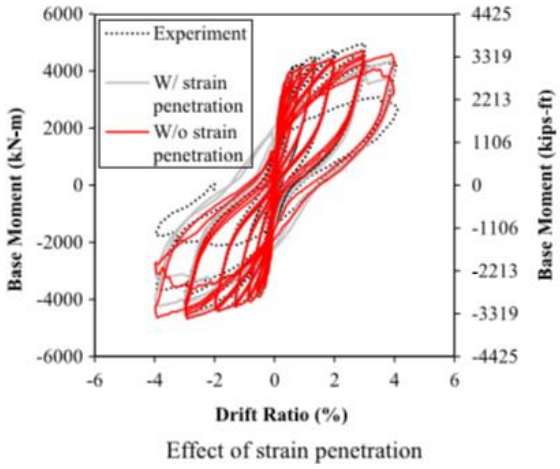

Figure 1–13: Effect of strain penetration in Wall 2 of Pakiding et al. (Moharrami & Koutromanos, 2017)

1.4 SUMMARY

The research here presented Rashid et al. (2000); Murcia-Delso (2013); and Moharrami et al. (2017), shows the implementation of detailed non-linear finite element analysis in the prediction and postdiction of the response of reinforced concrete elements to validate their use. All the authors used programs that based the concrete material in continuum 3D elements with fracture-plastic constitutive models.

The prediction of the overall behavior was well captured, in the sense of strength capacity and stiffness prediction. However, none of the investigations gave, as a result, the distribution of the deflection capacity and compare it to the tests results.

The use of beam elements to represent the reinforcement applied with the correct constitutive law could predict bar buckling. Nevertheless, once the fracture of the bar took place, it had to be manually removed from the model (Moharrami & Koutromanos, 2017).

From the results seen, it is recommended to use constitutive material laws that can capture the open and closure of flexural cracks, to be able to consider the pinching effect on the hysteresis of the elements. Otherwise, contact elements distributed along the portion where cracking are expected should be thought to account for this effect.

Another important conclusion of the analysis corresponds to the use of this type of model predictions in shaking table tests where a damping ratio consistent with the level of cracking of the element should be considered (if possible) over a constant value.

CHAPTER 2: CASE STUDY

The case study used to calibrate a detailed non-linear finite element model is a column extending into type II shaft. Which studied the column-shaft interface of a bridge column extending into a Type II shaft designed following Caltrans specifications, and reinforced with high-strength ASTM A706 Grade 80 bars. Type II shafts correspond to a pile shaft continuous with the column, where the shaft has an enlarged diameter as shown in Figure 2–1. These components are designed such that the plastic hinge will form at or above the shaft-column interface, providing an easier inspection after an earthquake.

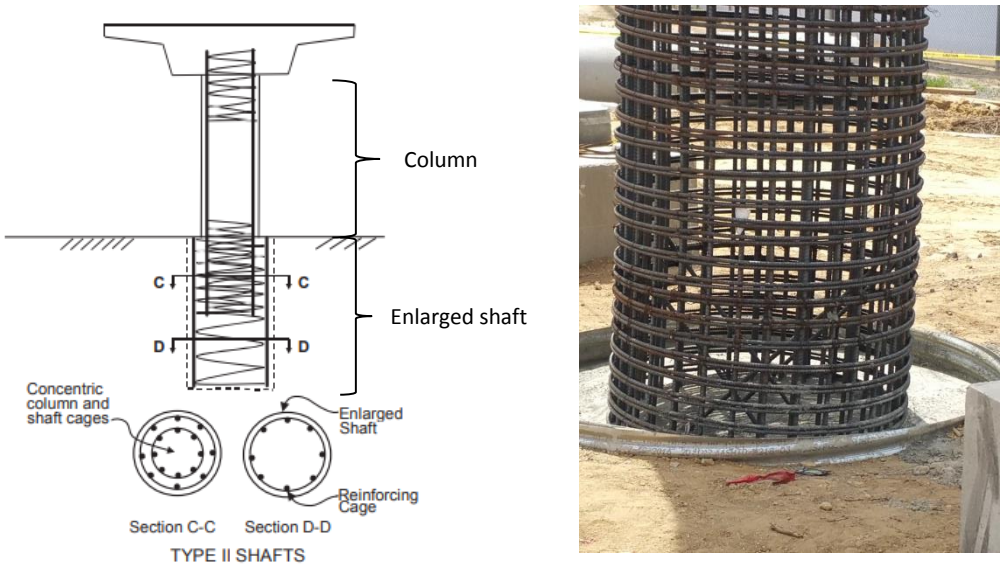

Figure 2–1: (a) Type II Pile Shafts (Caltrans, 2006) (b) interface of column-shaft (Lotfizadeh, 2019).

Due to the difference in the shaft and column diameter, there are two reinforcing cages, where column cage extends into the shaft cage and is terminated at a certain distance, creating a non-contact lap splice between both reinforcements.

Since there are no code requirements for the dimensions of the development length of a Gr.80 reinforcement, this was address during the research project (Lotfizadeh, 2019). As a result

of this research, Lotfizadeh used a scaled dimension of the tension development length of a Gr.60 reinforcement (i.e., 80 ksi/60 ksi) given by AASHTO LRFD Bridge Design Specifications (2010).

2.1 TESTS SETUP, SPECIMEN REINFORCEMENT AND GEOMETRY

The test specimen was built at full scale at the Charles Lee Powell Laboratories. It had a column diameter of 4 ft. and a shaft diameter of 6 ft., the longitudinal reinforcement of the column was 14 #14, which gives a reinforcement ratio of 0.0174, with double #5 hoops spaced at 5 in. at the first 4 ft. that provides a transverse ratio of 0.011, and then spaced at 8 in., that gives a transverse ratio of 0.0071. The shaft was reinforced with 20 #18 longitudinal reinforcement, which provides a longitudinal reinforcement ratio of 0.019. For the transverse reinforcement, #7 hoops spaced at 5 in. were used, which gives a transverse ratio of 0.00376. Figure 2–2 shows the elevation of the test specimen. Figure 2–3 and Figure 2–4 shows the section cuts of the shaft and column with the reinforcement detail.

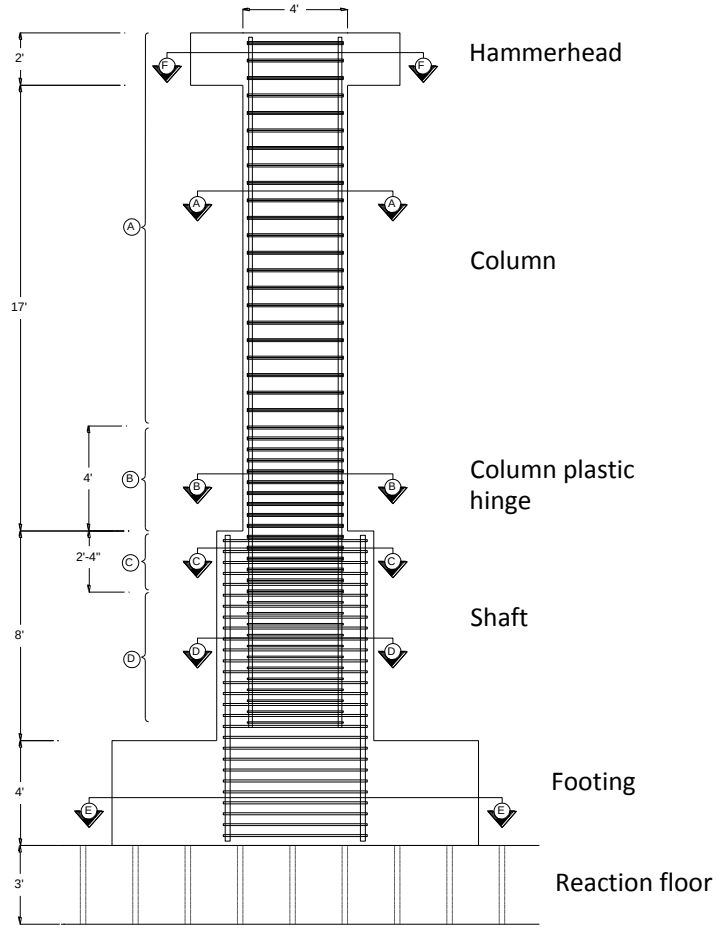

Figure 2–2: Elevation of test setup (Lotfizadeh, 2019).

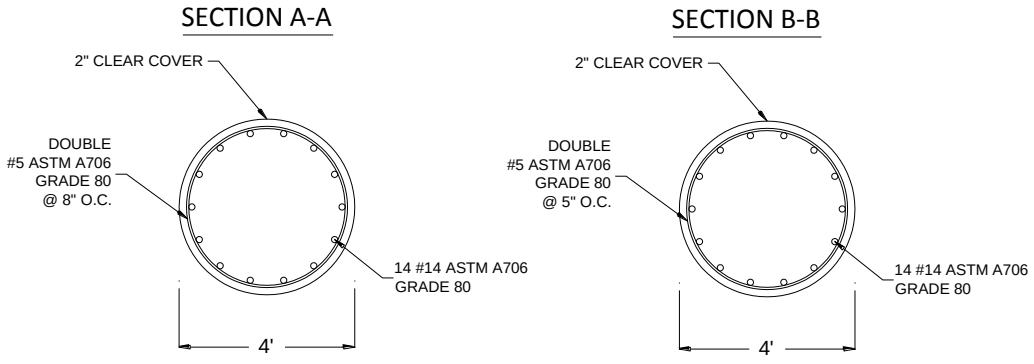

Figure 2–3: Cross section of column (Lotfizadeh, 2019).

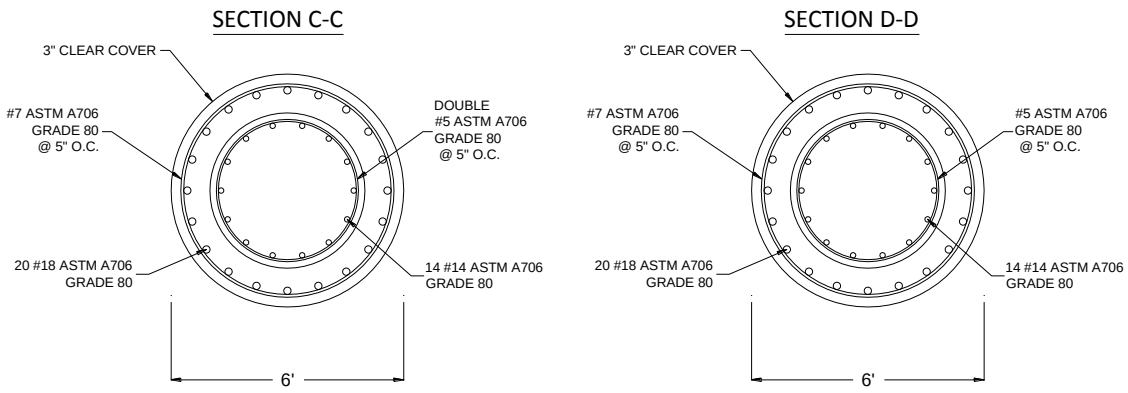

Figure 2–4: Cross section of shaft (Lotfizadeh, 2019).

The tests setup considered two additional elements are shown in Figure 2–2. The top element, refer in the following as *hammerhead*, and the lower element, placed between the reaction floor and the shaft called *footing*.

The hammerhead served to apply the lateral and additional vertical load to the column. The element was 8 ft. x 8 ft. in plan and 2 ft. height. Two actuators that ranged between the reaction wall of the laboratory and the hammerhead applied the lateral load. The stroke of this actuators was 48 in. and were placed at mid-stroke, the maximum load that each of these could apply was 220 kips. Figure 2–5 displays a render of the test setup, where it can be seen the two lateral actuators anchor to the reaction wall. To simulate an 8.6% axial load ratio on the column, an external axial load was applied using post-tensioning rods connected to the hammerhead shown in Figure 2–5 and Figure 2–6. The rods applied a total load of 800 kips, kept quasi-constant throughout the entire test. Figure 2–7 displays the reinforcement details of the hammerhead.

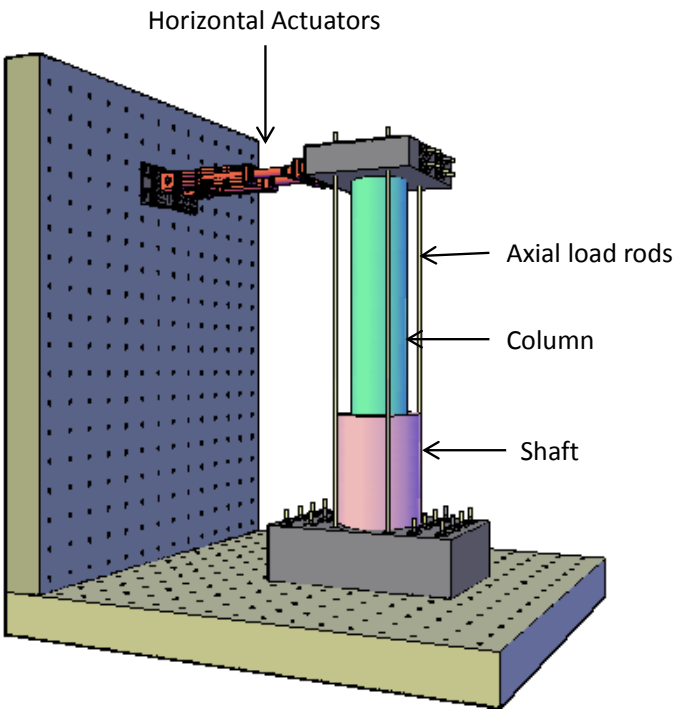

Figure 2–5: 3D view of test setup (Lotfizadeh, 2019).

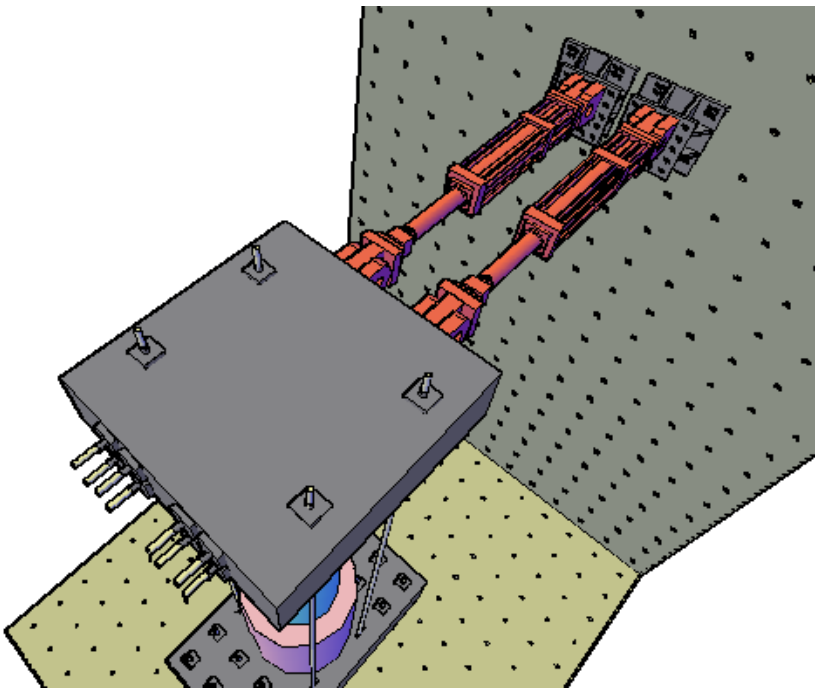

Figure 2–6: 3D View of test setup of application of external load (Lotfizadeh, 2019).

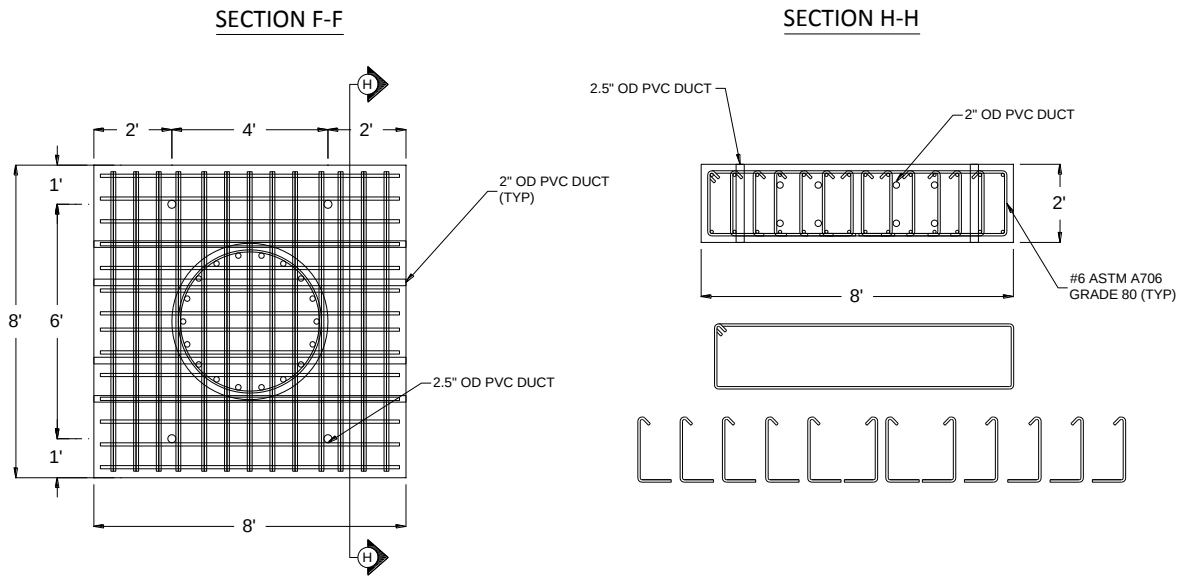

Figure 2–7: Cross section of hammerhead (Lotfizadeh, 2019).

The footing served to anchor the specimen to the strong floor. The dimensions were 14 ft. x 8 ft. in plan, and 4 ft. height. It had four cone PVC ducts as shown in Figure 2–8, to accommodate the displaced form of the post-tensioned rods that applied the vertical load to the hammerhead. The additional ducts shown in these figures worked to anchor the test to the reaction floor. Figure 2–9 shows the reinforcement detail of this section, which was design to remain elastic throughout the test.

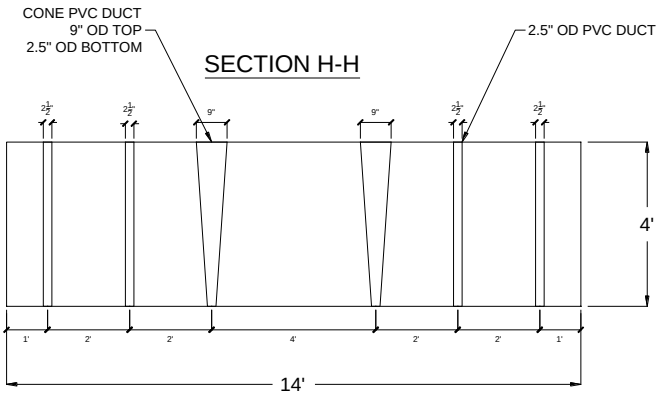

Figure 2–8: Footing elevation showing PVC ducts (Lotfizadeh, 2019).

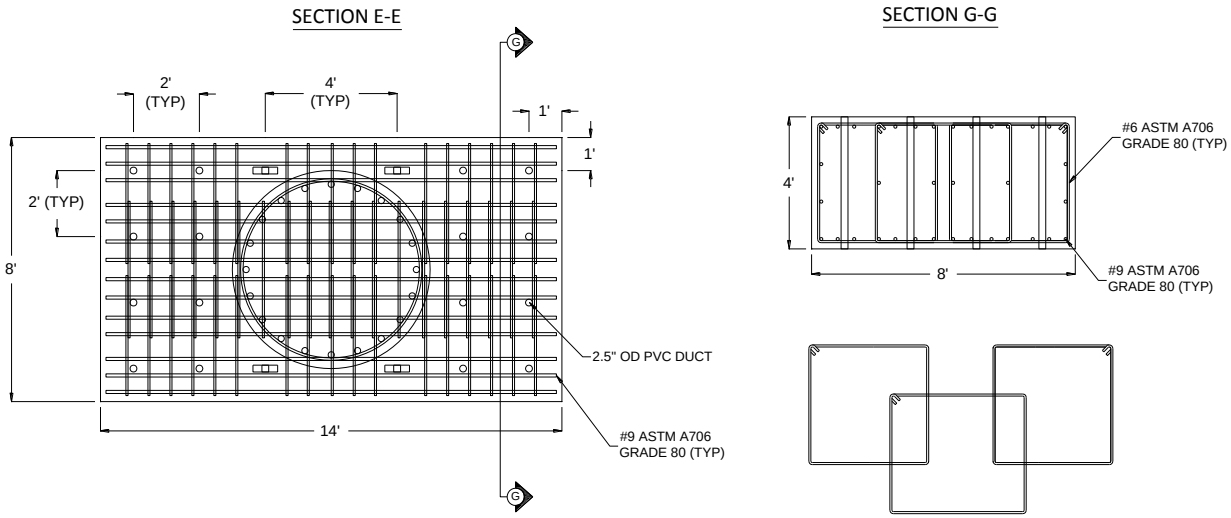

Figure 2–9: Cross section of footing (Lotfizadeh, 2019).

2.2 MATERIALS AND CONSTRUCTION PROCESS

The construction process considered four stages, shown in Figure 2–11. The first stage considered the placement of the reinforcement of the footing and PVC ducts, and the cage reinforcement of the shaft. Placing the concrete of the footing was also part of this stage. Figure 2–12 shows a picture of part of this process.

The second stage consisted of the placement of the concrete in the shaft. Since the longitudinal reinforcement of the column started at 6in higher than the footing-shaft interface, the cage of the column was placed sitting over four threated bars. The threated bars had a nut at the interface with the footing, to adjust the height to make sure of the plumbness of the column cage. The threated bars were welded at the top with the bottom of the longitudinal reinforcement of the column, see Figure 2–10. Due to the large diameter of the shaft, a steel casing was used as formwork, see Figure 2–13.

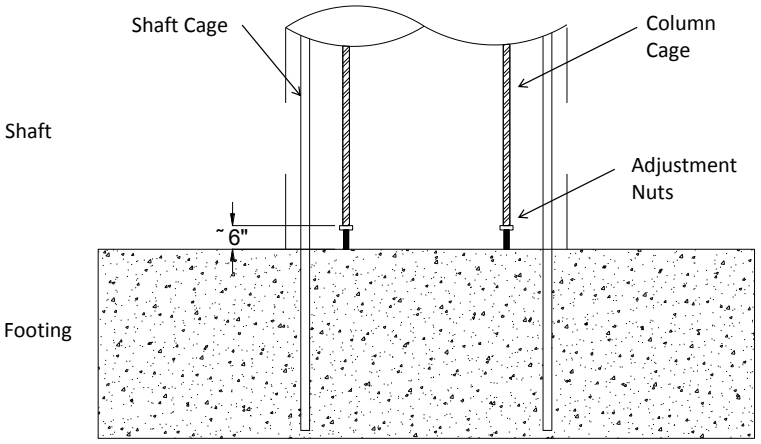

Figure 2–10: Sketch of adjustment threated bars used to place the column cage.

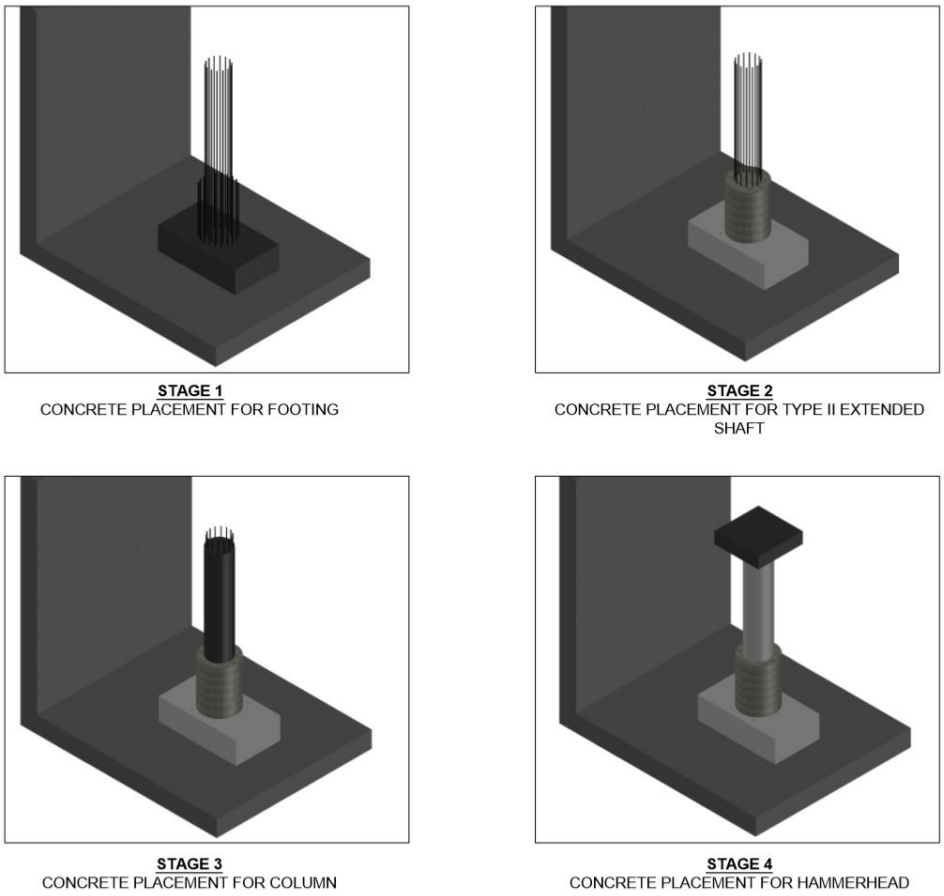

Figure 2–11: Construction stages (Lotfizadeh, 2019).

The third stage cast the column itself. Since the formwork used was Sonotube ®, see Figure 2–14. The column was cast in two stages. The first part was 48 in. height and upon setting, the remainder of the column was cast in the second part.

The hammerhead had additional vertical and longitudinal PVC ducts that were placed to anchor the lateral actuators, and the post-tensioned rods that applied the vertical load, and was cast in the fourth stage.

Figure 2–12: First stage of the construction process (Lotfizadeh, 2019).

Figure 2–13: Second stage of the construction process (Lotfizadeh, 2019).

Figure 2–14: The Sonotube® used as formwork for the column (Lotfizadeh, 2019).

The concrete specified strength was 5000 psi, with a maximum aggregate size of 1 in. The reinforcement was Gr.80 ASTM A706.

Concrete cylinder compression tests were made for the concretes of the first three construction stages. Since the hammerhead was not in the scope of this research, there is no concrete cylinder compression test data. Table 2-1 shows the concrete parameters at the day of testing (DOT).

Table 2-1: Concrete parameters (Lotfizadeh, 2019).

Region	Max. Aggregate Size [in.]	w/cm Ratio [%]	Age of Concrete at DOT [days]	f_c' [ksi]	Slump [in.]
Column Plastic Hinge	0.75	45	57	5.17	6.0
Column Elsewhere	0.75	45	57	5.08	5.5
Shaft	0.75	45	75	4.93	5.5

As part of the project two additional uniaxial compression tests were performed to obtain the compressive fracture energy, the specimens were from a different concrete pour but with the same mix. As it is known (Van Mier et al., 1997), the test setup can affect the softening part of the stress-strain curve of the concrete. The friction in the platens and the slenderness of the specimen affects it. The executed tests were performed using steel platens, where one end was free of rotating, and the other was fixed. The specimen had a hydrostone capping at both ends. The test specimen was a cylinder of 6 in. diameter and 12 in. tall, so the slenderness was 1.5 (H/D).

The compressive fracture energy (G_{fc}) is defined as the absorbed energy per unit of area in the fracture zone. Table 2-2 lists the compressive fracture energy taken from the strength to the 20% of f'$_c$ (i.e., the shaded area in Figure 2–15).

Table 2-2: Compressive Fracture Energy of Specimens (Lotfizadeh, 2019).

Specimen	G_{fc} [lb. /in.] (at σ/σ_0=0.20)
SPEC01	119
SPEC02	156

Nakamura & Higai (2001), related the compressive fracture energy (post-peak energy) to the tensile fracture energy, which is used later on this research.

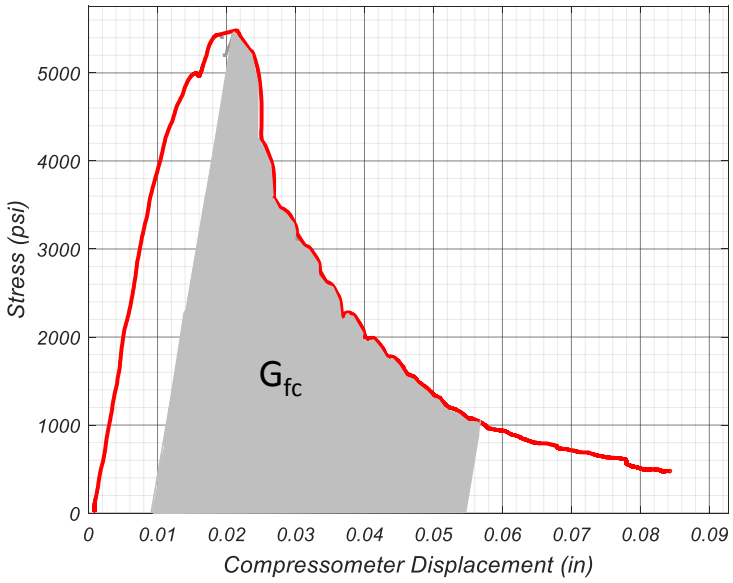

Figure 2–15: Typical axial displacement-stress response at a test cylinder (Lotfizadeh, 2019).

All the reinforcing steel in the test specimen conformed with ASTM A706 Grade 80 (A706/A706M-16). Tensile tests were carried out to obtain basic mechanical properties. For #5 circular hoops the tensile tests were performed by straightening the hoops per Caltrans Test 670 (CTM, 2013). No experimental data was available for the #7 circular hoops. Table 2-3 lists the properties for straight bars and straightened circular hoops, where f_y is the yield strength, f_{su} is the ultimate tensile strength, ε_{sh} the onset of strain hardening and ε_{su} the uniform strain (i.e. strain ,at f_{su}).

Table 2-3: Steel Parameters (Lotfizadeh, 2019)

Bar ID	f_y [ksi]	ε_{sh} [%]	f_{su} [ksi]	ε_{su} [%]	f_{su}/f_y
#18	81.9	0.610	110	11.9	1.35
#14	87.0	0.783	114	11.3	1.31
#5	87.8	- [(1)]	115	11.1	1.31
[(1)] No visible yield plateau.					

2.3 INSTRUMENTATION

The test specimen was instrumented with a dense array of 5 mm electrical foil strain in the longitudinal reinforcement of the column (88), transverse reinforcement of the column (22), longitudinal reinforcement of the shaft (48), and transverse reinforcement of the shaft (14), for a total of 172 strain gauges. Figure 2–16 and Figure 2–17 presents the location of these strains.

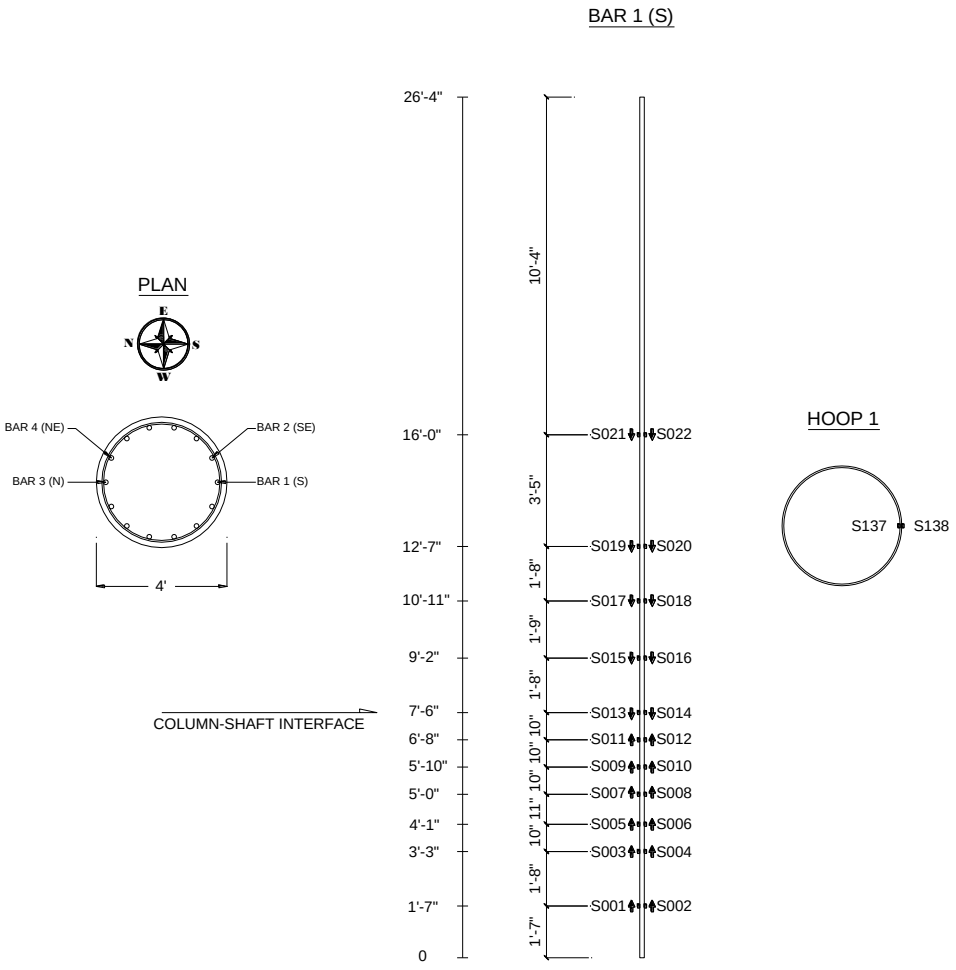

Figure 2–16: Column electrical foil strain location (Lotfizadeh, 2019).

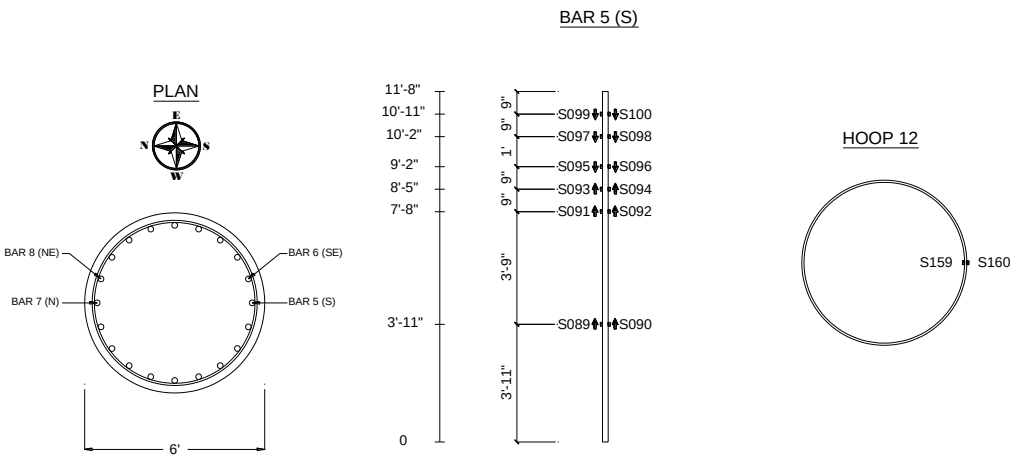

Figure 2–17: Shaft electrical foil strain location (Lotfizadeh, 2019).

The test specimen had 48 vertical linear potentiometers placed in the shaft (20) and column (28), and 10 diagonal (6) and horizontal (4) linear potentiometers. The rods of the linear potentiometers placed in the column were able to cross the entire transverse formwork since they were placed before pouring the concrete. However, since the shaft had a steel casing as formwork, it was not possible to set the shaft rods before pouring the concrete, which was done later by drilling into the hard concrete. Figure 2–18 shows a transverse cut of the column and shaft with the location of the rods. Figure 2–19 displays the vertical position.

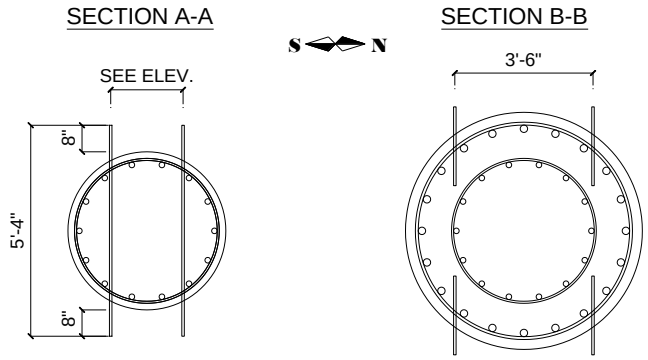

Figure 2–18: Rods of vertical linear potentiometers (Lotfizadeh, 2019).

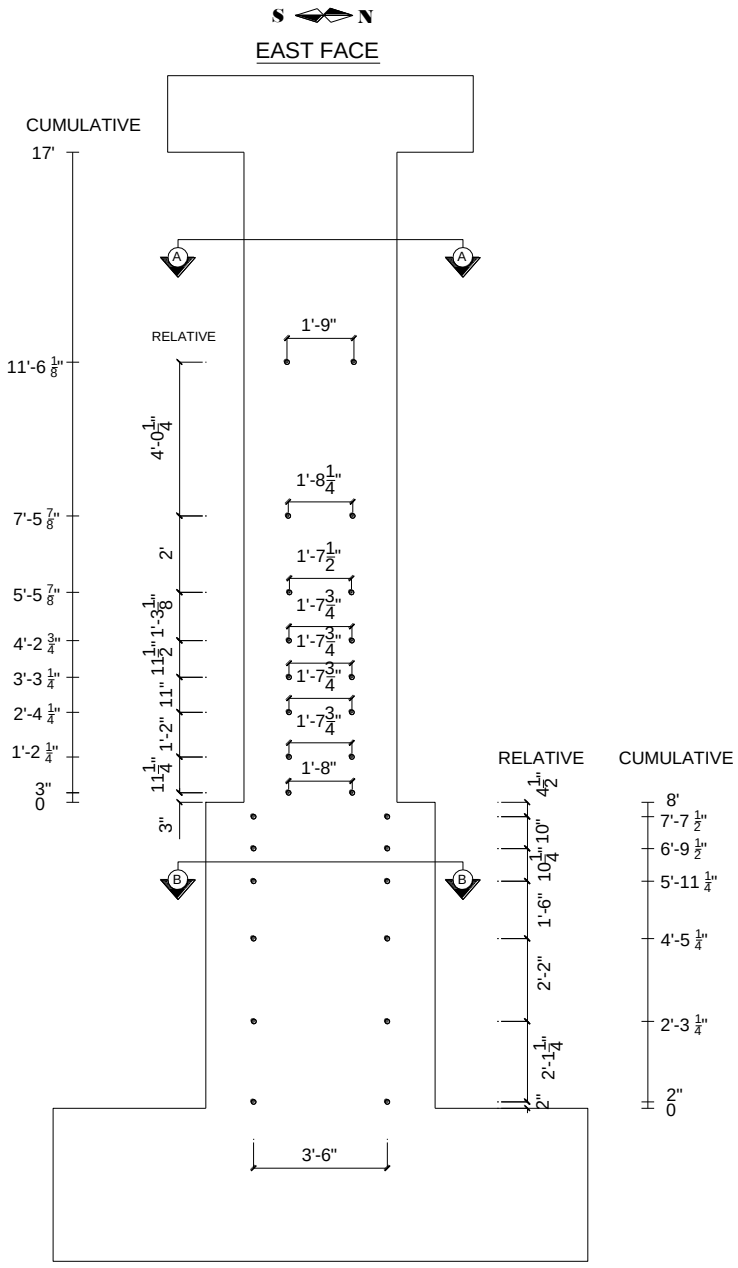

Figure 2–19: Vertical location for potentiometers (Lotfizadeh, 2019).

Additionally, it had three string potentiometers at the height of the shaft-column interface (1) and the mid-height of the hammerhead (2), shown in Figure 2–20.

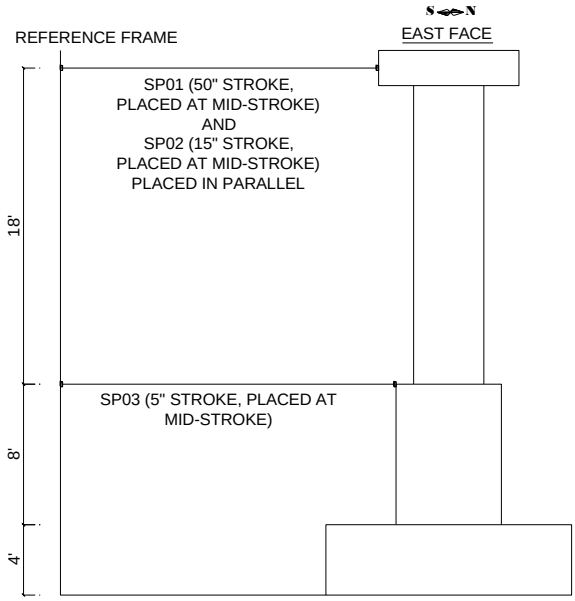

Figure 2–20: String potentiometers location (Lotfizadeh, 2019).

2.4 LOADING PROTOCOL

Loading was applied to the specimen via 2-500 kips capacity ±48 in. stroke servo-controlled actuators. The actuators were deployed horizontally between a reaction wall and the mid-depth of the specimen's hammerhead. Testing was carried out quasi-statically at the Charles Lee Powell Structural Research Laboratories of the University of California at San Diego. Testing was carried out using a prescribed load then lateral displacement controlled the loading protocol, see Figure 2–21.

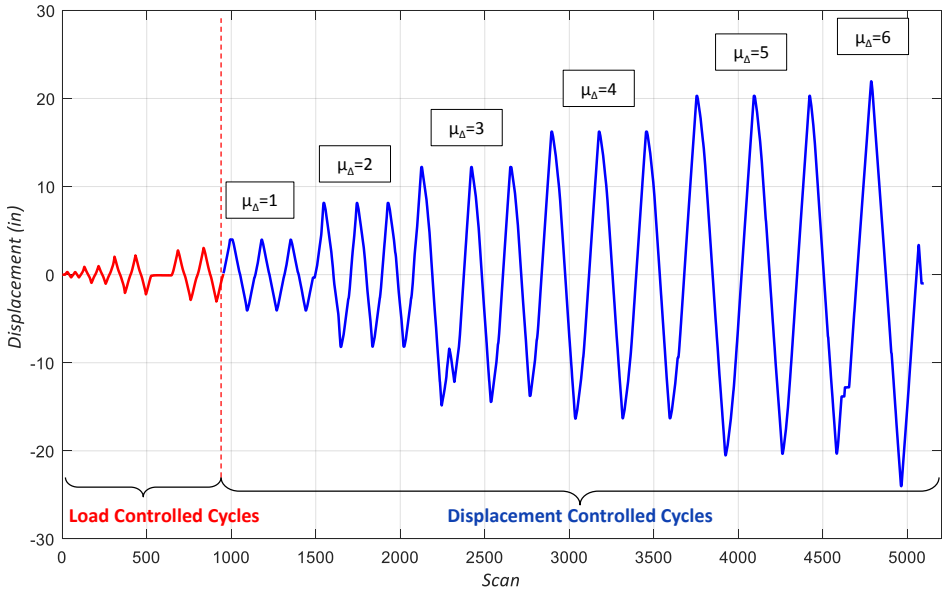

Figure 2–21: Displacement protocol recorded for the test. (Lotfizadeh, 2019).

2.5 TEST RESULTS

In the following, a summary of the most important observations and key results used in this work to validate the analytical FE model are described here. Lotfizadeh (2019) gives a detailed description.

2.5.1 Global behavior

Figure 2–22 shows the lateral load versus lateral displacement hysteretic response. The test specimen displayed a typical ductile flexural response. The flexural strength was attained at the column base and maintained at large drift ratios. The hysteretic response was characterized by round and stable loops (i.e., very little change in response upon repetition of the loop).

Considerable strength degradation was seen once the μ_Δ=5 cycles at 9.94% column drift ratio (i.e., the lateral displacement divided by the column height of 17 ft., 204 in.) begun. By the

end of the second cycle at this displacement, the lateral strength had decreased by 4% of the peak value recorded in the first cycle. By the end of the third cycle, the lateral strength had decreased by 7% of the peak value recorded on the first cycle. Only one cycle at $\mu_\Delta = 6$ at 10.7% column drift ratio was performed, since the damage included many fractured column longitudinal bars and the degradation in the lateral strength was substantial.

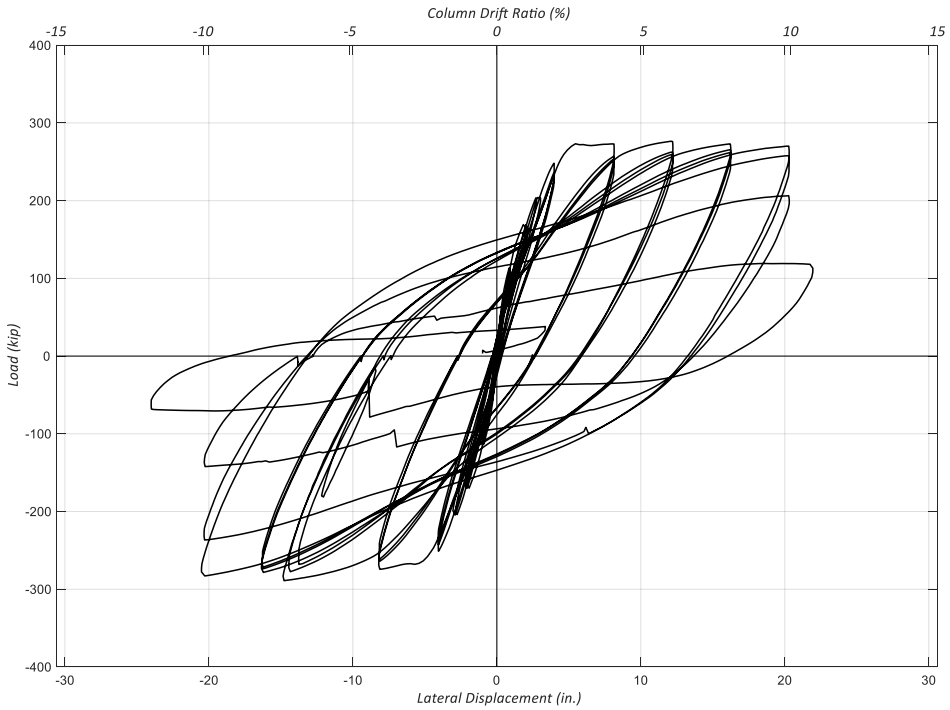

Figure 2–22: Actuator lateral load versus lateral displacement at hammerhead. (Lotfizadeh, 2019)

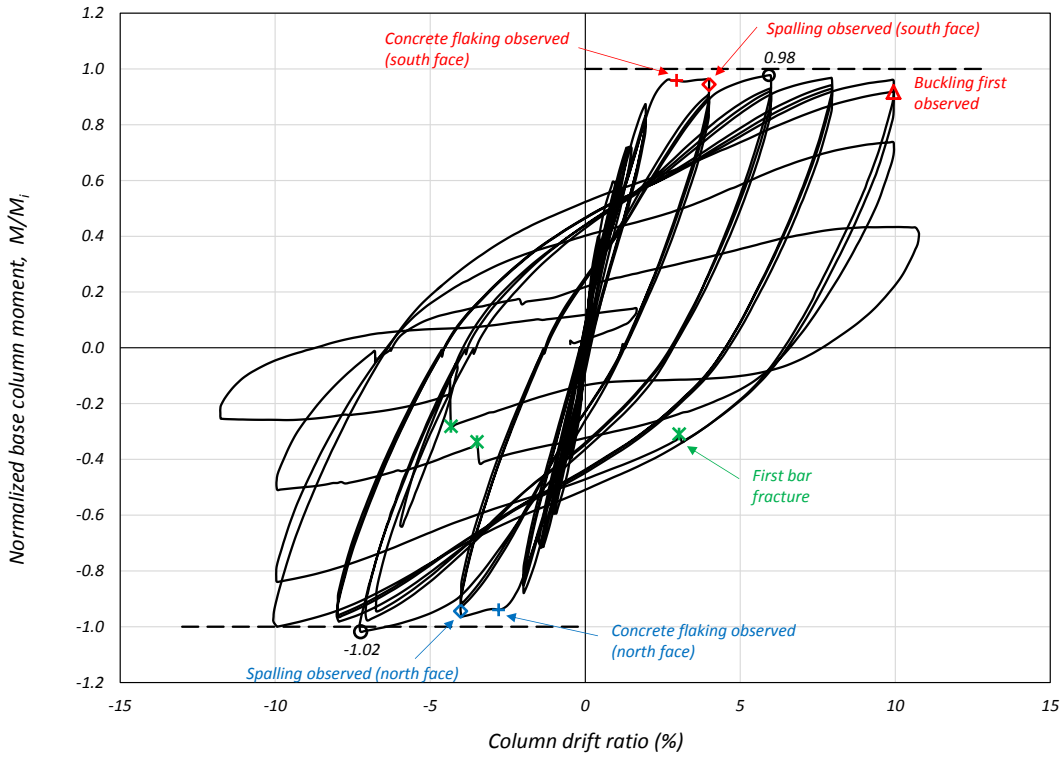

Figure 2–23: Normalized column moment versus column drift ratio. (Lotfizadeh, 2019)

Figure 2–23 displays the normalized base column moment versus the column drift ratio hysteretic response. The base column moment was computed from the deformed geometry of the specimen and using the actuator forces and the force and eccentricity of the post-tensioning roads placed to simulate axial force in the specimen, and at 204 in. from the column base. This moment was normalized by the ideal moment M_i computed with simplified flexure theory and using measured material properties corresponding to the materials at the column base.

Before the first positive peak of μ_Δ=2, at a column drift ratio of 2.95%, the first sign of concrete flaking was observed in the south face. After the peak of the same cycle, at the unloading with a column drift ratio of 3.99%, spalling in the same face of the column was observed. The first signed of bar buckling was observed at the peak of the second cycle at μ_Δ=5 at a column drift ratio of 9.94%.

Figure 2–24 shows the lateral displacement contributions at the positive and negative peak displacements computed from the linear potentiometers placed along the shaft and column, as a percentage of the total displacement measured externally at the hammerhead shown in the X-axis of the figure. The linear potentiometers in the lower column, in yellow, corresponded to the first 48 in. (22% of the column height); and the linear potentiometers in the upper column, in purple, the following 99 in. (representing 48.5% of the column height).

This figure reveals that the largest contribution of the lateral displacement was due to flexure in the lower portion of the column where plastic hinge eventually developed.

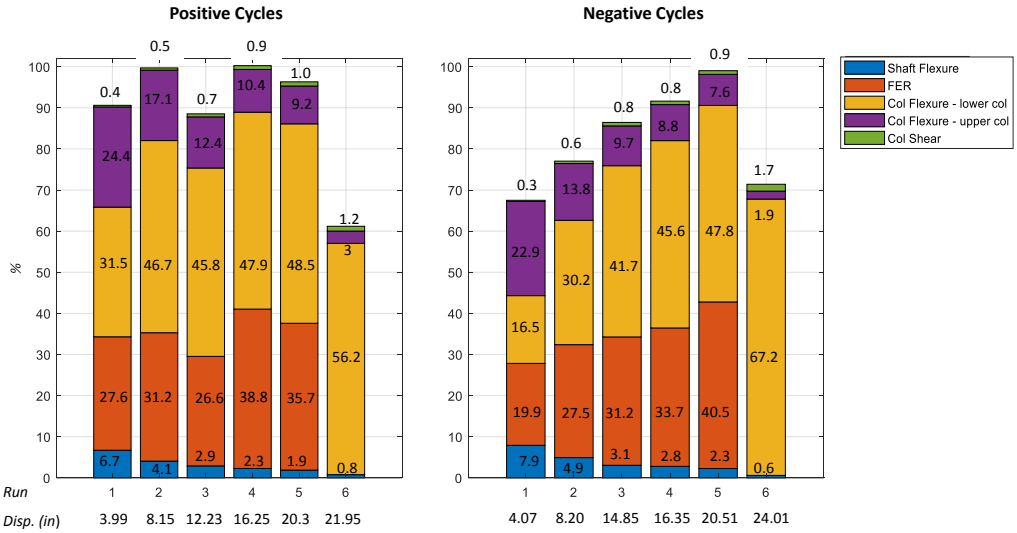

Figure 2–24: Lateral deflection contributions (Lotfizadeh, 2019).

Figure 2–25 shows the normalized moment M_{PH} measured at 194.875 in. from the column base, where plastic hinging was very pronounced, versus the normalized curvature, and the normalized moment at the column base versus the fixed end rotation caused chiefly by strain penetration. These two figures display the hysteretic response observed locally in these two parts of the column, where most of the inelastic action and energy dissipated took place in the test

specimen. The cycles are only displayed until $\mu_\Delta = 5$. For the plastic hinge region, the curvature was calculated considering the first 3 pairs of vertical potentiometers above the column base and excluding the potentiometers that monitored the fixed end rotation.

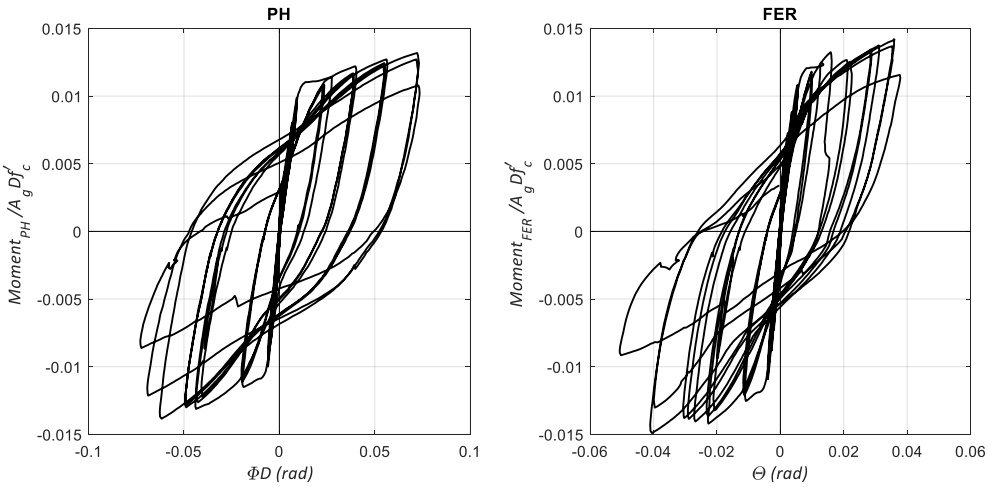

Figure 2–25: (a) Normalized moment-curvature at plastic hinge region PH, and (b) normalized moment-rotation at the shaft-column interface region FER (Lotfizadeh, 2019).

The electrical foil strain gauges of bar 1 and bar 3 shown in Figure 2–16 were used to obtain the strain distribution at the peak displacements of the first cycle of ductility 1, 2, 3 and 4. Figure 2–26 and Figure 2–27 shows the strain distributions. The electrical foil strain gauges of bar 3 at μ_Δ=3 gave wrong lectures of strains.

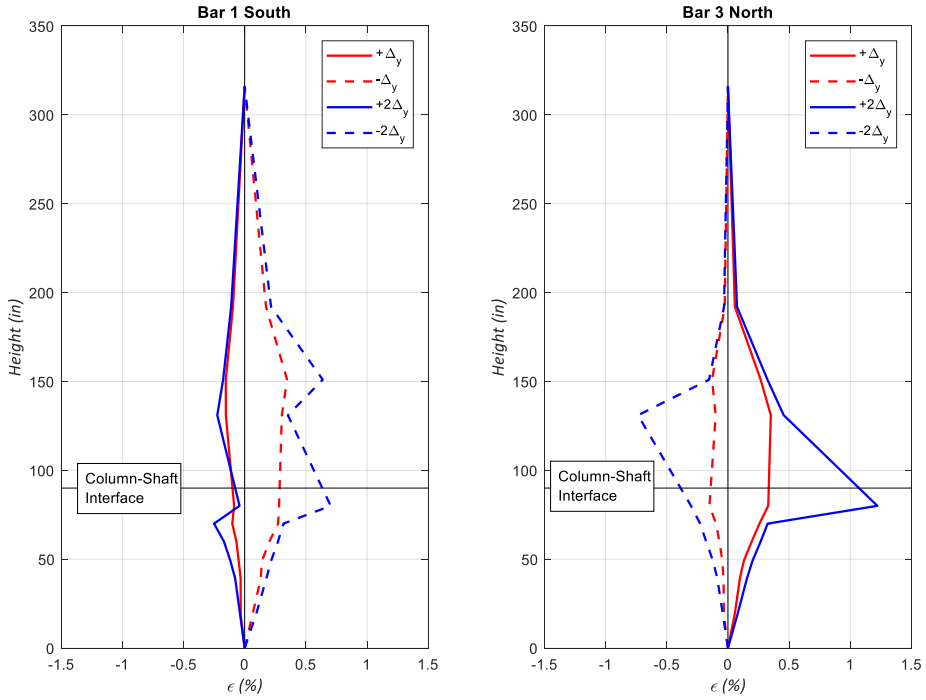

Figure 2–26: Strain distribution at south and north bar at Δ_y and $2\Delta_y$.

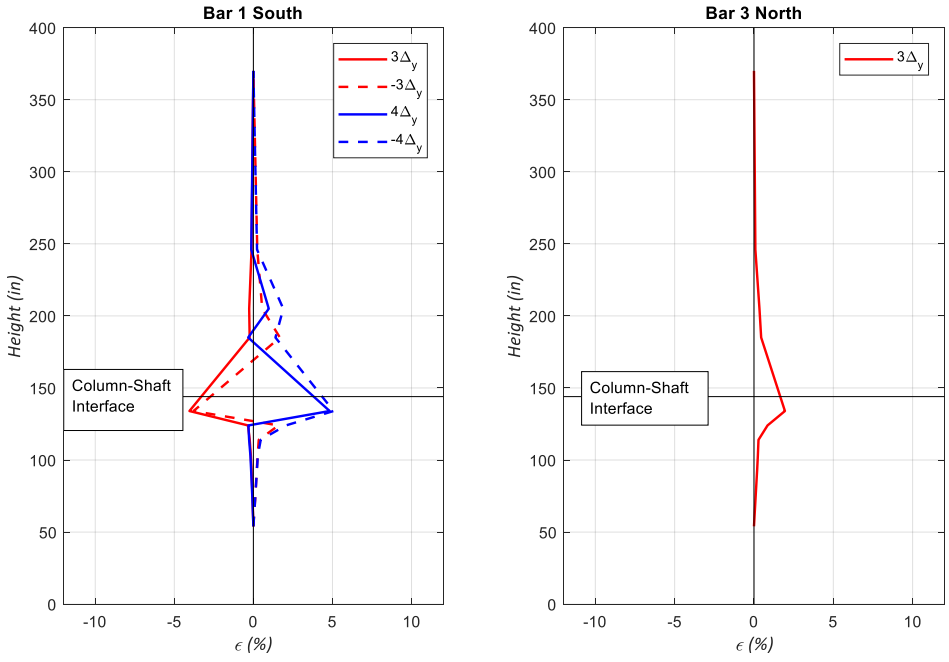

Figure 2–27: Strain distribution at south and north bar at $3\Delta_y$ and $4\Delta_y$.

2.5.2 Test observations

The damage in the test specimen was recorded. Most of the damage was encountered in the plastic hinge region, i.e., within the first 48 in. of the column. Figure 2–28 shows the interface between the column and the shaft at the end of the load control cycles. In the figure, the cracks of the east face of the column are marked with red (for the negative cycles) and black (for negative cycles). There were radial cracks in the shaft at the end of the load control cycles.

At the end of the displacement control cycles, fracture of rebar and considerable concrete crushing was observed. A 3D cloud image processing is shown in Figure 2–29 for the north face and Figure 2–30 for the south face (Lotfizadeh, 2019).

Figure 2–28: Picture of test-specimen at the shaft column interface at the end of the 75% load control cycle (Lotfizadeh, 2019).

Figure 2–29: Damage after the completion of the test at the north face (Lotfizadeh, 2019).

Figure 2–30: Damage after the completion of the test at the south face (Lotfizadeh, 2019).

CHAPTER 3: MATERIAL MODELS

ATENA Studio from Cervenka Consulting was the software chosen to perform the nonlinear analysis. This finite element program is specialized to model reinforced concrete structures. The author created a 3D finite element model with GID. GID specializes in pre-processing given a friendly user interface to generate the model. ATENA Studio performed the analysis and post-processing.

The material models used in this investigation are discussed in the following sections.

3.1 CONCRETE MODELS

The concrete model used is the facture-plastic constitutive model (named as *CC3DNonLinCementitious2*). It is a combination of a plasticity model (for compression) with a fracture model (for tension) (Cervenka et al., 2018).

The material model formulation is based on the decomposition of the strain vector into the elastic, plastic, and fracturing strains:

$$\varepsilon_{ij} = \varepsilon_{ij}^{e} + \varepsilon_{ij}^{p} + \varepsilon_{ij}^{f} \tag{3.1}$$

The stress evolution is based on the following formulation:

$$^{(n)}\sigma_{ij} = {}^{(n-1)}\sigma_{ij} + E_{ijkl}\left(\Delta\varepsilon_{kl} - \Delta\varepsilon_{kl}^{p} - \Delta\varepsilon_{kl}^{f}\right) \tag{3.2}$$

Where *E* corresponds to the elastic stiffness tensor. The fracture and plastic concrete models are reviewed below.

Fracture

For the tensile behavior of the concrete, the fracture model is based on the classical orthotropic smeared crack formulation and crack band model. The Rankine criterion is used. There are two models of the smeared cracks, the fixed-crack model and the rotated crack model.

For the fixed-crack model, the crack direction is given by the principal stress direction at the onset of crack initiation. At this point, the direction of principal stresses is fixed and represents the material orthotropic axis. In further loading steps, the difference between the principal stress and strain directions produces shear stresses in the crack plane.

For the rotated crack model, the direction of the principal stress coincides with the principal strains at every step, leading into no shear stresses at the crack plane.

The Rankine criterion:

$$F_i^f = {\sigma'_{ii}}^t - f'_{ti} \leq 0 \tag{3.3}$$

Where ${\sigma'_{ii}}^t$ is the trial tensile strength in local axes of the element, calculated with the elastic predictor, and f'_{ti} is the tensile strength in the material direction i.

$$\sigma'^t_{ij} = \sigma'^{n-1}_{ij} + E_{ijkl}{\Delta\varepsilon'}_{kl} \tag{3.4}$$

If $F_i^f > 0$

$$F_i^f = \sigma'^n_{ii} - f'_{ti} = \sigma'^t_{ii} - E_{iikl}{\Delta\varepsilon'}_{kl} - f'_{ti} = 0 \tag{3.5}$$

Assuming the increment in fracturing strain ${\Delta\varepsilon'}_{kl}$ is always perpendicular to the failure surface F^f, and that only one surface is being checked ("k"), we can state that:

$$\Delta\varepsilon'^{f}{}_{ij} = \Delta\lambda \frac{\partial F_k^f}{\partial \sigma_{ij}} \tag{3.6}$$

Introducing $\Delta\varepsilon'^{f}{}_{ij}$ into F_i^f, the fracture multiplier is computed by:

$$\Delta\lambda = \frac{\sigma_{kk}'^{t} - f_t'(w_k^{max})}{E_{kkkk}} \tag{3.7}$$

$$w_k^{max} = L_t\left(\hat{\varepsilon}_{kk}'^{f} + \Delta\lambda\right) \tag{3.8}$$

L_t is defined as the element size projected in the direction of the crack. And $\hat{\varepsilon}_{kk}'^{f}$ is the maximal fracturing strain reached during loading.

$f_t'(w_k^{max})$ is dependent on the crack opening. For pre-peak tensile stress, a linear behavior is assumed. For post-peak behavior, the exponential crack opening law derived experimentally by Hordijk et al. (1991) is used. The expressions used are stated below.

$$\frac{\sigma}{f_t'} = \left[1 + \left(c_1 \frac{w}{w_{tc}}\right)^3\right] e^{-c_2 w/w_{tc}} - \frac{w}{w_{tc}}(1 + c_1^3) e^{-c_2} \tag{3.9}$$

$$w_{tc} = 5.14 \frac{G_f}{f_t'} \tag{3.10}$$

Where w_{tc} is the crack opening at the complete release of stress. It is important to notice that w_{tc} is different to the maximum crack opening. Reported maximum crack openings were around 400-500 μm and larger.

G_f is the fracture energy that by definition is the amount of energy needed to create a unit crack area. G_f is the area under the curve shown in Figure 3–1.

σ is the crack cohesion (normal stresses 1,2,3). The parameters c_1 and c_2 correspond to 3 and 6.93 respectively and were calculated to fit experimental data from Hordijk and other authors.

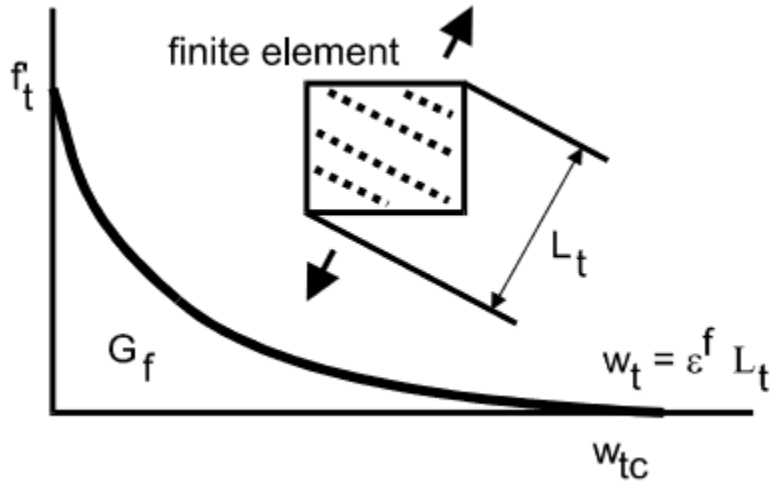

Figure 3–1: Tensile softening (Cervenka et al., 2018).

Plasticity

For the plastic surface, the failure surface given by Menétrey- Willam (1995) was used. The model is formulated in the Haigh-Westergaard coordinate system. The relation between the stress vector and the Haigh-Westergaard coordinates is shown below.

$$\begin{bmatrix}\sigma_1\\ \sigma_2\\ \sigma_3\end{bmatrix} = \frac{1}{\sqrt{3}}\begin{bmatrix}\xi\\ \xi\\ \xi\end{bmatrix} + \sqrt{\frac{2}{3}}\rho\begin{bmatrix}\cos(\theta)\\ \cos(\theta - 2\pi/3)\\ \cos(\theta + 2\pi/3)\end{bmatrix} \quad (3.11)$$

With ξ the hydrostatic stress invariant, ρ the deviatoric stress invariant, and θ the deviatoric stress angle.

The model is based on three parameters that involve properties of uniaxial tests such as the compressive strength f_c', tensile strength f_t', and an out of roundness parameter e.

$$F_p(\xi,\rho,\theta) = \left[\sqrt{1.5}\frac{\rho}{f_c'}\right]^2 + m\left[\frac{\rho}{\sqrt{6}f_c'}r(\theta,e) + \frac{\xi}{\sqrt{3}f_c'}\right] - c = 0 \quad (3.12)$$

Where m is presented as in the original model and c evolves through crushing/yielding. The function $r(\theta,e)$ gives the shape of a triple symmetric elliptic.

$$m = 3\frac{(f_c')^2-(f_t')^2}{f_c'f_t'}\frac{e}{e+1} \quad (3.13)$$

$$r(\theta,e) = \frac{4(1-e^2)\cos^2(\theta)+(2e-1)^2}{2(1-e^2)\cos(\theta)+(2e-1)[4(1-e^2)\cos^2(\theta)+5e^2-4e]^{1/2}} \quad (3.14)$$

$$c = \left(\frac{f_c'(\varepsilon_{eq}^p)}{f_c'}\right)^2 \quad (3.15)$$

$f_c'(\varepsilon_{eq}^p)$ indicates the hardening/softening law, based on the uniaxial compressive test. And ε_{eq}^p represents the equivalent plastic strain. Figure 3–2 depicts the laws used by the program. As it can be seen the plastic surface (F_p) is not unique, and it evolves with the equivalent plastic strain ε_{eq}^p.

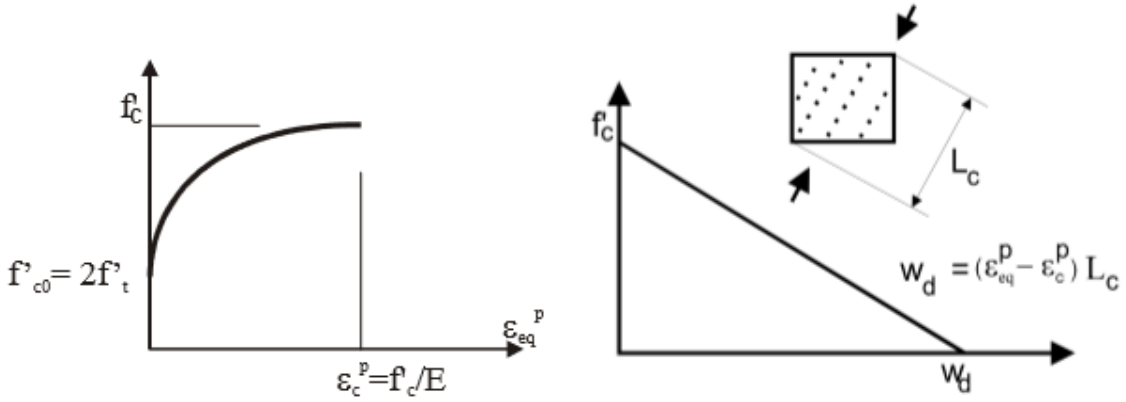

Figure 3–2: Hardening/softening laws used in CC3DNonLinCementitiuos model (Cervenka et al., 2018).

The hardening is modeled with a linear and nonlinear branch. The nonlinear curve is governed by:

$$\hat{f}_c(\varepsilon_{eqp}) = f'_{c0} + (f'_c - f'_{c0})\sqrt{1 - \left(\frac{\varepsilon_{cp} - \varepsilon_{eqp}}{\varepsilon_{cp}}\right)^2} \tag{3.16}$$

With f'_{c0} representing the stress at the onset of nonlinear hardening and ε_{cp} the strain at which fc' is reached in a uniaxial test.

From Figure 3–2, the softening branch is linear and based on displacements. In this figure, w_d is the critical compressive displacement from Van Mier's formulation. L_c is the crushing band calculated for each FE as the projection of the element size in the direction of the minimum compressive stress.

Since the softening is a function of the displacement instead of strain, mesh objectivity is introduced to the formulation (Nakamura & Higai, 2001).

w_d parameter is assumed as a material property, as it was found by Van Mier et al. (1997). Van Mier (1984) found a value of -0.5 mm (-0.0197 in.), and Nakamura & Higai found -2.5 mm (-0.0984 in.) (Cervenka et al., 2018). As we can see this parameter is not well understood, and different authors have found different values. In 2001, RILEM released recommendations for the test method to measure strain-softening behavior of concrete under uniaxial load. From values found in a Round Robin test, considering the recommendations above, the values for w_d range around -0.75 mm (-0.0295 in.) (Van Mier et al., 1997).

Regarding the out of roundness parameter, a.k.a. eccentricity, it will control the relation between the uniaxial and equibiaxial compressive strength. Figure 3–3 represents the relation

when $\sigma_3 = 0$. A value of 0.52 it is recommended by Cervenka Consulting, that is equivalent to consider $f'_{bc} = 1.14 f'_c$, which is in agreement with Kupfer et al. (1969).

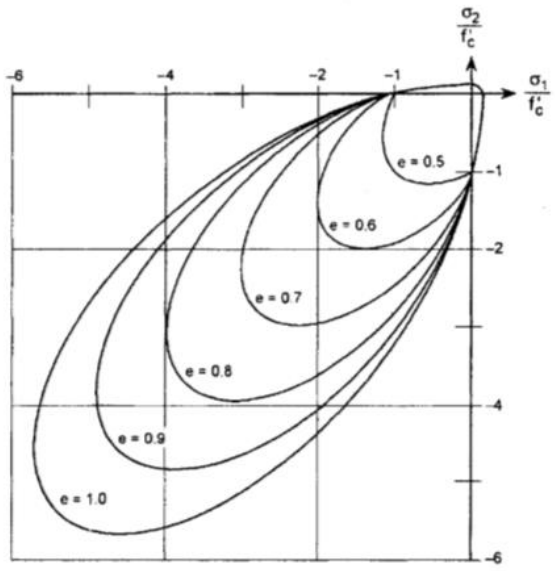

Figure 3–3: Influence of eccentricity on biaxial strength for the 3 parameter criterion (Menetrey & Willam, 1995).

The plastic potential G^pgoverns the direction of the plastic flow. G^p is a function that depends on parameter β. β defines the volumetric change during crushing (positive means expansion, negative values mean contraction, and if it is equal to zero the volume is preserved).

$$G^p(\bar{\sigma}) = \beta \frac{I_1}{\sqrt{3}} + \sqrt{2J_2} = \beta\xi + \rho \tag{3.17}$$

The iterative process to recover the new stress state is based on a predictor-corrector formula. The input parameters are:

$$^{(n-1)}\sigma_{ij} \qquad ^{(n-1)}\varepsilon_{ij}^{p} \qquad \Delta^{(n)}\varepsilon_{ij} \tag{3.18}$$

$$^{(n)}\sigma_{ij} = {}^{(n-1)}\sigma_{ij} + E_{ijkl}\left(\Delta\varepsilon_{kl} - \Delta\varepsilon_{kl}^{p}\right) = \sigma_{ij}^{t} - E_{ijkl}\Delta\varepsilon_{kl}^{p} = \sigma_{ij}^{t} - \sigma_{ij}^{p} \tag{3.19}$$

Where σ_{ij}^{t} is the elastic predictor, computed as:

$$\sigma_{ij}^{t} = {}^{(n-1)}\sigma_{ij} + E_{ijkl}\Delta^{(n)}\varepsilon_{kl} \tag{3.20}$$

Where σ_{ij}^{p} is the plastic corrector, computed as:

$$f_i^p = F^p\left(\sigma_{ij}^{t} - \sigma_{ij}^{p}\right) = F^p\left(\sigma_{ij}^{t} - \Delta\lambda^i E m_{ij}\right) = 0 \tag{3.21}$$

With $m_{ij} = \frac{\partial G^p\left(\sigma_{ij}^{t}\right)}{\partial \sigma_{ij}}$.

For the first iteration, the plastic multiplier increment will be set equal to zero ($\Delta\lambda^{i=1} = 0$).

If $f_i^p > 0$, then the failure criterion is violated, and the procedure is:

Compute the return direction ${}^{(i)}m_{ij}$

Compute $\Delta\lambda^{i+1}$ with $F^p\left(\sigma_{ij}^{t} - \Delta\lambda^{i+1}E^{(i)}m_{ij}, {}^{(n-1)}\varepsilon_{ij}^{p}\right) = 0$

Evaluate $f_{i+1}^p = F^p\left(\sigma_{ij}^{t} - \Delta\lambda^{i+1}E^{(i)}m_{ij}, {}^{(n-1)}\varepsilon_{ij}^{p} + \Delta\lambda^{i+1}\,{}^{(i)}m_{ij}\right)$

Then as long as $\left|\Delta\lambda^i - \Delta\lambda^{i+1}\right| > e$

$$\Delta\lambda^{i+2} = \Delta\lambda^i - f_i^p \frac{\Delta\lambda^{i+1} - \Delta\lambda^i}{f_{i+1}^p - f_i^p}$$

$${}^{(i+1)}m_{ij} = \frac{\partial G^p\left(\sigma_{ij}^{t} - \Delta\lambda^{i+2}E^{(i)}m_{ij}\right)}{\partial \sigma_{ij}}$$

$$f_{i+2}^p = F^p\left(\sigma_{ij}^{t} - \Delta\lambda^{i+2}E^{(i+1)}m_{ij}, {}^{(n-1)}\varepsilon_{ij}^{p} + \Delta\lambda^{i+2\,(i+1)}m_{ij}\right)$$

Then if $f_{i+2}^{p} < 0$ do $f_{i+1}^{p} = f_{i+2}^{p}$ $\Delta\lambda^{i+1} = \Delta\lambda^{i+2}$

$f_{i+2}^{p} \geq 0$ do $f_{i}^{p} = f_{i+1}^{p}$ $\Delta\lambda^{i} = \Delta\lambda^{i+1}$

$f_{i+1}^{p} = f_{i+2}^{p}$ $\Delta\lambda^{i+1} = \Delta\lambda^{i+2}$

End of the algorithm, update:

$$^{(n)}\varepsilon_{ij}^{p} = {}^{(n-1)}\varepsilon_{ij}^{p} + \Delta\lambda^{i+1\,(i+1)}m_{ij}$$

$$^{(n)}\sigma_{ij} = \sigma_{ij}^{t} - \lambda^{i+1\,(i+1)}E\, m_{ij}$$

3.2 REINFORCEMENT MODELS

There are two ways of considering reinforcement in ATENA. The first is using a uniaxial material associated with line elements, and the second is through smeared reinforcement associated with the concrete material in 3D elements (Cervenka et al., 2018).

For the case of the uniaxial elements, the program allows considering the cyclic response of the reinforcement through Menegotto-Pinto (1973) cyclic model. The backbone curve of the steel corresponds to a multilinear stress-strain curve.

The implementation of the Menegotto-Pinto (M-P) model differs from the one given in Filippou et al. (1983). The model is based on the following formulations:

$$\sigma^* = b\varepsilon^* + \frac{(1-b)\varepsilon^*}{(1+\varepsilon^{*R})^{1/R}} \tag{3.22}$$

$$\sigma = (\sigma_0 - \sigma_r)\sigma^* + \sigma_r \tag{3.23}$$

$$\varepsilon^* = \frac{\varepsilon-\varepsilon_r}{\varepsilon_0-\varepsilon_r} \tag{3.24}$$

$$R = R_0 - \frac{c_1\xi}{c_2+\xi} \tag{3.25}$$

The parameters c_1, c_2 and R_0 are experimentally determined. Typical values for this in the original implementation of the model range between 20, 18.5 and 0.15 respectively. However, in ATENA the recommended values are 4, 500, 50.

Figure 3–4 shows the comparison between M-P given by Steel02 Material in OpenSees (2013) and the M-P obtained from ATENA. For the Steel02 the setting was taken as: the yield strength and elastic modulus set from the test values obtained for bar #14, the strain hardening

ratio (b) as 0.012, R_0 as 20, cR1 as 0.9 and cr2 as 0.08, a1 as 0.039, a2 and a4 as 1 and a3 as 0.029.

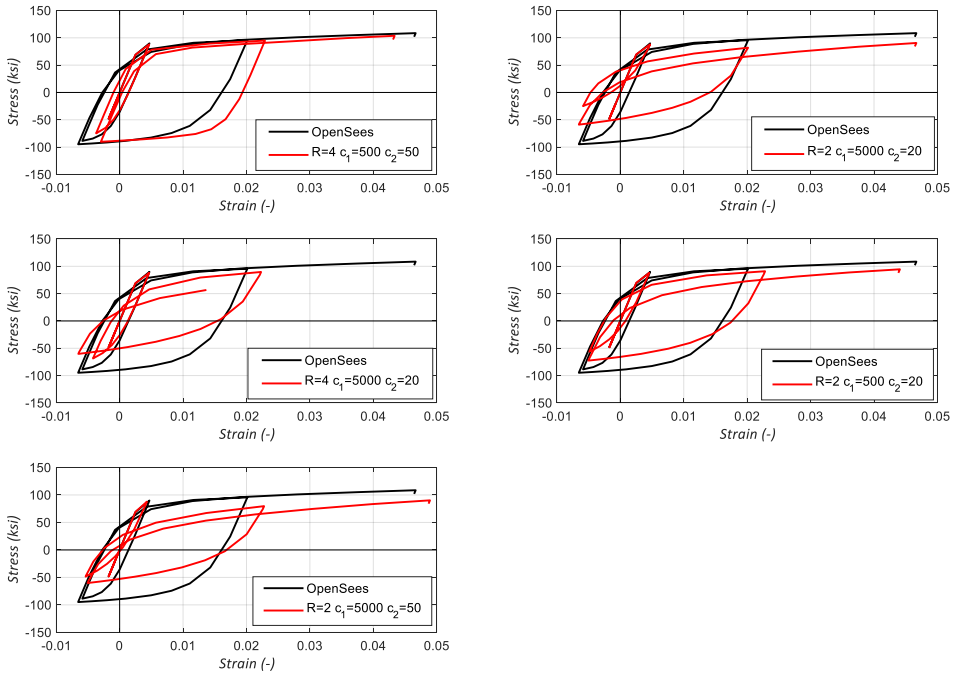

Figure 3–4: Comparison between OpenSees and ATENA implementation of Menegotto-Pinto.

From the figure, the curve with the parameters recommended by ATENA fits better with the curve given by OpenSees (2013) for the first cycle.

Deactivating the compressive response of the reinforcement is possible. If activated, buckling in the rebar is assumed, and the strength of the element is considered negligible.

The bond-slip of the rebar can be accounted with three different models provided by the software. These are the CEB-FIB model code from 1990, the bar bond slip law by Bigaj (1999), and a user-defined law.

The user-defined law is a bond slip-bond strength definition, i.e., no elastic bond slip is considered in the bond mode, and only when the bond strength is reached the bar starts to slip. It should not start from zero strength for zero slip ($0.1\tau_b$).

3.2.1 CEB-FIB 1990 Model Code

The model given by CEB-FIP (1990) gives the bond stress for a monotonic loading calculated as a function of the relative displacement s.

$$\tau = \begin{cases} \tau_{max}\left(s/s_1\right)^{\alpha} & 0 \le s \le s_1 \\ \tau_{max} & s_1 < s \le s_2 \\ \tau_{max} - \left(\tau_{max} - \tau_f\right)\left(\frac{s-s_2}{s_3-s_2}\right) & s_2 < s \le s_3 \\ \tau_f & s_3 < s \end{cases} \tag{3.22}$$

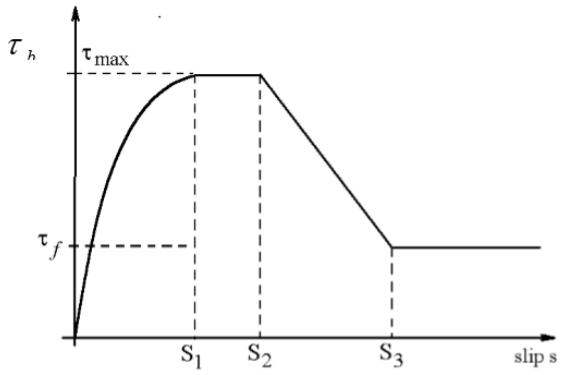

Figure 3–5: Bond-slip model by CEB-FIB 1990 (Cervenka et al., 2018)

The parameters used for the model considers a ribbed bar. Table 3-1 shows the parameters used. These values are applicable only in loading states where the concrete is not subjected to lateral tension.

Table 3-1: Parameters for defining the mean bond stress-slip relationship. (CEB-FIP, 1990)

	Column 2	Column 3	Column 4	Column 5
	Unconfined concrete*		Confined concrete†	
	Good bond conditions	All other bond conditions	Good bond conditions	All other bond conditions
s_1	0.6 mm	0.6 mm	1.0 mm	1.0 mm
s_2	0.6 mm	0.6 mm	3.0 mm	3.0 mm
s_3	1.0 mm	2.5 mm	Clear rib spacing	Clear rib spacing
α	0.4	0.4	0.4	0.4
τ_{max}	$2.0\sqrt{f_{ck}}$	$1.0\sqrt{f_{ck}}$	$2.5\sqrt{f_{ck}}$	$1.25\sqrt{f_{ck}}$
τ_f	$0.15\tau_{max}$	$0.15\tau_{max}$	$0.40\tau_{max}$	$0.40\tau_{max}$

*Failure by splitting of the concrete.
†Failure by shearing of the concrete between the ribs.

To use columns 2 and 3 (unconfined concrete), minimum requirements are set:

- Concrete cover $c = 1\phi_s$
- Minimum transverse reinforcement $A_{st,min} = 0.25nA_s$

To use columns 4 and 5 (well-confined concrete), the requirements are:

- Concrete cover $c \geq 5\phi_s$
- Clear spacing $> 10\phi_s$
- Closely spaced transverse reinforcement $A_{st} > nA_s$
- Or high transverse pressure $p \geq 7.5MPa$

Where *n* is the number of bars enclosed by the stirrups, A_{st} area of stirrups (two legs) over a length equal to the anchorage length, and A_s the area of one bar.

3.2.2 Bond Model by Bigaj

The model is based on the experimental investigation made by Bigaj (1999) on her doctoral dissertation. For the first stage, between points 1 and 2 shown in the figure below, a bi-linear curve is used. Table 3-2 lists the coordinates of the points 1 through 4, where D represents the reinforcement bar radius.

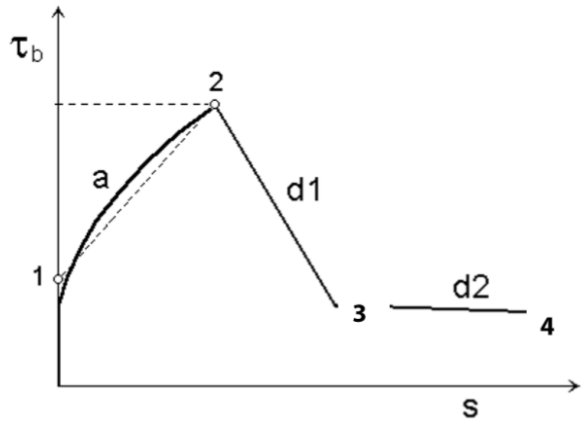

Figure 3–6: Bond-slip model by Bigaj 1999 (Cervenka et al., 2018)

Table 3-2: Parameters for defining bond strength-slip relation (Cervenka et al., 2018).

Concrete Type	Bond quality		Point 1	Point 2	Point 3	Point 4
$f_c^{'} < 60$	Excelent	s / D	0.000	0.020	0.044	0.480
		$\tau_b / \sqrt{0.8\, f_{cu}^{'}}$	0.500	3.000	0.700	0.000
	Good	s / D	0.000	0.030	0.047	0.480
		$\tau_b / \sqrt{0.8\, f_{cu}^{'}}$	0.500	2.000	0.700	0.000
	Bad	s / D	0.000	0.040	0.047	0.480
		$\tau_b / \sqrt{0.8\, f_{cu}^{'}}$	0.500	1.000	0.700	0.000
$f_c^{'} > 60$	Excelent	s / D	0.000	0.012	0.030	0.340
		$\tau_b / \sqrt{0.88\, f_{cu}^{'}}$	0.600	2.500	0.900	0.000
	Good	s / D	0.000	0.020	0.030	0.340
		$\tau_b / \sqrt{0.88\, f_{cu}^{'}}$	0.600	1.900	0.900	0.000
	Bad	s / D	0.000	0.025	0.030	0.340
		$\tau_b / \sqrt{0.88\, f_{cu}^{'}}$	0.600	1.100	0.900	0.000

For a cyclic loading analysis, an additional model is available called memory bond material. This model uses the previously mentioned bond-slip models as a backbone. Once the bond stress sign changes, an additional parameter τ_1 determines the maximum bond stress. τ_1 lies between $\tau_{res} \leq \tau \leq \tau_{max}$. The residual bond stress is the last value from the bond strength-bond slip function.

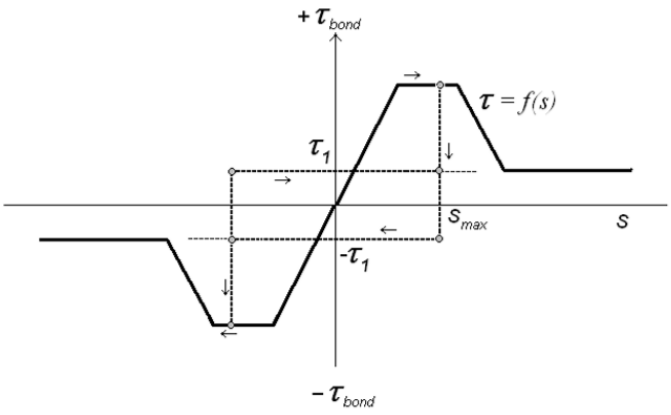

Figure 3–7: Memory bond working diagram (Cervenka et al., 2018).

So

$$s_i = s_{i-1} + \Delta s_i \tag{3.23}$$

The loading range $|s| \geq s_{max}$

$$\tau = f(s) \tag{3.24}$$

The unloading range $-s_{max} < s < s_{max}$

$$\Delta s \geq 0 \qquad \tau = \tau_1 \tag{3.25}$$

$$\Delta s \leq 0 \qquad \tau = -\tau_1 \tag{3.26}$$

CHAPTER 4: BASED MODEL AND INPUT PARAMETERS

The author modeled the geometry of the test specimen in the GID interface, introducing a series of simplifications to achieve a faster run process. The simplifications consisted in:

- Where elastic behavior was observed in the test, the author added an elastic material (instead of reinforced concrete), i.e., the hammerhead and footing.
- A point displacement at mid-height and mid-width of the hammerhead (instead of two points used in the test) introduced the displacement protocol.

A unique feature was the post-tensioning rods which applied the additional axial load to the column see Figure 2–5. The fixity points of the rods are the bottom of the reaction floor, from this point the PT follows the trajectory of the hammerhead adding P-δ effect to the overall behavior.

In the model, the PT rods were modeled as external cables (*CCExternal Cable*), applying the prestress as an initial strain. Applying the prestress as initial stress did not introduce an axial load to the system. The Young's Modulus was made equal to $E_{PT}/10$ to emulate the test setup where the force in these rods was actively controlled and maintained reasonably constant.

Figure 4–1 shows the fix-points of the PT rods. For this, the footing considered the height of the reaction floor and the footing itself.

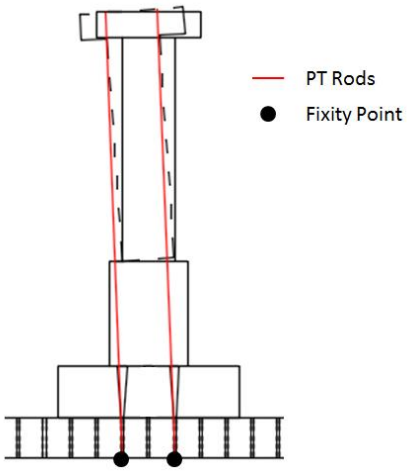

Figure 4–1: Fixity point of post-tension rods.

At the interface between the column pier and the shaft, a slim volume of 3 in. height placed at the base of the column was set to consider the cold joint formed in this region. It had the same properties as the plastic hinge with a reduce tensile strength.

4.1 MATERIALS FOR VOLUME ELEMENTS

Figure 4–2 shows the list of materials used for volume elements in the model.

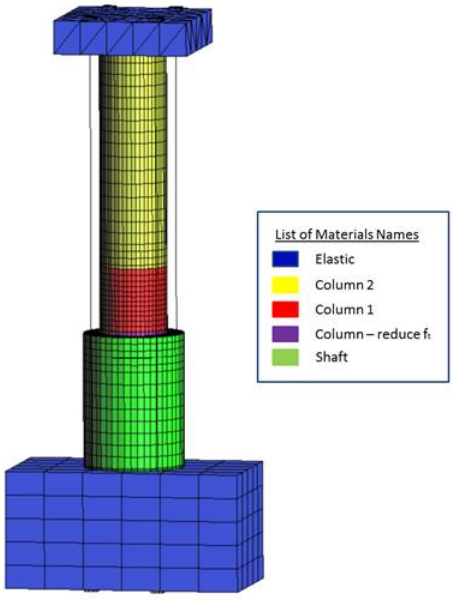

Figure 4–2: Color code of concrete materials used.

Table 4-1 shows the parameters used. These are required to use *CC3DNonLinCementitious2* explained in Chapter 3.1. The author used the compression strength and Young's modulus obtained from the concrete cylinder compression tests given in Chapter 2.2. The researcher only performed one split-cylinder test for this project, which provided a tensile strength of 0.45 ksi.

Activation of crack spacing and minimum crack spacing was not necessary to introduce since the mesh was refined enough. The tension stiffening, aggregate interlock, the shear factor (s_F) and the unloading factor (f_U) were not activated.

Since there was no experimental data of the fracture energy G_{ft} (no wedge-splitting test), the author used the formulation proposed by Vos (1983) and given by ATENA manuals.

$$G_{ft}[MN/m] = 0.000025 f_t'[MPa] \quad (4.1)$$

The formulation given above was calibrated using results by Peterson (1981) , shown in Figure 4–3, and considering that the tensile strength is within the upper 95% limit proposed by CEB-FIP.

The fixed-crack material parameter determines at which maximum residual tensile stress level the crack direction gets fixed. In other words, 0 means the use of a fully rotated crack model, and 1 means using a fixed-crack model (Chapter 3.1). Values between 0 and 1 determine the crack direction locking level. For example, using 0.7 fixes the crack direction as soon it opens so far that the softening law drops to 0.7 times the initial tensile strength. A fully rotated cracked model was used (value set as 0).

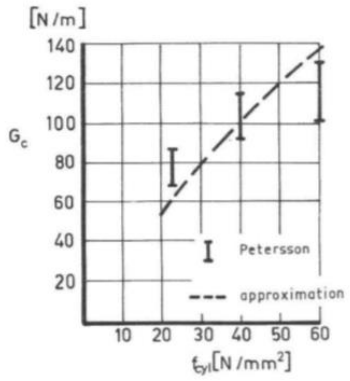

Figure 4–3: Calibration of fracture energy versus cylindrical compressive strength (Vos, 1983).

The plastic strain at peak load called ε_{cp} was determined by dividing the compressive strength by Young's modulus. f_{c0} corresponded to the onset of nonlinearity and determined as the average of the values found with the experimental data given in Chapter 2. Figure 4–4 shows both of these parameters.

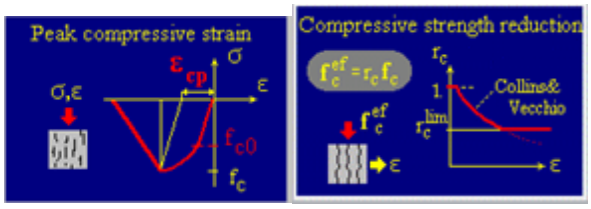

Figure 4–4: Left figure: Peak compressive strain and onset of crushing. Right figure: compressive strength reduction (ATENA ®).

w_d corresponds to the critical compressive displacement explained in Chapter 3.1. F_c reduction is a parameter that reduces the compressive strength due to cracking. Figure 4–4 shows the r_c value.

In the *miscellaneous* parameters: the density of the material is set; this parameter is for a dynamic problem (not the case of this study). The thermal expansion coefficient is also set, which would not influence the research. The eccentricity is the parameter defining the shape of the failure surface, explained in Chapter 3.1, and kept as the 0.52 recommended by Cervenka

Consulting. The last parameter corresponds to the direction of the plastic flow β mentioned in Chapter 3.1, the values given can vary in a range between -5 and 5, where a negative value corresponds to compaction and a positive to expansion. Figure 4–5 shows the schematic return direction with a positive, zero or negative plastic flow.

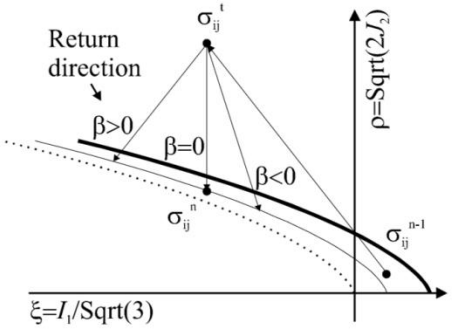

Figure 4–5: Return plastic flow direction (Cervenka et al., 2018).

Table 4-1: Input parameters for volume elements.

	Shaft	Column reduce f_t	Column 1	Column 2
Concrete				
Base Material Prototype	CC3DNonLinCementitious2			
Young's Modulus [ksi]	3695.7	3751.3	3751.3	3557.7
Poisson Ratio	0.20	0.2	0.2	0.2
Tension Strength [ksi]	0.45	0.1	0.45	0.45
Compression Strength [ksi]	-4.93	-5.17	-5.17	-5.08
Tensile				
Activate Crack Spacing	no	no	no	no
Crack spacing	-	-	-	-
Activate crack spacing min	no	no	no	no
Crack spacing min	-	-	-	-
Activate tension stiffening	no	no	no	no
Tension stiffening	-	-	-	-
Activate aggregate interlock	no	no	no	no
Aggregate Size [in.]	-	-	-	-
Activate shear factor	no	no	no	no
Shear factor	-	-	-	-
Activate unloading factor	no	no	no	no
Unloading factor	-	-	-	-
Fracture energy [lb. /in.]	0.44	0.44	0.44	0.44
Fixed-crack	0	0	0	0
Compressive				
Plastic Strain EPS-CP	-0.0013	-0.0014	-0.0014	-0.0014
Onset of crushing Fco (linearity limit) [ksi]	-2.33	-2.88	-2.88	-2.73
Critical comp disp-WD [in.]	-0.197	-0.197	-0.197	-0.197
Fc Reduction	1	1	1	1
Miscellaneous.				
Rho-Density [lb./in.^{3}]	8.67E-08	8.67E-08	8.67E-08	8.67E-08
Thermal Expansion Alpha [F^{-1}]	6.67E-06	6.67E-06	6.67E-06	6.67E-06
Eccentricity-EXC	0.52	0.52	0.52	0.52
Dir. of Plastic Flow-BETA	0	0	0	0

4.2 MATERIALS FOR 1D ELEMENTS

Figure 4–6 shows the list of materials used for the 1D element in the model. These correspond to the mild reinforcement used in the column and shaft and the post-tension reinforcement.

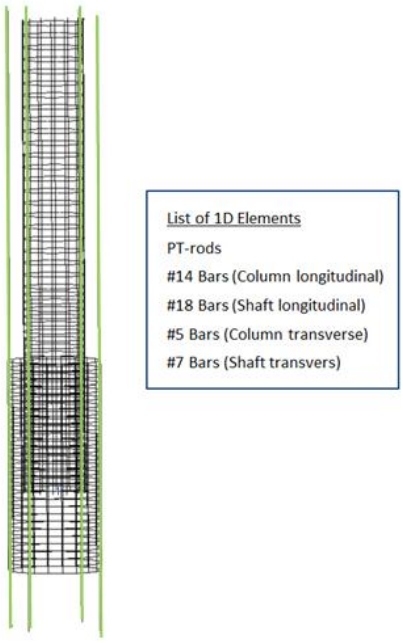

Figure 4–6: List of 1D element names.

Table 4-2 shows the input parameters that characterize the mild reinforcement used in the column and shaft, based on the coupon tests. For #7 since there was no data available, the author based the stress-strain on the #6 results. The longitudinal reinforcement used a four linear function to describe the backbone curve. The transverse reinforcement used a three linear function for the backbone curve. For the cyclic response, the author used the Menegotto-Pinto built in ATENA ®.

In the *miscellaneous* parameters, the density and thermal expansion parameters were set; however, these are not used during the analysis. If the reinforcement in compression is activated,

the element will have the same backbone curve for tension and compression. If the reinforcement has low bending stiffness is recommended not to enable this setting, to simulate the buckling in the reinforcement under compressive forces.

In the *element geometry* parameters, the type of geometrical non-linearity (linear or nonlinear) is introduced. Here the type of bond is set, by default the program considerers the bar to be perfectly bonded with the surrounding volume elements. The settings for *embedded short bars* and *quadratic elements* indicate if the volume elements have quadratic interpolation functions between nodes and if the rebar is smaller than the 3D volumes (coarser mesh).

Table 4-3 shows the input parameters used for the bond law of the longitudinal reinforcement of the column. A user-defined function was used for the base model.

Table 4-2: Input parameters for mild reinforcement.

		No 18	No 14	No 5	No 7
Basic					
Material Prototype		CCyclingReinf			
Young's Modulus	[ksi]	29123	27760	28160	29000
Profile	[in.]	2.25	1.75	0.625	0.875
Number of profiles		1	1	1	1
Reinforcement Function					
Yield Strength YS	[ksi]	81.9	87	87.8	84.6
Number of multilinear values		5	5	4	4
eps2	[-]	0.01497	0.02393	0.0192	0.02533
f2	[ksi]	90	100	105	105
eps3	[-]	0.03233	0.033	0.04367	0.05067
f3	[ksi]	100	105	114	115
eps4	[-]	0.061	0.06567	0.1109	0.10624
f4	[ksi]	108	113	115	119.5
eps5	[-]	0.11904	0.1134	-	-
f5	[ksi]	110.4	114.3	-	-
Menegotto-Pinto					
Bauschinger exp-R		2	2	2	2
C1		5000	5000	5000	5000
C2		20	20	20	20
Miscellaneous					
Rho Density	[lb./in.^{3}]	0.284	0.284	0.284	0.284
Thermal Expansion-Alpha	[F^{-1}]	6.7E-06	6.7E-06	6.7E-06	6.7E-06
Active in compression		yes	yes	yes	yes
Element Geometry					
Name		#18 shaft	#14 col	#5 col	#7 shaft
Geometrical Non-Linearity		Non-Linear	Non-Linear	Linear	Linear
Geom Type		Normal	Bar with memory bond	Normal	Normal
Embedded Reinf.		yes	yes	yes	yes
minimum	[in.]	2	2	2	2
Embedded short bars		yes	yes	yes	yes
Quadratic elements		no	no	no	no
default application		yes	yes	yes	yes

Table 4-3: Input parameters for bars with a bond.

	No 14
Bar with memory bond	
Bar end	fixed none
max bond strength	1000 psi
friction unload coefficient	50 psi
function for bond slip	From user
slip (length unit) 1	0 [in.]
bond strength 1	0.1 [-]
slip (length unit) 2	0.04 [in.]
bond strength 2	1 [-]
slip (length unit) 3	0.07 [in.]
bond strength 3	1 [-]
slip (length unit) 4	1.72 [in.]
bond strength 4	0.4 [-]

For the post-tension rebar Table 4-4 and Table 4-5 shows the parameters used.

Table 4-4: Input parameters for Post-tensioned rebar.

Basic		
Material Prototype		CCyclingReinf
Young's Modulus	[ksi]	2900
Profile	[in.]	1.75
Number of profiles		1
Reinforcement Function		
Yield Strength YS	[ksi]	140
Number of multilinear values		2
eps2	[-]	0.6
f2	[ksi]	150
Menegotto-Pinto		
Bauschinger exp-R		4
C1		500
C2		50
Miscellaneous		
Rho Density	[lb./in.^{3}]	0.2836
Thermal Expansion-Alpha	[F^{-1}]	6.67E-06
Active in compression		no

Table 4-5: Input parameters for Post-tensioned rebar.

Element Geometry	
Name	PT
Geometrical Non-Linearity	Linear
Geom. Type	cable
Embedded Reinforcement	no
Embedded short bars	no
Quadratic elements	no
Default application	yes

4.3 MESH AND PROCESS SETTINGS

The program assigns the mesh independently for each volume. Table 4-6 shows the type of element used. Linear interpolation functions between nodes were used. ATENA meshes the linear elements directly. The program creates a node at each intersection with a volume element.

Table 4-6: Element type for the mesh of volumes.

Volume	Element Type
Hammerhead	Tetrahedra
Column	Hexahedra
Shaft	Hexahedra
Footing	Hexahedra
Steel Plates	Tetrahedra

Figure 4–7 shows the prescribed number of element in height indicated for the volumes that represent the column, shaft, and footing. Also, the picture displays the quality of the mesh for the tetrahedra and hexahedra. The column and shaft had the same mesh in plan view, so each node at the shaft-column interface connected both elements. The mesh at the interface is visible in Figure 4–8.

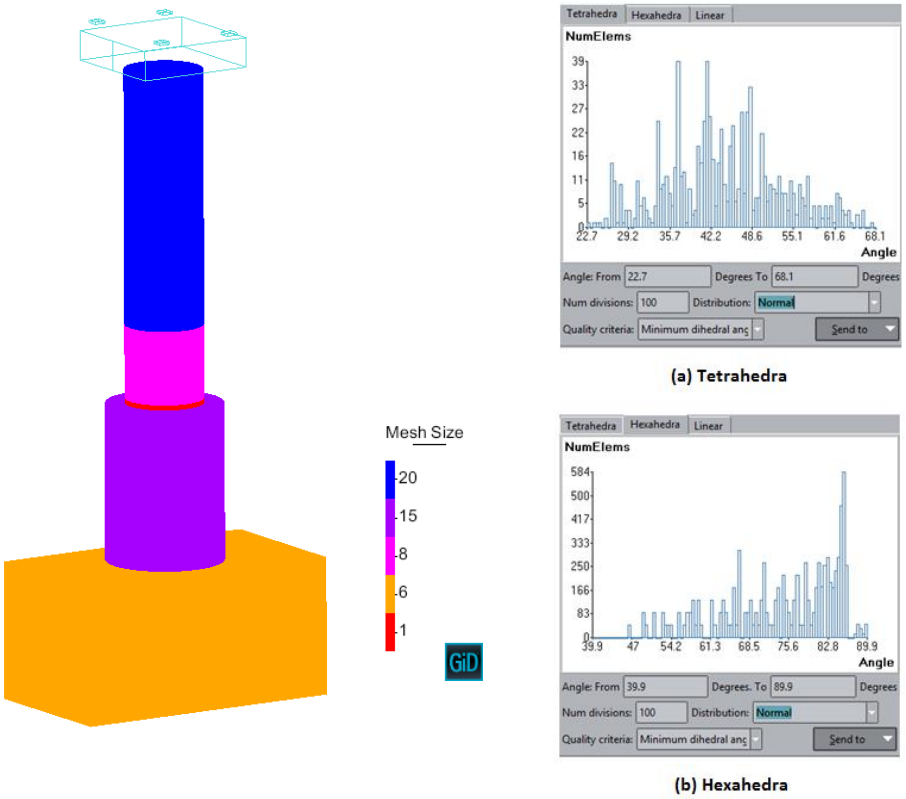

Figure 4–7: Volume mesh size (number of divisions in height) and mesh quality for (a) Tetrahedra elements and (b) hexahedra elements.

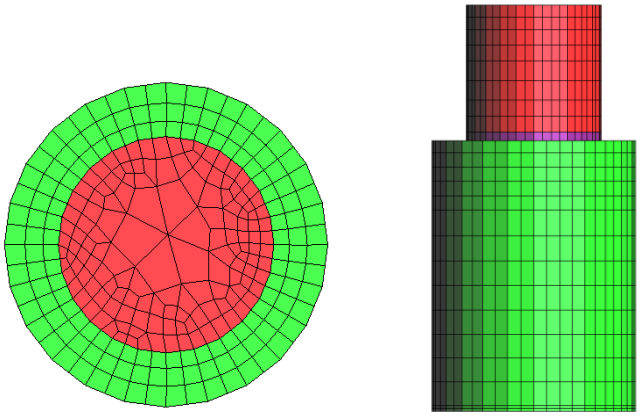

Figure 4–8: Section cut of column mesh at the column-shaft interface.

Three master-slave conditions were used to connect the volume elements that did not share nodes (mesh independently). These interfaces were the hammerhead to the column, the

shaft with the footing, and the steel plates with the hammerhead and footing. The master condition is given to the volume with the coarser mesh.

Table 4-7 presents the problem data setups. The method of resolution of the nonlinear static problem was set as Modified Newton-Raphson. The process was analyzed leaving one core of the system free (number of threads). And two processes were run simultaneously. The computer in which it was analyzed had 4 cores and 8 logical processors. For the processor type, changing from 32bits to 64bits reduced the time of process significantly.

Table 4-7: ATENA Process Settings.

Global Settings	
Type of problem	Static Analysis
Processor Type	64bit
Number of threads	-1
Solution Parameters	
Method	Newton-Raphson
Displacement Error	0.01
Residual Error	0.01
Absolute Residual Error	0.01
Energy Error	0.0001
Iteration Limit	400
Optimize Band	Sloan
Stiffness Type	Elastic Predictor
Assemble Stiffness Matrix	Each step
Solver	PARDISO
Pardiso Required accuracy	0.00000001

CHAPTER 5: BASE MODEL RESULTS

This chapter presents the comparison between the overall behavior and the specific response between the base model and the test. As mentioned in Chapter 2, the test specimen was heavily instrumented with vertical potentiometers (LVDT). The author replicated the monitor points in the model, with the same vertical location, but for modeling convenience, the horizontal distance was kept constant and differed from the test specimen. Table 5-1 shows the horizontal spacing for the model monitoring points.

Table 5-1: Monitor horizontal distance in model.

	Horizontal distance [ft.]
Shaft	3
Column	2

The author divided the column into two sections: column 1 that represents the first 48 in. and is where the plastic hinge developed; and column 2 which corresponds to the upper part of the column. So, the first three panels of vertical potentiometers relate to the results shown as column 1, and the last four panels are considered column 2.

The comparative analysis presented considered checking the following graphs:

- Actuator Load v/s Displacement at mid-height mid-width of the hammerhead.
- Normalized moment-curvature at the plastic hinge.
- Normalized moment - curvature at the shaft-column interface.
- Lateral deflection contributions.
- Strains in south and north bars at peak displacements.

In the following, an explanation of how the author developed these graphs from the model data is presented.

Actuator Load v/s Displacement at mid-height mid-width of the hammerhead.

The program gives directly the reaction at the point where the displacement is prescribed.

Normalized moment - curvature at the plastic hinge.

The author used the following procedure to get the moment and curvature at the plastic hinge region:

Moment:

$$M = R_{act} \cdot \left(H_{col} + \frac{H_{hh}}{2} - H_{cg,\,col\,1\,monitor} - 3[in.]\right) + W_{col} \cdot \left(\frac{M01}{2} - M02\right) + W_{hh} \cdot (M01 - M02) + L_{PT} \cdot cos\,\alpha \cdot (M01 - M02) \quad (5.1)$$

$$\alpha = \text{atan}\left(\frac{M01}{H_{hh}/_2 + H_{col} + H_{shaft} + H_{foot} + H_{lab\,slab}}\right) \quad (5.2)$$

Where:

R_{act}	Actuator Load, [kip].
H_{col}	Column height, [in.].
H_{hh}	Hammerhead height, [in.].
H_{shaft}	Shaft height, [in.].
H_{foot}	Footing height, [in.].
$H_{lab\,slab}$	Laboratory reaction floor height, [in.]

$H_{cg,\,col\,1\,monitor}$ The height of the centroid of gravity of column 1, [in.].

$M01$ Horizontal displacement measure at mid-height mid-width of the hammerhead, [in.].

$M02$ Horizontal displacement measure shaft at mid-width, [in.].

W_{col} The weight of Column (1 and 2), [kip].

W_{hh} The weight of hammerhead, [kip].

L_{PT} Post-tension Load, [kip].

α Angle measure from the original vertical axis to PT-rod alignment, [rad].

Curvature:

$$\theta = \sum_{i=1}^{4} atan\left(\frac{\delta_{LVDT,ib} - \delta_{LVDT,ia}}{24[in.]}\right) \quad (5.3)$$

$$\delta_{LVDT,ia} = z_{i+1a} - z_{ia} \quad (5.4)$$

$$\delta_{LVDT,ib} = z_{i+1b} - z_{ib} \quad (5.5)$$

$$\emptyset = {}^{\theta}/_{dh} \quad (5.6)$$

Where $\delta_{LVDT,ia}$ and $\delta_{LVDT,ib}$ is the relative vertical displacement between point "i" and "i+1" in the same vertical axis a or b. And dh is the vertical distance between the three first panels. An important remark is made to this part, since the curvature was not calculated for each panel, but for the three first panels giving a "smeared" curvature over this region.

The moment is normalized by the cross-section area times the diameter and the compressive strength. The curvature is normalized by the diameter.

Normalized moment - curvature at the shaft-column interface.

Calculation of the moment followed (5.1) where the height multiplied by the actuators forces changes to the one given in (5.7). α is considered as provided in (5.2).

Moment:

$$M = R_{act} \cdot \left(H_{col} + \frac{H_{hh}}{2} - 1.5[in.]\right) + W_{col} \cdot \left(\frac{M01}{2} - M02\right) + W_{hh} \cdot (M01 - M02) + L_{PT} \cdot \cos\alpha \cdot (M01 - M02) \quad (5.7)$$

The curvature follows the same procedure as the one given in (5.6), where only one panel of vertical potentiometers is considered, and dh is equal to 3 in.

Lateral deflection contributions

The displacement contribution considered the flexural response of the shaft, column 1, and column2, and the fixed end rotation (FER). With the rotation at each LVDT the flexural displacement is:

$$\theta_i = atan\left(\frac{\delta_{LVDT,ib} - \delta_{LVDT,ia}}{24[in.]}\right) \quad (5.8)$$

$$\Delta_i = \theta_i \cdot h_i \quad (5.9)$$

h_i is the vertical distance from the center of the LVDT to the top of the hammerhead. Then adding the contribution of the vertical potentiometers placed in each section gives the flexural displacement contribution. Using of the same procedure, but considering a height of 3 in. (at the base of the column), the FER was obtained.

A remark must be made to this calculation, the contribution of each vertical potentiometer was made on its own and then added by region (not the smear contribution by sector).

Figure 5–1 shows a reduced displacement history used to decrease the time of the analysis.

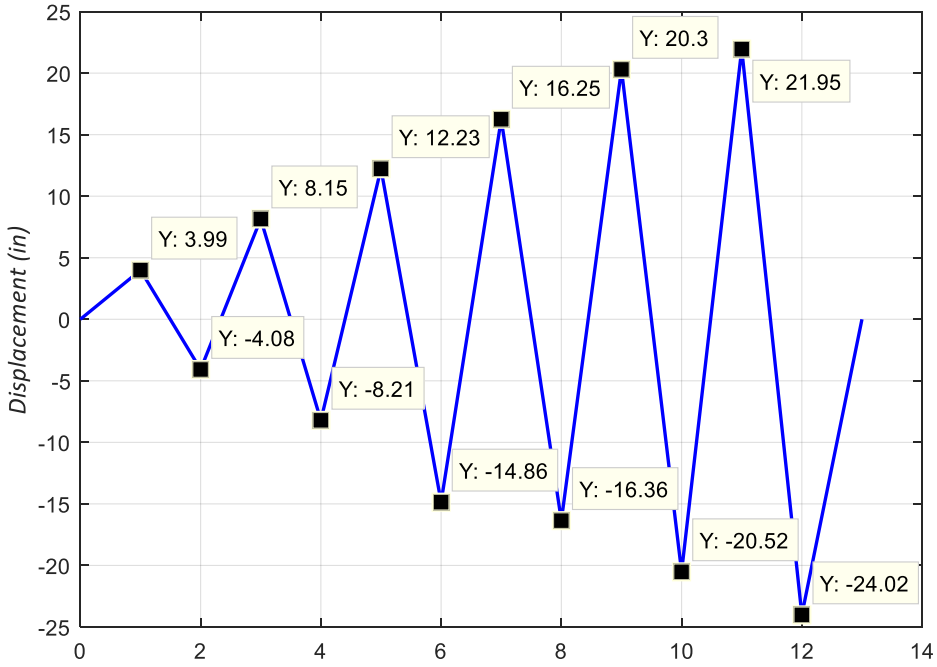

Figure 5–1: Reduce displacement protocol.

Figure 5–2 shows the overall behavior of the test specimen compared with the analytical model. From the graph, the analytical model has convergence issues before the end of the displacement protocol. Figure 5–3 gives a close up by ductility cycle. From this, the overall behavior of the analytical model matches well the specimen behavior. For the first cycle, the dissipated energy of the model is higher than the test. In the second cycle, the model predicts a higher strength of around 10%, and it is not capable of predicting the change in stiffness at the re-loading of the negative cycle. For the third cycle, the strength matches between model and

specimen, but the model is not able to predict the change in stiffness also seen in the second cycle.

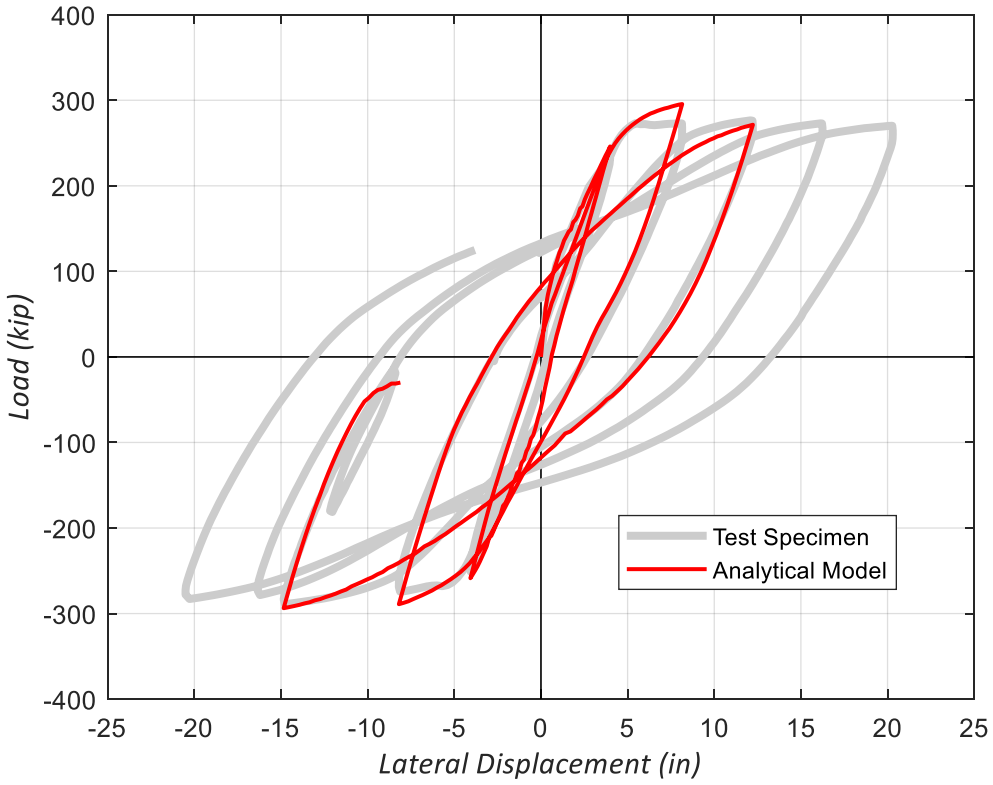

Figure 5–2: Actuator Load versus displacement at hammerhead.

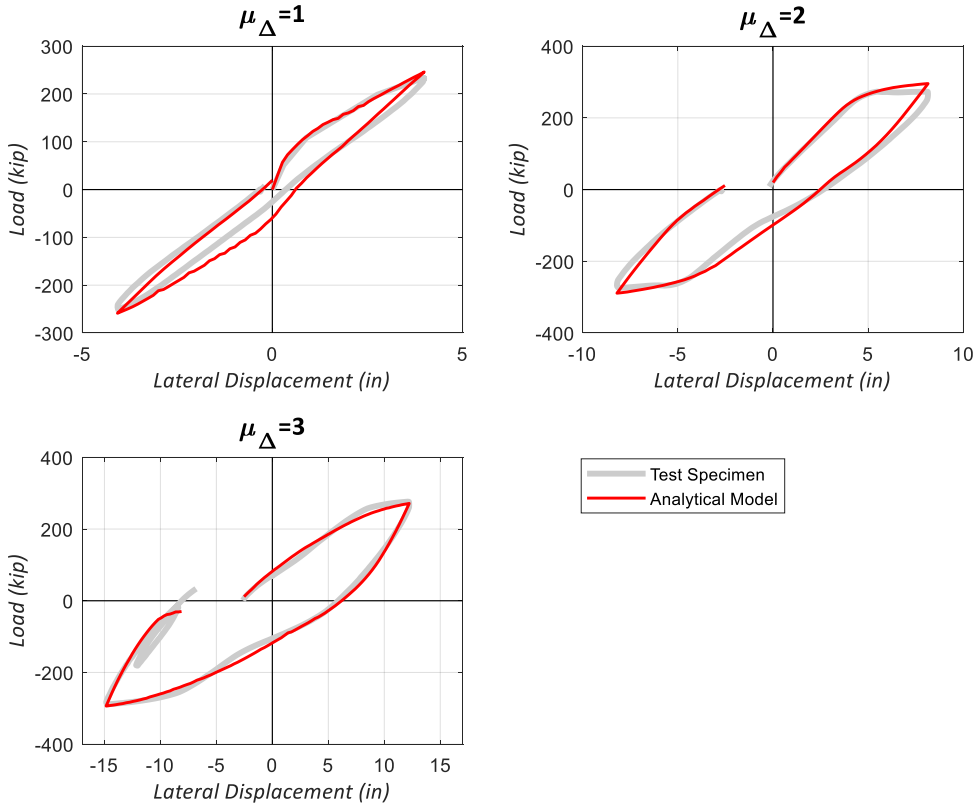

Figure 5–3: Actuator Load versus displacement at hammerhead per ductility displacement cycle.

Figure 5–4 and Figure 5–5 shows the normalized moment curvature of the analytical model and test specimen. Figure 5–4 displays the moment-curvature for the first two displacement ductility cycles, with the yield curvature given by Priestley (2003) for a circular column. The yield strain was obtained from the monotonic tensile test of the #14 bar (0.00313).

$$\emptyset_y = 2.25\,{}^{\varepsilon_{sy}}/_{D} \qquad (5.10)$$

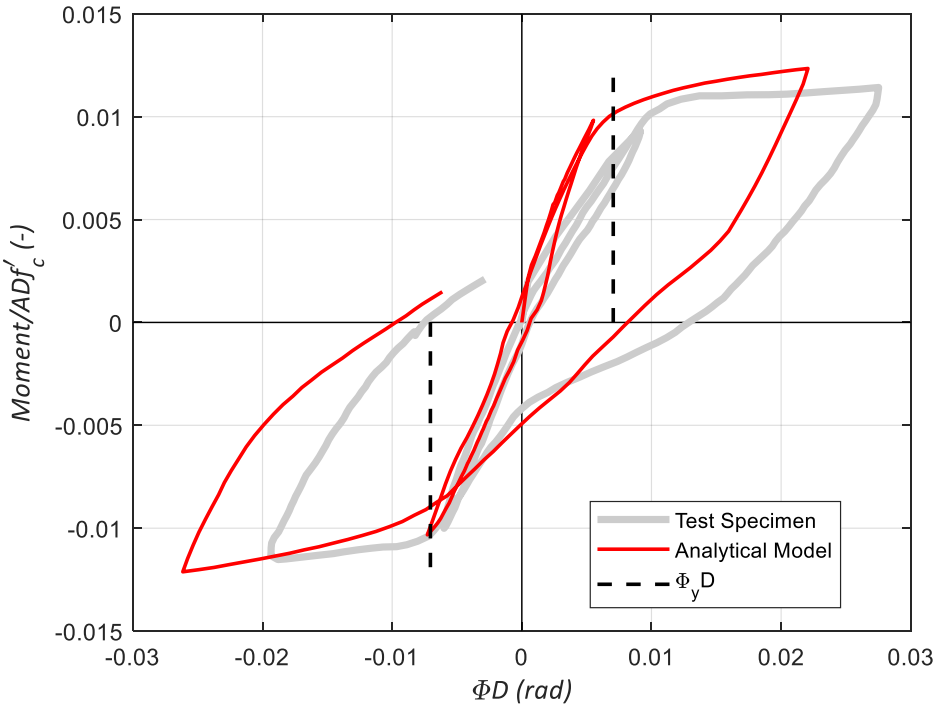

Figure 5–4: First cycles of normalized moment curvature.

From the figure, it is possible to identify that the prediction of the yield curvature given by the model is in good agreement with the one from Priestley. However, the test specimen behaves more elastically for the positive cycle than for the negative, which makes the yield curvature predicted by the formulation to have an offset with the actual one. Also, the test specimen has an asymmetric behavior in the curvature at the first 48 in. of the column. The analytical model predicts an asymmetry. However, this is reduced in comparison with the one from the experiment.

The change in stiffness at the re-loading of the second negative cycle is more pronounced in this region than at the overall behavior. The base model was not able to capture this feature.

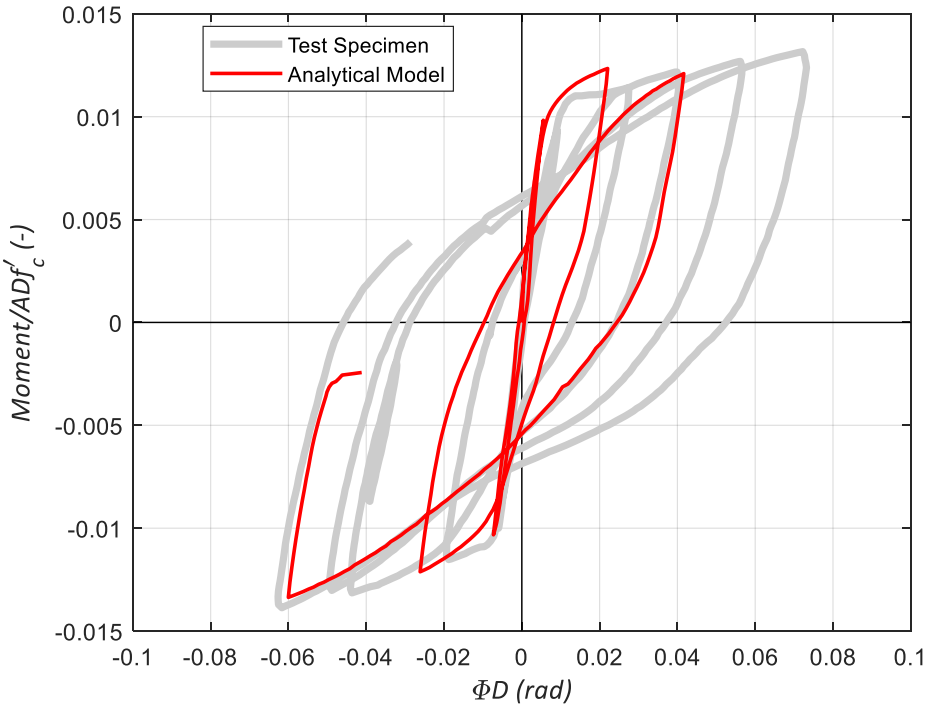

Figure 5–5: Normalized moment-curvature at the plastic hinge region.

Figure 5–5 shows the complete comparison of the normalized moment-curvature curve; this does not present the last displacement ductility cycle for the test (ductility 6). From the figure, the normalized flexural capacity at the peak displacement of the third cycle is in agreement with the one predicted (positive 1%, negative 3% difference), but at the end of the negative cycle, the normalized curvature is 38% off.

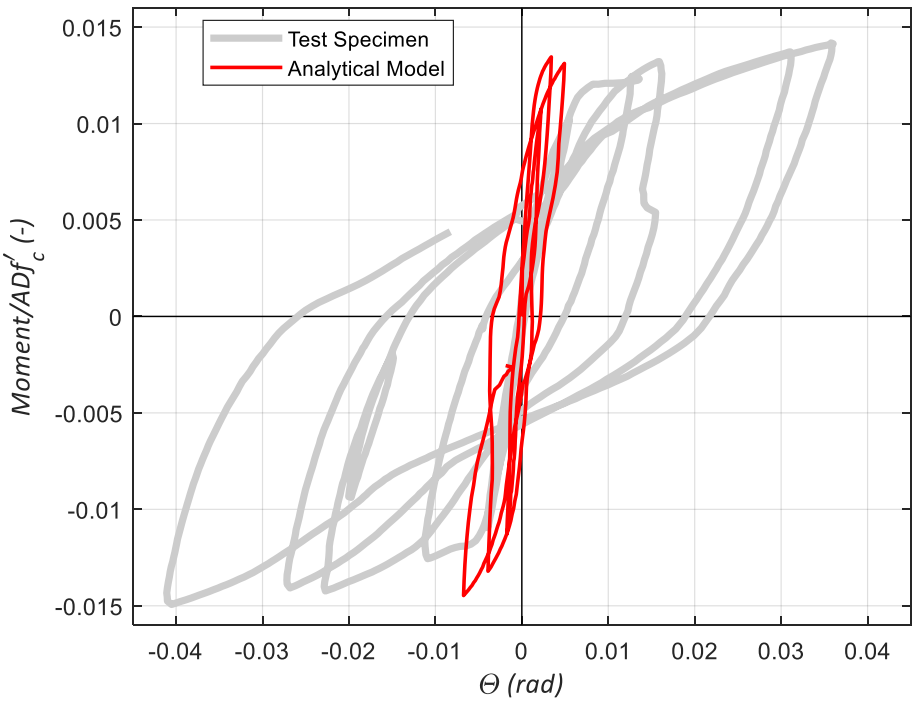

Figure 5–6: Normalized moment-rotation at the column-shaft interface.

Figure 5–6 shows the normalized moment-rotation at the column-shaft interface. The prediction of the model underestimates the rotation capacity at this region. Also, the model predicts a stiffer behavior in the first cycles than the specimen.

Figure 5–7 shows the lateral deflection contribution of the test specimen at the left and at the analytical model at the right. The value from the experiment corresponds to the average of the positive and negative first cycle of the different displacement ductility. The analytical model has convergence issues during the third cycle. Table 5-2 gives the detail and a comparison between the model values and the test values. It is noticeable that the model accounts for a higher flexural displacement at the shaft and it reduces the contribution of the fixed end rotations (FER). At the end of the experiment, the vertical potentiometers at the base of the specimen were not reading any data.

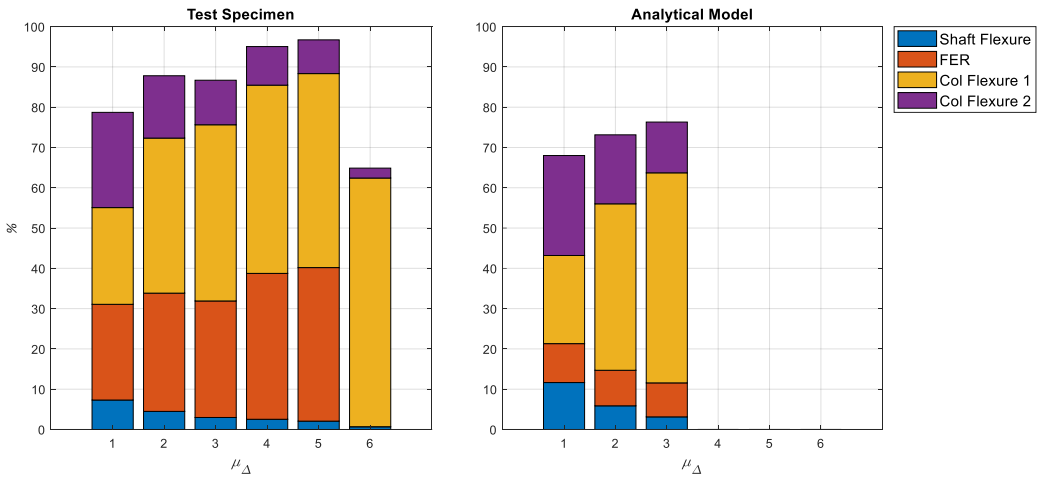

Figure 5–7: Displacement Contribution.

Table 5-2: Displacement contributions.

	Test						Base Model			M/Test		
CDR (%)	1.98	4.01	6.64	7.99	10	11.3	1.98	4.01	6.64	1.98	4.01	6.64
μ_Δ	1	2	3	4	5	6	1	2	3	1	2	3
Shaft	7.3	4.5	3.0	2.5	2.1	0.7	11.7	5.87	3.1	1.59	1.31	1.05
FER	23.8	29.4	28.9	36.2	38.1	0.0	9.66	8.82	8.4	0.41	0.3	0.29
Col1	24.0	38.5	43.7	46.7	48.2	61.7	21.9	41.3	52	0.91	1.07	1.19
Col2	23.6	15.5	11.1	9.6	8.4	2.5	24.8	17.1	13	1.05	1.11	1.14
CDR : Column Drift Ratio												

CHAPTER 6: PARAMETRIC ANALYSIS

A series of analysis ran modifying the material parameters to see the influence in the behavior.

6.1 CONCRETE PARAMETERS

6.1.1 Tension Stiffening (c_{ts})

The factor represents the relative limiting value of tensile strength in the tension softening diagram. Figure 6–1 shows how the tensile stress cannot drop below $c_{ts}f_t$. By CEB-FIP (1990) Model code the recommended value for c_{ts} for an instantaneous loading is 0.4 and for a long-term loading 0.25.

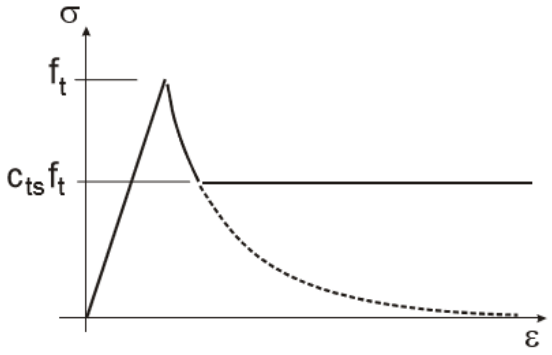

Figure 6–1: Tension stiffening parameter.

Table 6-1: Tension stiffening models and run time.

Model	Modifications	Run Time [hrs.]	Last Step	Run Time [hrs.] @ 300 steps
M1	Not active	10.75	427	7.27
M2	Active with c_{ts} = 0.2	89.50	1108	18.63
M3	Active with c_{ts} = 0.4	37.28	637	10.23
M4	Active with c_{ts} = 0.6	36.28	583	7.91

Table 6-1 presents the different parameters considered for the tension stiffening. The base model recognized this as inactive which gave problems of convergence with at the third loading cycle. Once the tension stiffening is active, the most noticeable from this table is the program can go further on the displacement cycles. By considering the value of c_{ts} as 0.2, the analysis runs until the last positive displacement cycle. The fastest run process until the 300 steps was by considering this factor inactive.

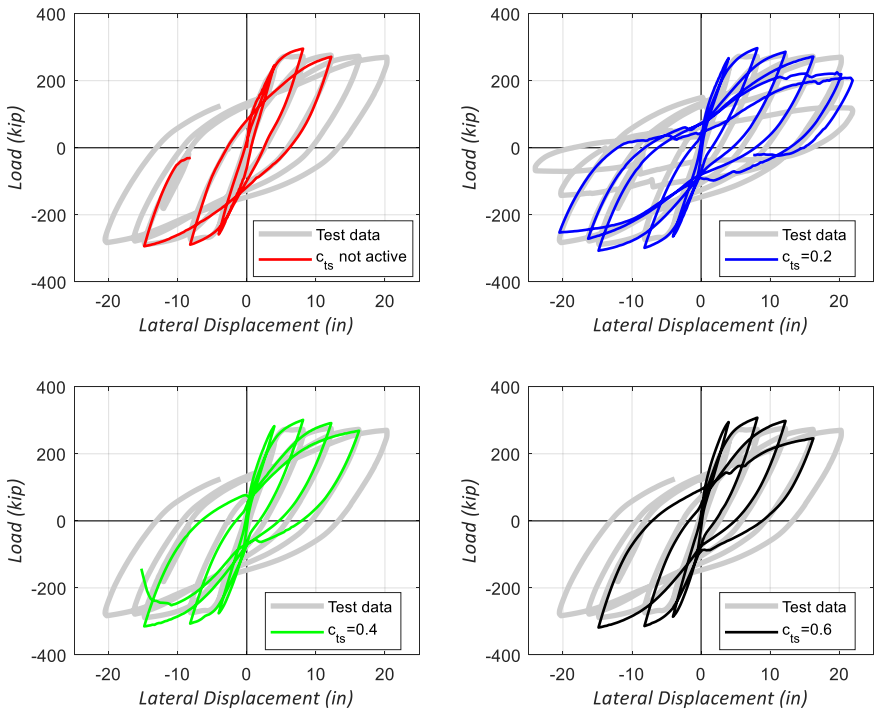

Figure 6–2: Actuator load versus lateral displacement, for different tension stiffening parameters.

Figure 6–2 shows the comparison of the curve load versus displacement. Considering the tension stiffening as active allows the constitutive model to capture pinching in the response. Also, by activating the parameter, improves the convergence of the analysis. For the study with c_{ts} taken as 0.2 (blue curve), the analysis had convergence issues starting the fifth displacement cycle; this translates into the unsmooth curve at this cycle.

For a better comparison purpose, Figure 6–2 shows the first five cycles of displacement ductility. Only the model with c_{ts} equal to 0.2, which goes into μ_{Δ}=6 (Column Drift Ratio (CDR) of 11.3%), the test results exhibits two cycles at μ_{Δ}=5 (CDR=10%) as well as the last displacement ductility.

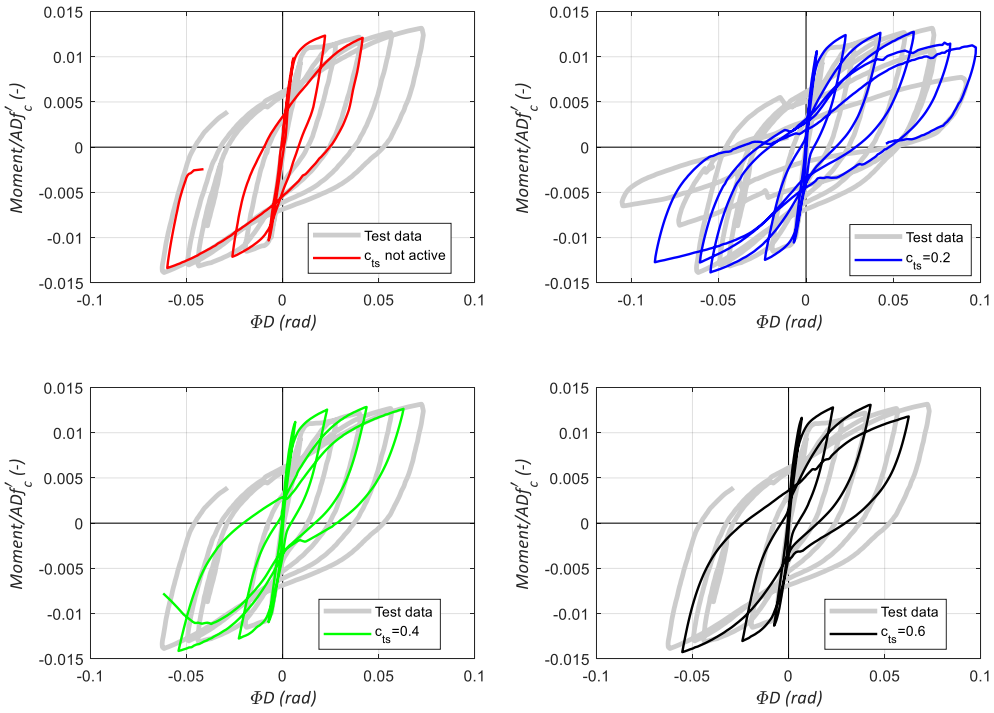

Figure 6–3: Normalized moment curvature at PH region, for different tension stiffening parameters.

Figure 6–3 shows the normalized moment curvature, and Figure 6–4 shows the same graph considering the first two ductility displacement cycles and the yielding curvature given by Priestley (2003) in the latter chapter. As well as Figure 6–2, Figure 6–3 shows the first five cycles of displacement ductility. Only the model with c_{ts} equal to 0.2 shows all the cycles for the test result.

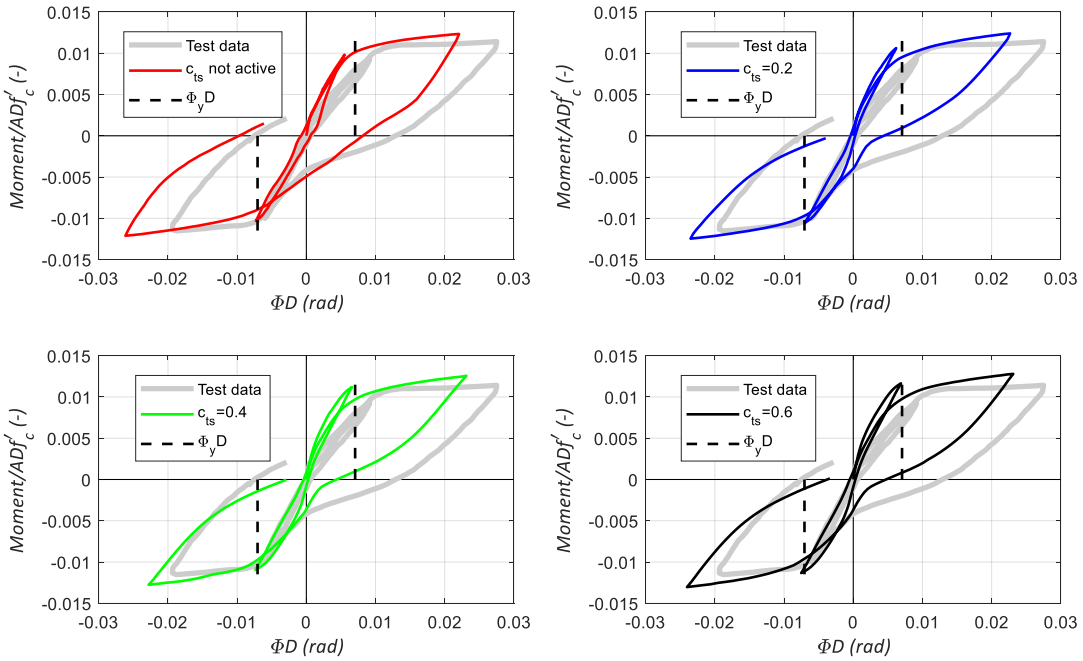

Figure 6–4: First cycles of normalized moment curvature at PH region, for different tension stiffening parameters.

Figure 6–4 shows that the model agrees with the yielding curvature proposed by Priestley, as well as the test for the negative cycle. The main difference between the prediction and test specimen is that the latter is more flexible for the positive cycle, and the yielding curvature is higher than the predicted by the model and the formulation. Between the models, activating the tension stiffening gives a necking on the hysteresis which traduces into lower energy dissipation. All the analyses predict a higher strength than the test for the first two cycles, and all the models predict a fairly symmetric curvature incursion for the positive and negative cycles, but for the test specimen the incursion in curvature it is not symmetric (negative second cycle ΦD of -0.0194 radians and positive cycle ΦD of 0.0275 radians). The area under the curve for the first cycles, for the model without the tension stiffening activated, is higher than the one from the test specimen, and is lesser than the one with the parameter enabled; the model that is closer to the test specimen would be the one without activating it.

Regarding the comparison in the higher cycles, activation of the parameter allows the program to go further on the displacement protocol and allows having a noticeable necking of the curve. The model better captures the strength and curvature at the positive higher cycles. It is important to notice the asymmetry of the test specimen, as well as the over-estimation of the curvature by the model for cycles higher than μ_Δ=3 (CDR=6.64%).

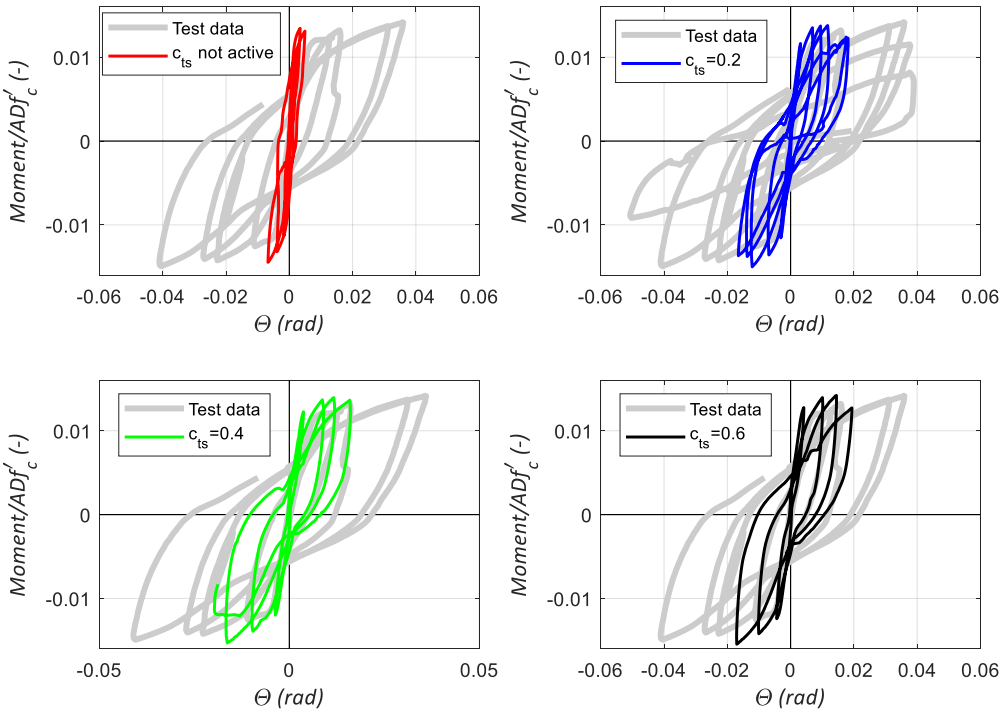

Figure 6–5: Normalized moment-rotation at the column-shaft interface, for different tension stiffening parameters.

Figure 6–5 shows the moment-rotation for the fixed end rotation region. The analysis with the c_{ts} activated resembles the behavior observed in the test. However, the models under-estimate the rotation capacity of this region.

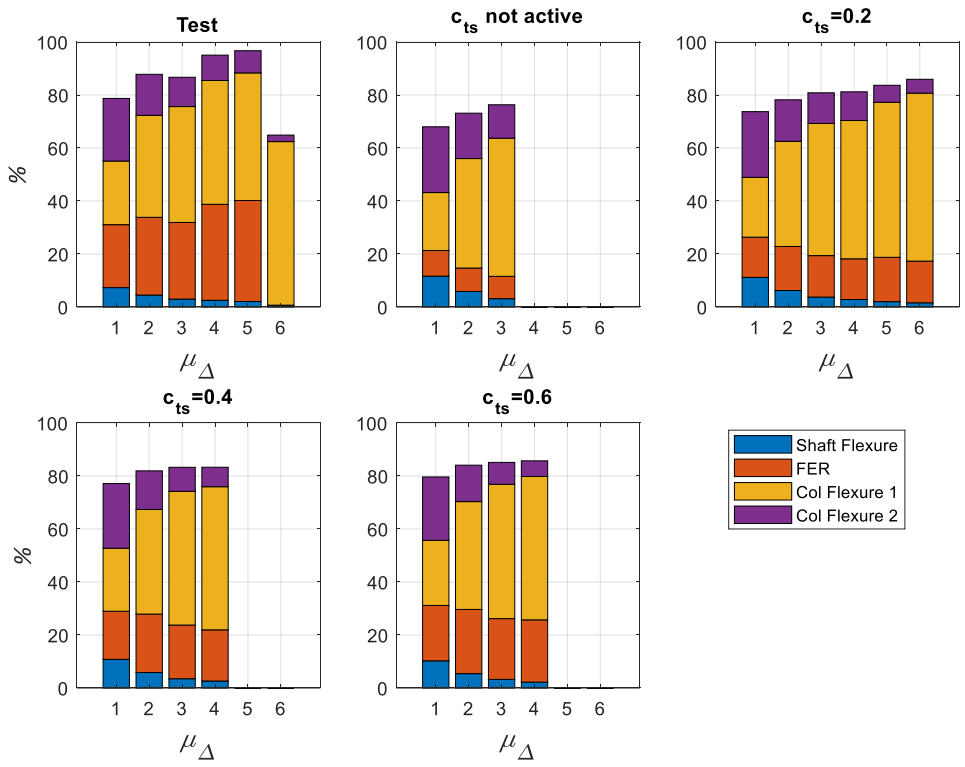

Figure 6–6: Lateral displacements contribution calculated for test specimen and thorough analysis for different tension stiffening parameters.

From Figure 6–6 it is noticeable that activating the tension stiffening allows for an increase in the displacement contribution of the FER. For the model with inactive c_{ts} the contribution is around 9%, and it doubles when it is activated. The model that suits better the distribution is the model considering a value of c_{ts} 0.6, since this is the value that gives a higher matched for the FER.

Table 6-2: Displacement contributions in %, for c_{ts} set to 0.2.

	c_{ts}=0.2						M/Test					
CDR (%)	1.98	4.01	6.64	7.99	10	11.3	1.98	4.01	6.64	7.99	10	11.3
μ_Δ	1	2	3	4	5	6	1	2	3	4	5	6
Shaft	11.2	6.22	3.73	2.82	2.01	1.58	1.53	1.38	1.3	1.11	0.97	2.3
FER	15.2	16.6	15.7	15.4	16.7	15.7	0.64	0.57	0.5	0.42	0.44	-
Col1	22.6	39.7	49.9	52.2	58.5	63.4	0.94	1.03	1.1	1.12	1.22	1.03
Col2	24.8	15.7	11.6	10.8	6.41	5.23	1.05	1.01	1	1.13	0.77	2.12

Table 6-3: Displacement contributions in %, for c_{ts} set to 0.4.

	c_{ts}=0.4				M/Test			
CDR (%)	1.98	4.01	6.64	7.99	1.98	4.01	6.64	7.99
μ_Δ	1	2	3	4	1	2	3	4
Shaft	10.8	5.84	3.49	2.63	1.48	1.3	1.17	1.04
FER	18.2	22	20.3	19.3	0.76	0.75	0.7	0.53
Col1	23.8	39.5	50.5	54	0.99	1.03	1.15	1.16
Col2	24.4	14.6	9.08	7.35	1.03	0.94	0.82	0.77

Table 6-4: Displacement contributions in %, for c_{ts} set to 0.6.

	c_{ts}=0.6				M/Test			
CDR (%)	1.98	4.01	6.64	7.99	1.98	4.01	6.64	7.99
μ_Δ	1	2	3	4	1	2	3	4
Shaft	10.2	5.41	3.2	2.2	1.40	1.20	1.09	0.87
FER	20.9	24.2	22.9	23.5	0.88	0.83	0.79	0.65
Col1	24.6	40.7	50.7	54.1	1.02	1.06	1.16	1.16
Col2	23.9	13.7	8.3	5.9	1.01	0.89	0.75	0.61

6.1.2 Aggregate interlock

The aggregate interlock activates the use of the shear strength of the cracked concrete calculated using the modified compression field theory by Vecchio and Collins (1991). The comparison of enabling it with the maximum size of the aggregate was assessed.

Table 6-5 shows the parameters used and the time that the program took to complete the process. The activation of the setting gives a longer time of analysis, even though the steps analyzed where less.

Table 6-5: Aggregate interlock models and run time.

Model	Modifications	Run Time [hrs.]	Last Step	Run Time [hrs.] @ 300 steps
M1	Not active	10.75	427	7.27
M2	Active with maximum aggregate size (0.75[in.]).	16.88	419	10.6

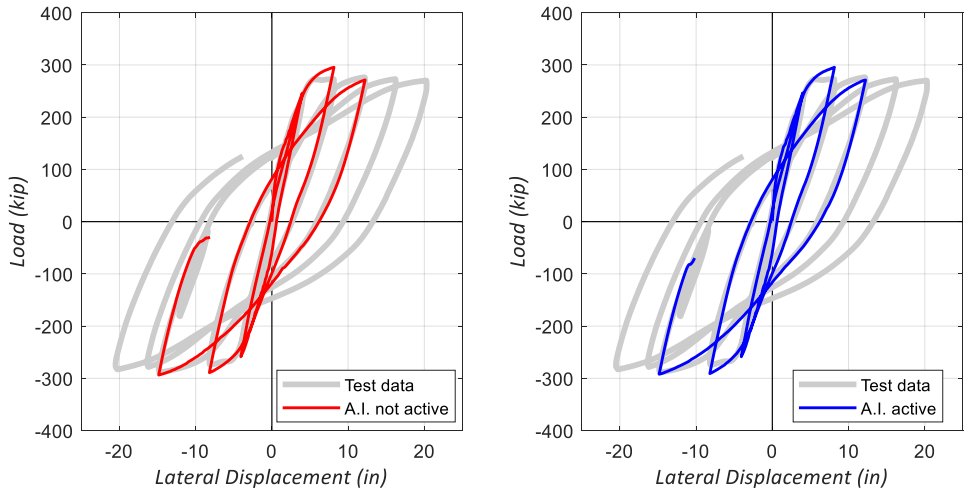

Figure 6–7: Comparison of curve load versus lateral displacement, for different aggregate interlock parameters.

Figure 6–7 shows the comparison of the curve of the applied actuator load and the displacement measure at the hammerhead. The overall behavior is almost identical for both

models. The analyses give an over-estimate of 8% on the strength of the test specimen at the peak of the μ_Δ=2 (CDR=4.01%) and the third peak an under-estimation of around 1.8%.

From the comparison of the normalized moment-curvature of the plastic hinge region shown in Figure 6–8, both models give a higher initial stiffness than the one seen in the test specimen. Also, the initial flexural capacity at the peak of the first cycle is higher. The main difference between the models is the convergence issues that it has by activating the parameter and the higher time that the process takes to run. Moreover, by enabling the setting, the energy dissipation is less than by not activating it. The model gives an additional rotation capacity in the negative cycles in comparison with the test specimen.

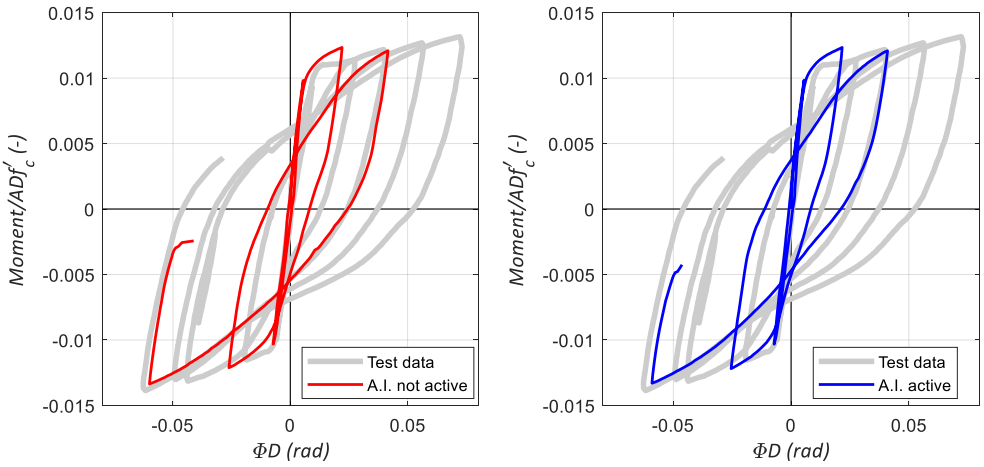

Figure 6–8: Normalized moment curvature at PH region, for different aggregate interlock parameters.

Figure 6–9 shows the first two cycles of the normalized moment-curvature shown in Figure 6–8. The activation of the parameter does not change much the predicted behavior.

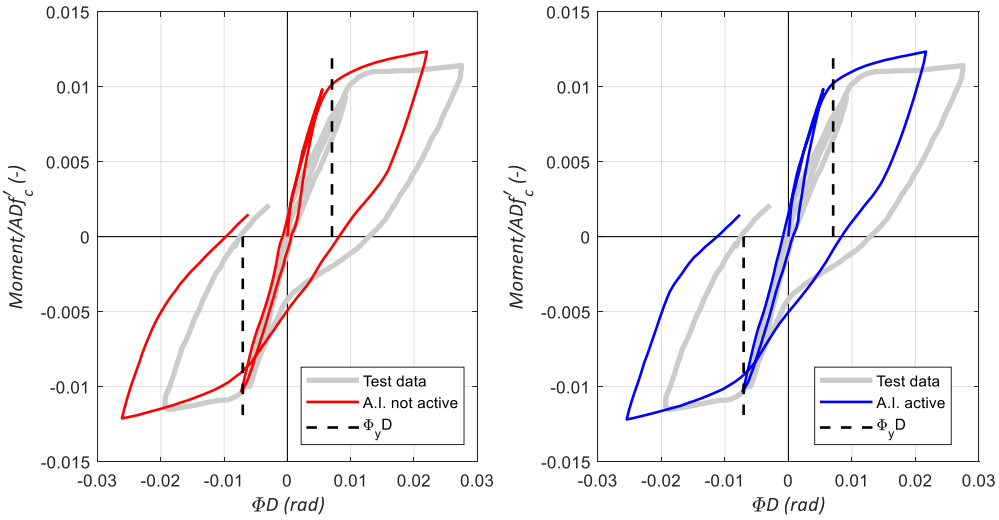

Figure 6–9: First cycles of normalized moment curvature at PH region, for different aggregate interlock parameters.

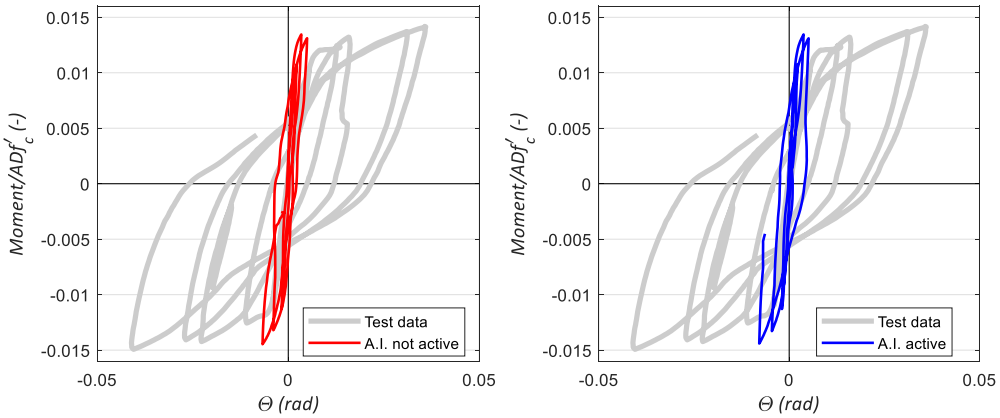

Figure 6–10: Normalized moment-rotation at the shaft-column interface, for different aggregate interlock parameters.

Figure 6–10 shows the normalized moment-rotation for the fixed end rotation. The models under-estimate the rotation and over-estimate the flexural capacity of this region.

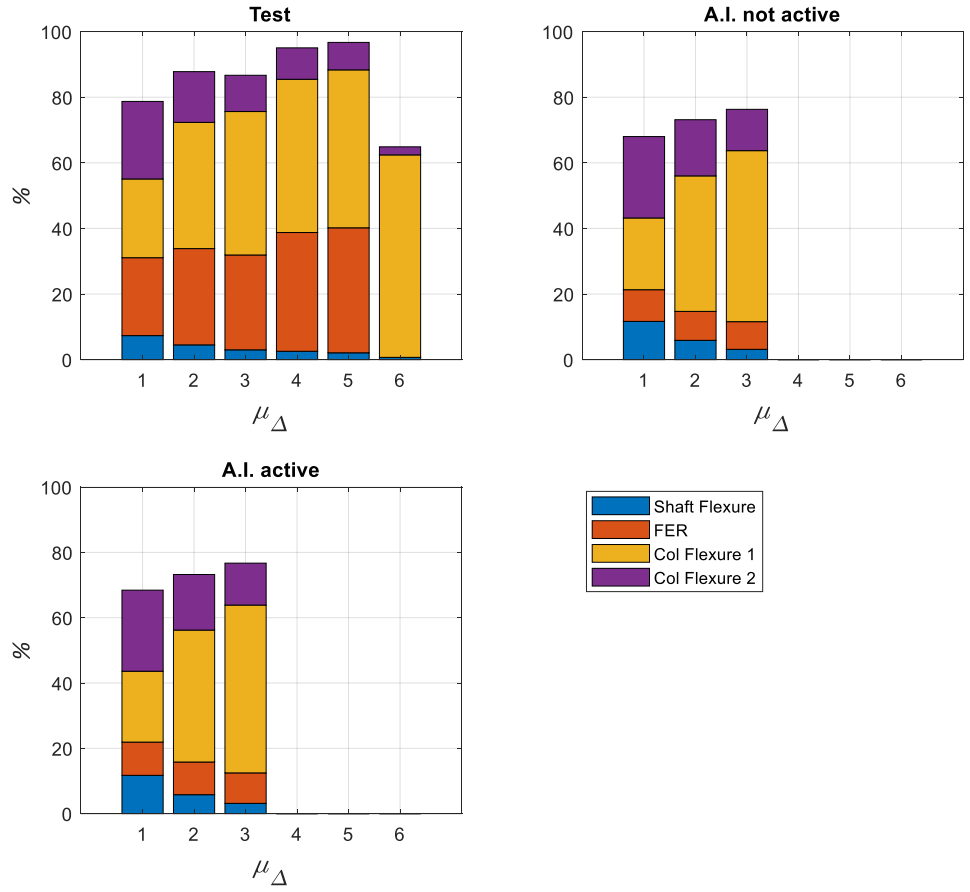

Figure 6–11: Lateral displacements contribution calculated for test specimen and thorough analysis for aggregate interlock parameters.

Figure 6–11 shows the displacement contribution of each section of the column, which is given in detail in Table 6-6. Both models provide roughly the same displacement contributions, where both of them sub-estimate the contribution due to FER.

Activating the parameter does not change in extent the response of the predicted behavior, but it does introduce convergence issues.

Table 6-6: Displacement contributions in %, for aggregate interlock activated.

	A.I. active			M/Test		
CDR (%)	1.98	4.01	6.64	1.98	4.01	6.64
μ_Δ	1	2	3	1	2	3
Shaft	11.5	5.7	3.1	1.57	1.26	1.03
FER	11.1	9.1	8.2	0.47	0.31	0.28
Col1	18.9	37.2	47.0	0.79	0.97	1.07
Col2	24.9	18.3	15.0	1.05	1.18	1.35

6.1.3 Shear Factor (s_F)

The activation of the shear factor s_F will set a value to use in the calculation of cracked shear stiffness. s_F links the stiffness in mode II to mode I. This factor is related to the shear retention factor (β) as follows (Havlásek & Kabele, 2017):

$$D_{II} = s_F D_{I,S} \tag{6.1}$$

$$G_c = \beta G \tag{6.2}$$

$$\beta = \frac{D_{II}}{D_{II}+G} \tag{6.3}$$

A s_F factor of 20 recommended by Cervenka Consulting was used (value based on experiments performed by Walraven 1981) (Cervenka et al., 2018), as well as a value of 200 suggested in the paper "*Prediction of shear failure of large beam based on fracture mechanics*" (Cervenka et al., 2016).

Table 6-7 presents the models analyzed to compare the use of this parameter and the time of the process. The fastest model was the one that did not activate the shear factor parameter. The model with the activation of the setting using the value recommended by Cervenka Consulting was the one who presented convergence issues at the earliest step stage.

Table 6-7: Shear Factor models and run time.

Model	Modifications	Run Time [hrs.]	Last Step	Run Time [hrs.] @ 300 steps
M1	Shear Factor not activated	10.75	427	7.27
M2	s_F= 20 (recommended by ATENA Manual)	13.92	415	10.78
M3	s_F= 200 (recommended in paper, (Cervenka et al., 2016).	21.72	462	12.87

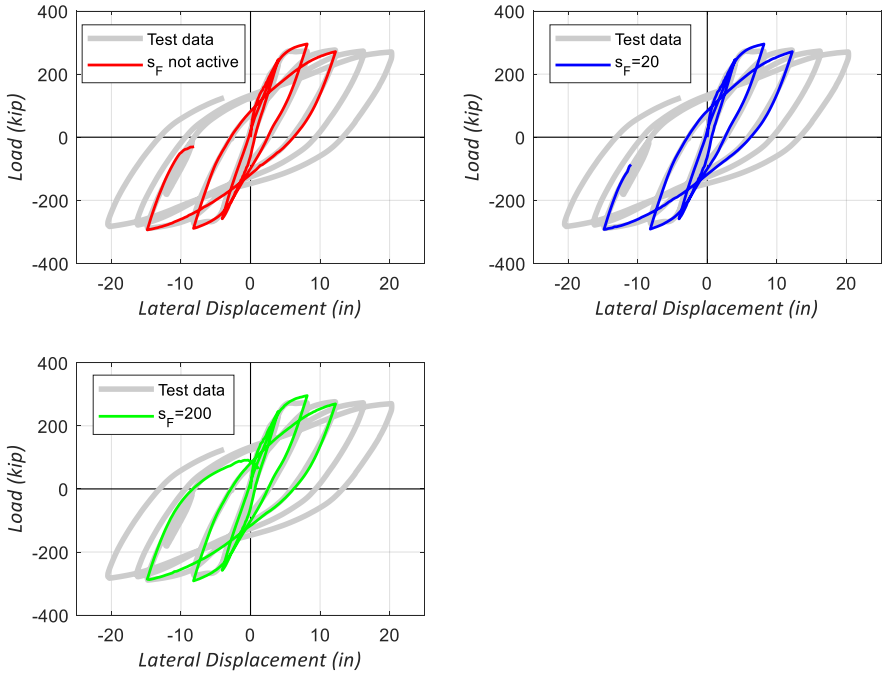

Figure 6–12: Comparison of curve load versus lateral displacement, for different shear factor parameters.

From Figure 6–12, the overall response of the structure at these drift levels does not change by changing s_F. The models over-estimate the strength at the end of the first positive displacement cycle around 8% and under-estimate the strength at the end of the second displacement cycle around 2%. The models do not capture the change in slope at the reloading of the structure, attributed to the closure of the concrete flexural cracks.

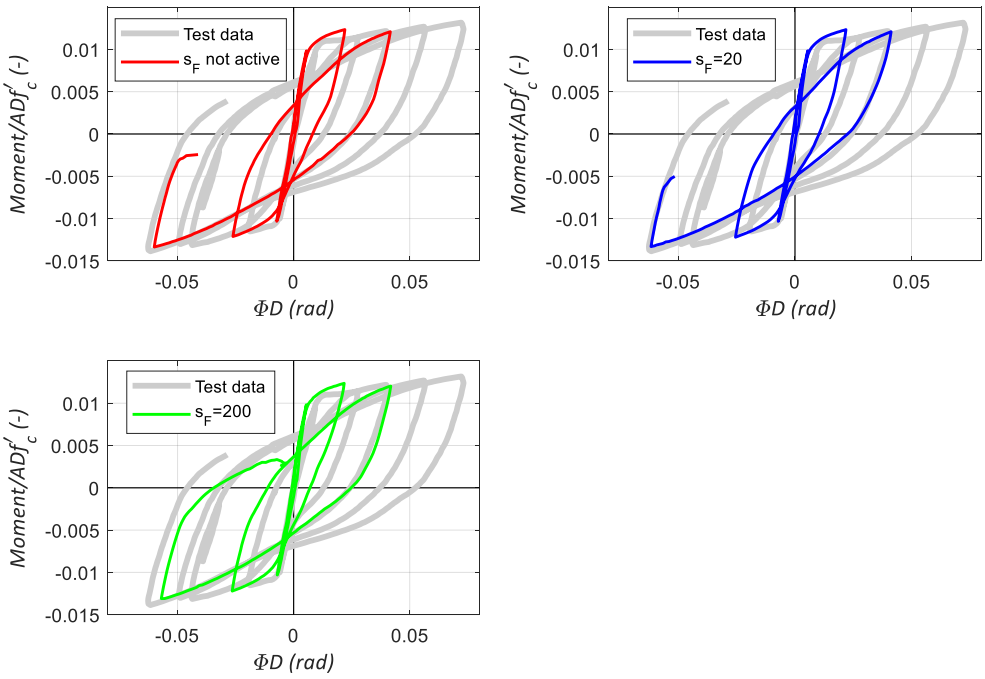

Figure 6–13: Normalized moment curvature at PH region, for different shear factor parameters.

Figure 6–13.shows the normalized moment-curvature at the plastic hinge. The models predict a higher initial stiffness for the positive loading direction. The analyses present a slight variation on the behavior at the unloading of μ_Δ=3 (CDR=6.64%), where the one with a higher shear factor gives a reduction in around 8% of the normalized curvature at the negative peak response, but it is off the experimental results by 33%.

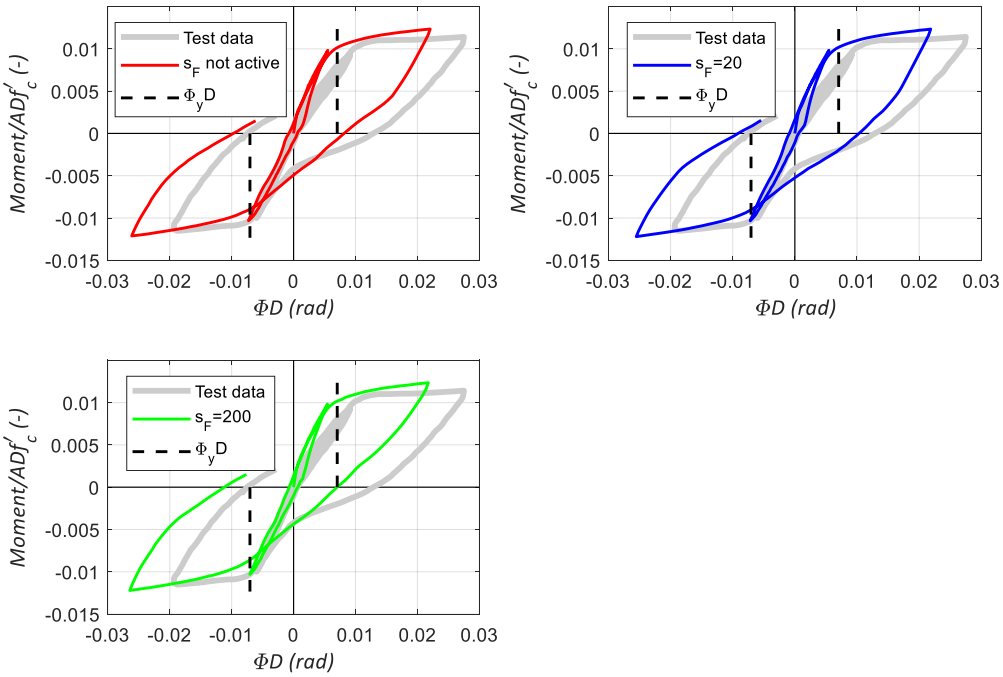

Figure 6–14: First cycles of normalized moment-curvature at PH region, for different shear factor parameters.

Figure 6–14 displays the first two ductility displacement of the normalized moment-curvature at the plastic hinge. The figure also shows, in the segmented line, the yield curvature given by Priestley, which fits well with the model's prediction. However, the test specimen for the positive cycles gives a higher ductility than the one predicted by the model and by Priestley's formulation.

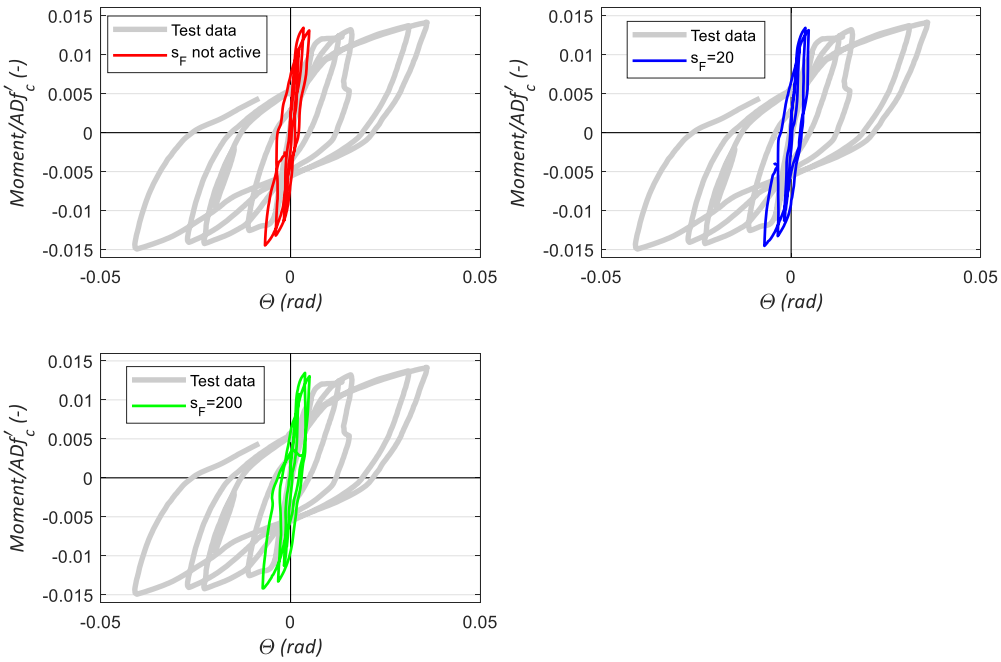

Figure 6–15: Normalized moment-rotation at the shaft-column interface, for different shear factor parameters.

Figure 6–15 shows the normalized moment-rotation at the shaft-column interface. The models do not capture the behavior of this region. The analyses over-predict the stiffness and under-estimates the rotation capacity, compared to the test results.

From Figure 6–16, the displacement contribution does not change much with the variation of s_F. The significant difference would be at the shaft displacement contribution. Table 6-8 shows the percentage of the total displacement that each region contributes and the relation with the test specimen.

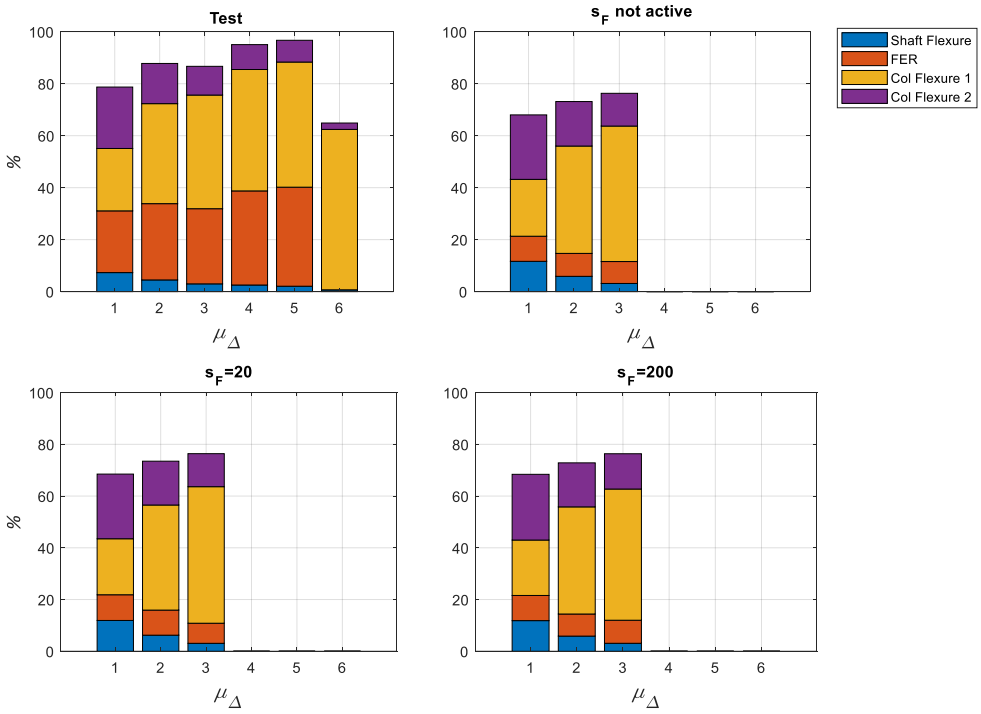

Figure 6–16: Lateral displacements contribution calculated for test specimen and thorough analysis for different shear factor parameters.

Table 6-8: Displacement contributions in %, for different shear factor parameters.

	s_F=20			M/Test			s_F=200			M/Test		
CDR (%)	1.98	4.01	6.64	1.98	4.01	6.64	1.98	4.01	6.64	1.98	4.01	6.64
μ_Δ	1	2	3	1	2	3	1	2	3	1	2	3
Shaft	11.9	6.2	3.1	1.63	1.39	1.03	11.5	5.5	3.0	1.57	1.22	0.99
FER	9.9	9.7	7.8	0.42	0.33	0.27	11.1	9.2	8.1	0.47	0.31	0.28
Col1	21.6	40.6	52.8	0.90	1.06	1.21	18.8	37.4	47.9	0.78	0.97	1.10
Col2	25.0	16.9	12.8	1.06	1.10	1.15	24.9	17.8	15.1	1.05	1.15	1.37

The predicted behavior of the model does not change much by varying this parameter in the range prescribed, but it does introduce convergence issues to the analysis.

6.1.4 Unloading Factor (F_U)

The unloading factor (f_U) controls the crack closure stiffness. This parameter should be higher or equal to 0 and less than 1, where 0 means that the unloading goes to the origin and 1 means that the unloading direction is parallel to the initial elastic stiffness.

Table 6-9 shows the unloading factors used to compare its effect and the time of the process. The base model (Model 1) has the lowest run time. Model 2 has the lowest number of steps analyzed.

Table 6-9: Unloading Factor models and run time.

Model	Modifications	Run Time [hrs.]	Last Step	Run Time [hrs.] @ 300 steps
M1	Not active	10.75	427	7.27
M2	Active $f_U = 0.99$ (values must be less than 1)	12.87	246	-
M3	Active $f_U = 0$	20.15	469	13.32

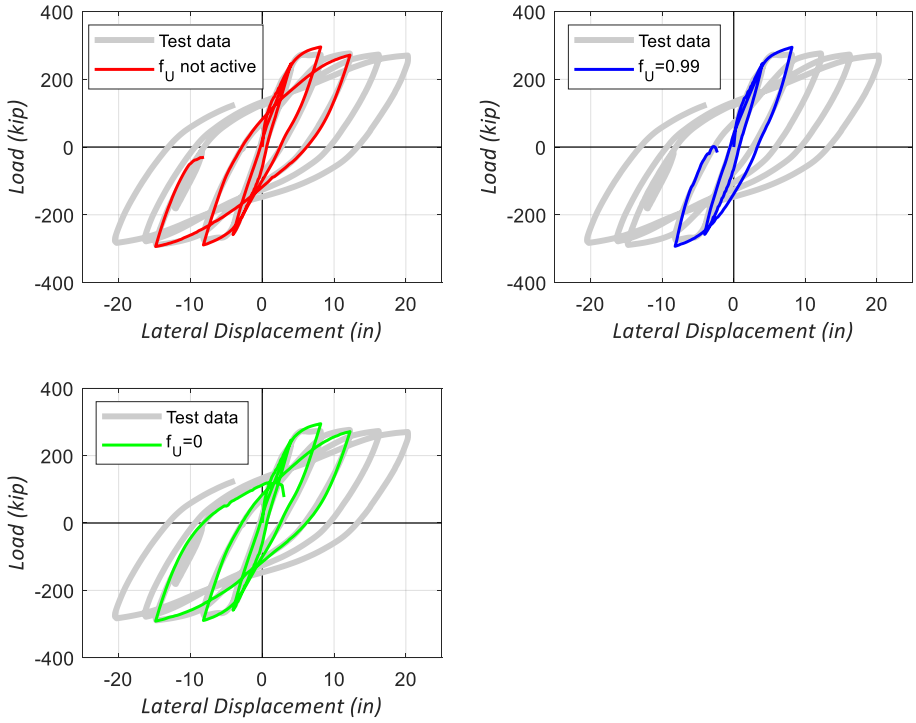

Figure 6–17: Comparison of curve load versus lateral displacement, for different unloading factor parameters.

From Figure 6–17, the three models over-estimate the strength at the end of the μ_Δ=2 (CDR=4.01%) by 8% and it under-estimates by 1.8% at the positive peak of μ_Δ=3 (CDR=6.64%). From the figure, considering the unloading direction as parallel to the initial stiffness gives higher dissipated energy than the actual response of the test specimen, as well as the other models. Not activating this factor, or considering an unloading factor of 0 (unloading goes to the origin), captures better the response of the specimen for the unloading of μ_Δ=1 (CDR=1.98%).

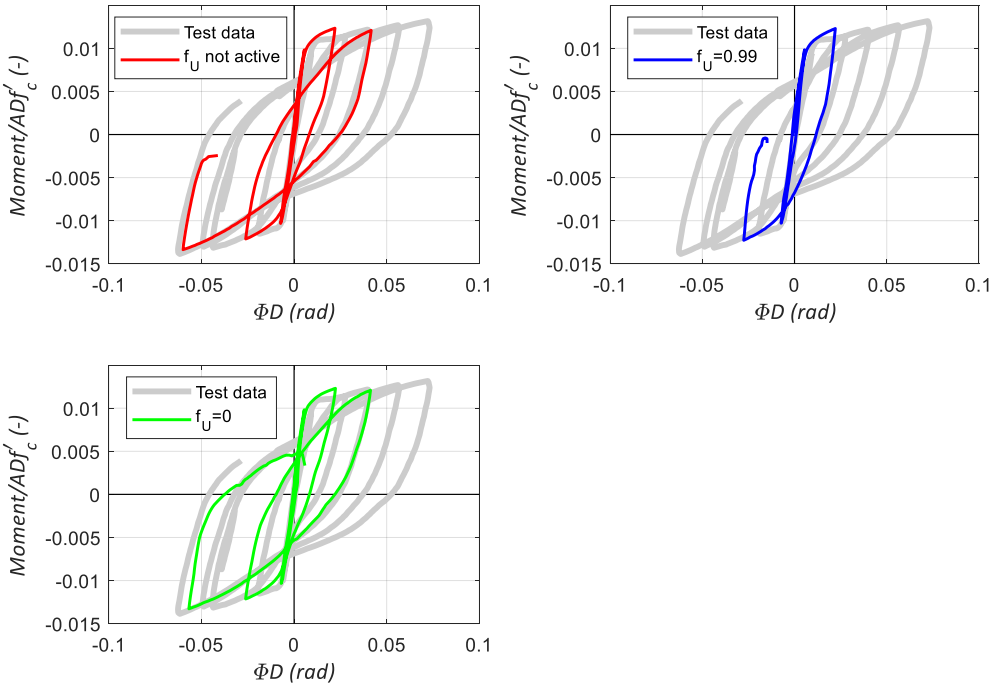

Figure 6–18: Normalized moment-curvature at PH region, for different unloading factor parameters.

Figure 6–18 shows the local response of the plastic hinge region. The models over-estimate the initial stiffness of the first cycle. Model 2 (unloading parallel to initial stiffness) gives higher normalized curvature at the end of the negative loading of μ_Δ=2 (CDR=4.01%), also at the end of this cycle in the unloading process experience convergence issues. At the reloading process of the third ductility displacement cycle, the models are not able to capture the increase in stiffness associated with the closure of the cracks. However, the model that gives a slight change in slope would be Model 3, where the unloading is assumed to go to the origin. This model experience convergence issues at the beginning of the loading process of the fourth ductility displacement cycle.

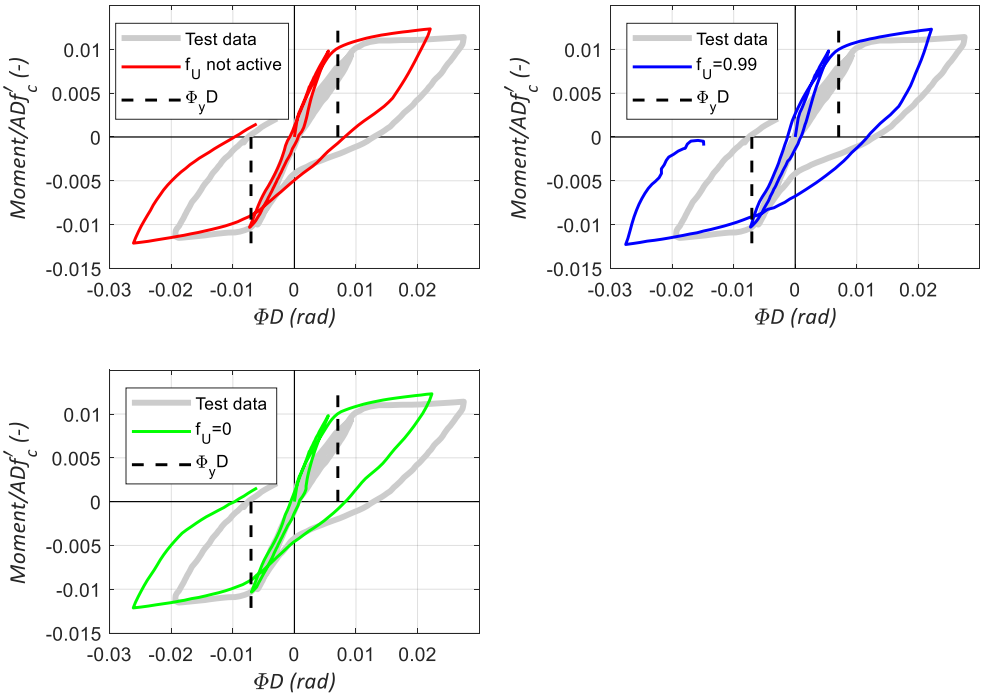

Figure 6–19: First cycles of normalized moment-curvature at PH region, for different unloading parameters.

From Figure 6–19, we can see that activating this parameter increases the ductility in the plastic hinge. Priestley's yield curvature fits well with the model prediction, but the test specimen is more flexible for the positive cycle. Any model does not capture this flexibility.

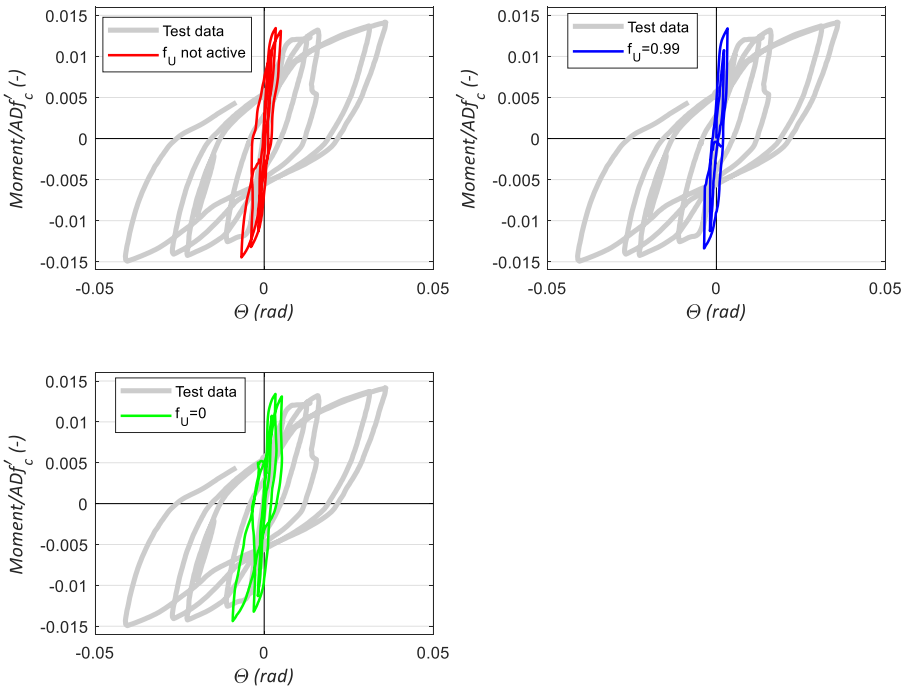

Figure 6–20: Normalized moment-rotation at the shaft-column interface, for different unloading parameters.

Figure 6–20 presents the normalized moment-rotation calculated at the column-shaft interface. For the negative branch of μ_Δ=3 (CDR=6.64%), the model that considers unloading to the origin (f_U=0) gives a higher rotation (24% under the specimen θ). No model can capture well the response at the interface.

Figure 6–21 shows the displacement contributions for each ductility displacement cycles. All the models failed to consider the contribution made by the fixed end rotation. Also, the unloading factor parameter does not have a significant role in the contribution made by the plastic hinge (column 1). The main differences between models are the contributions of the flexural displacement in the shaft and the upper section of the column (column 2). Table 6-10 presents the percentages of the displacement contributions.

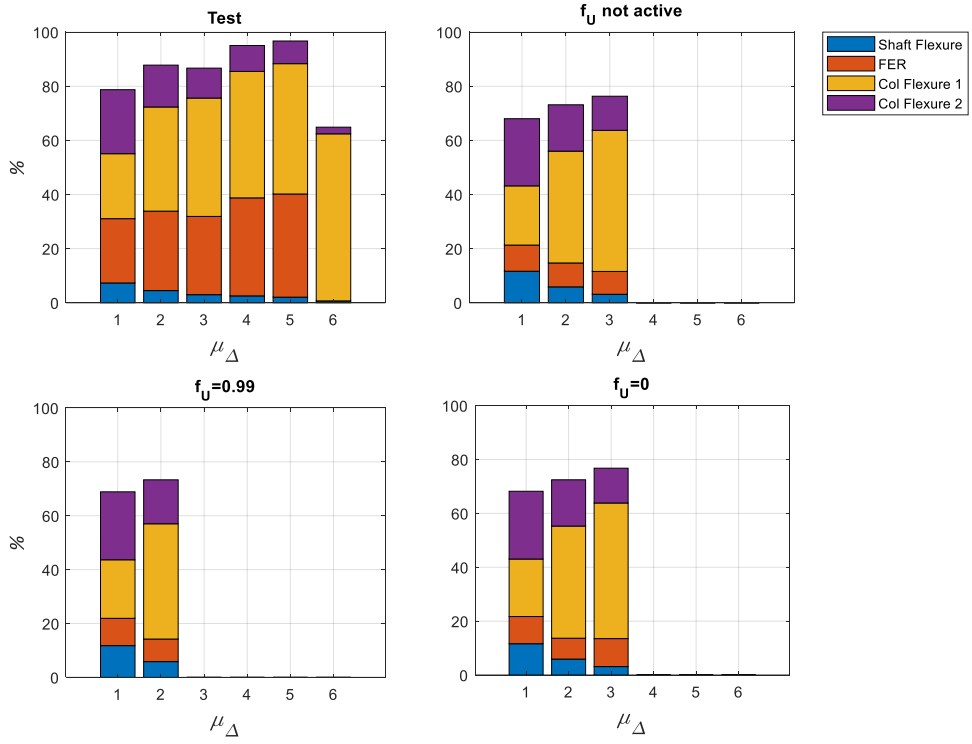

Figure 6–21: Lateral displacements contribution calculated for test specimen and thorough analysis for different unloading factor parameters.

Table 6-10: Displacement contributions in %, for different unloading factor parameters.

	f_U=0.99		M/Test		f_U=0			M/Test		
CDR (%)	1.98	4.01	1.98	4.01	1.98	4.01	6.64	1.98	4.01	6.64
μ_Δ	1	2	1	2	1	2	3	1	2	3
Shaft	11.8	5.9	1.61	1.30	11.6	5.92	3.14	1.59	1.32	1.05
FER	10.1	8.4	0.43	0.29	10.1	7.75	10.4	0.42	0.26	0.36
Col1	21.7	42.8	0.90	1.11	21.3	41.6	50.3	0.89	1.08	1.15
Col2	25.2	16.3	1.07	1.05	25.2	17.2	12.9	1.06	1.11	1.17

From the results, if the model does not present convergence issues by activating the parameter, it seems advisable to employ a value of 0.

6.1.5 Fracture Energy (G_{ft})

For the base model, the formulation given by Vos (1983) was used to compute the fracture energy. G_{ft} is compared with the value obtained by the formulation given by Nakamura & Higai (2001) that relates the compressive fracture energy (G_{fc})with the tensile fracture energy(G_{ft}).

$$G_{fc} = 250 G_{ft} \tag{6.4}$$

Applying this formulation to the values obtained by Lotfizadeh (2019), an average value of 0.55 lb. /in. was found. Table 6-11 presents the values reported of G_{fc} by Lotfizadeh and those of G_{ft} computed from equation 6.4.

Table 6-11: Compressive fracture energy found by Lotfizadeh and the tensile fracture energy found using the formulation by Nakamura & Higai.

Specimen	G_{fc} [lb. /in.]	G_{ft} [lb. /in.]
SPEC01	119	0.476
SPEC02	156	0.624

Table 6-12 shows the models used and the process time. The model that took less time was with fracture energy of 0.44 lb. /in.; also, this model is the one that goes further in the steps.

Table 6-12: Tensile fracture energy models and run time.

Model	Modifications	Run Time [hrs.]	Last Step	Run Time [hrs.] @ 300 steps
M1	G_{ft} = 0.44[lb. /in.]	10.75	427	7.27
M2	G_{ft} = 0.1[lb. /in.]	19.28	388	12.18
M3	G_{ft} = 0.55[lb. /in.]	12.82	333	10.41

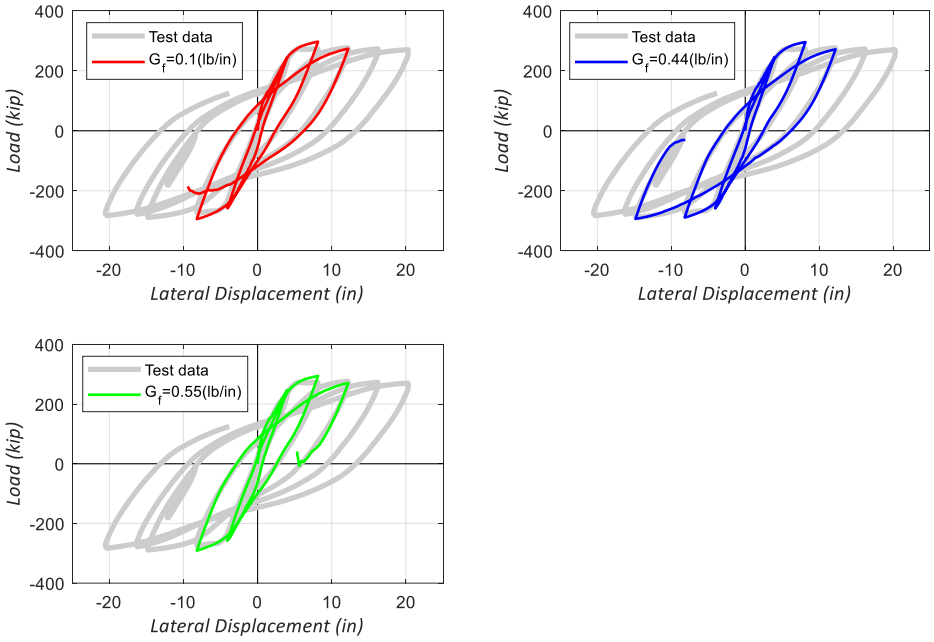

Figure 6–22: Comparison of curve load versus lateral displacement, for different fracture energy parameters.

Figure 6–22 shows the load versus displacement of the test specimen and the models. By changing the fracture (tensile) energy to a higher value or lower of the one recommended by Cervenka Consulting (2018) gives convergence issues at a sooner step. The strength at the end of μ_Δ=2 (CDR=4.01%) of the test is in better agreement with the model with higher G_{ft} (5.4%). However, for Model 1 and Model 2 the values are off by 6% and 7% respectively. For the positive peak of μ_Δ=3 (CDR=6.64%), the predicted strength is higher by around 3% for the three models.

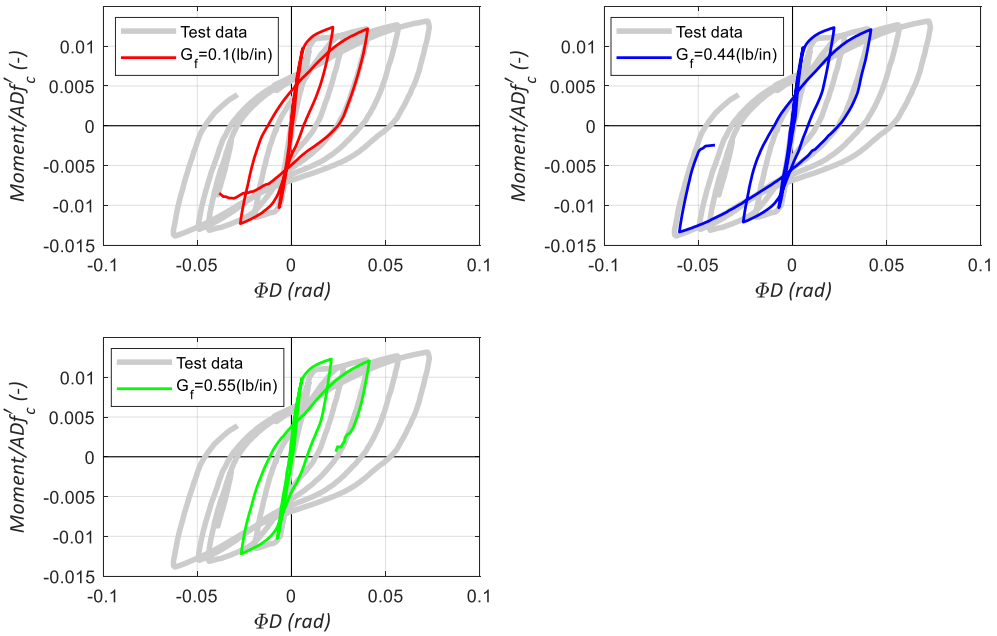

Figure 6–23: Comparison of normalized moment-curvature at PH region, for different fracture energy parameters.

Figure 6–23 shows the normalized moment-curvature graphs of the plastic hinge region. The curvature for all the models is under-predicted for the positive second displacement ductility and over-predicted for the negative part of this cycle. For μ_{Δ}=3 (CDR=6.64%), in the positive loading, the three models gave a good match in curvature and flexural capacity. But in the negative loading, the models Model 2 and Model 3 cannot go that far into the analysis, and for Model 1 the curvature prediction is overestimated by 41%.

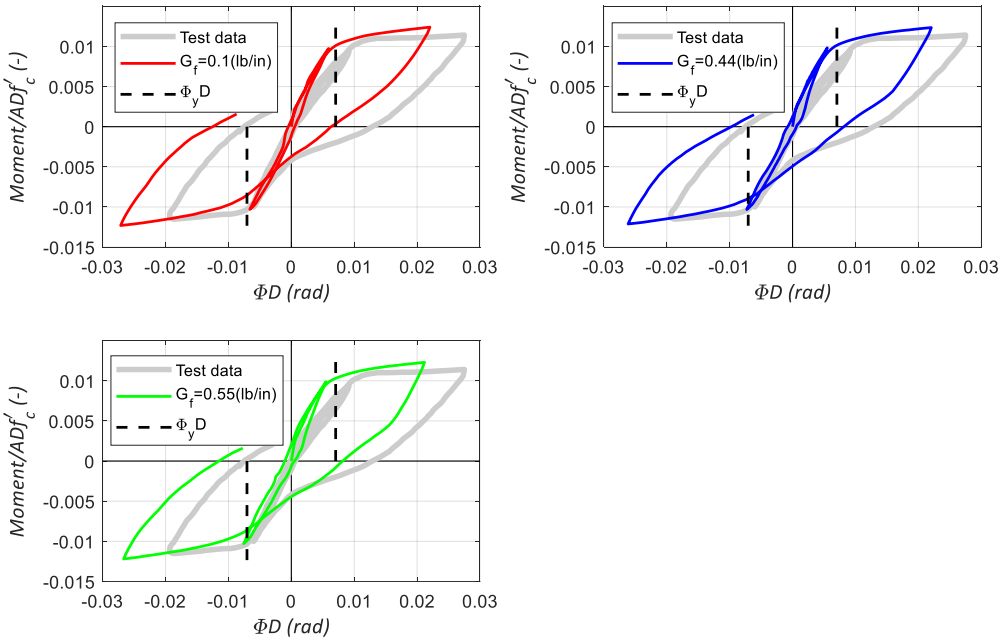

Figure 6–24: First cycles of normalized moment-curvature at PH region, for different fracture energy parameters.

Figure 6–24 presents the first two displacement ductility cycles with the yield curvature predicted by Priestley. The test specimen is more flexible than the prediction given by the analytical model as well as by Priestley's formulation for the positive loading. For the negative loading, the models and test provide a better match with Priestley's formulation, where the model that gives the better prediction is the one with lower tensile fracture energy.

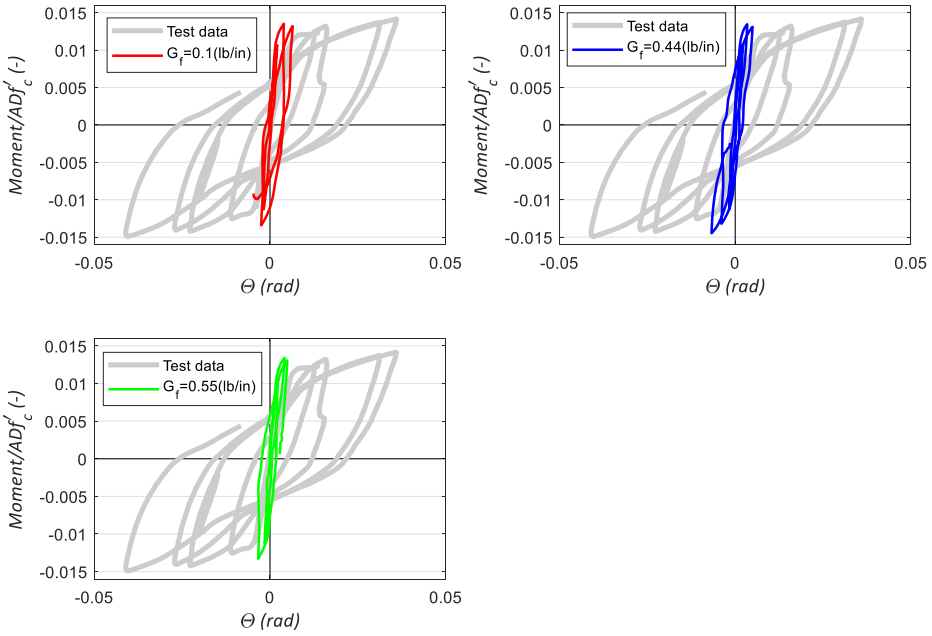

Figure 6–25: Normalized moment-rotation at the shaft-column interface, for different fracture energy parameters.

Figure 6–25 displays the normalized moment-rotation at the shaft-column interface. Changing the tensile fracture energy (G_{ft}) does not affect much this behavior at this displacement level.

Figure 6–26 gives the displacement contribution (in percentage) by region of the structure. Modifying G_{ft} does not have an impact on the displacement contribution of the FER, which is the displacement contribution that it is by far off on the model predictions. The displacement contribution does not varied much by changing the parameter in the range given. Table 6-13 shows the values presented in Figure 6–26.

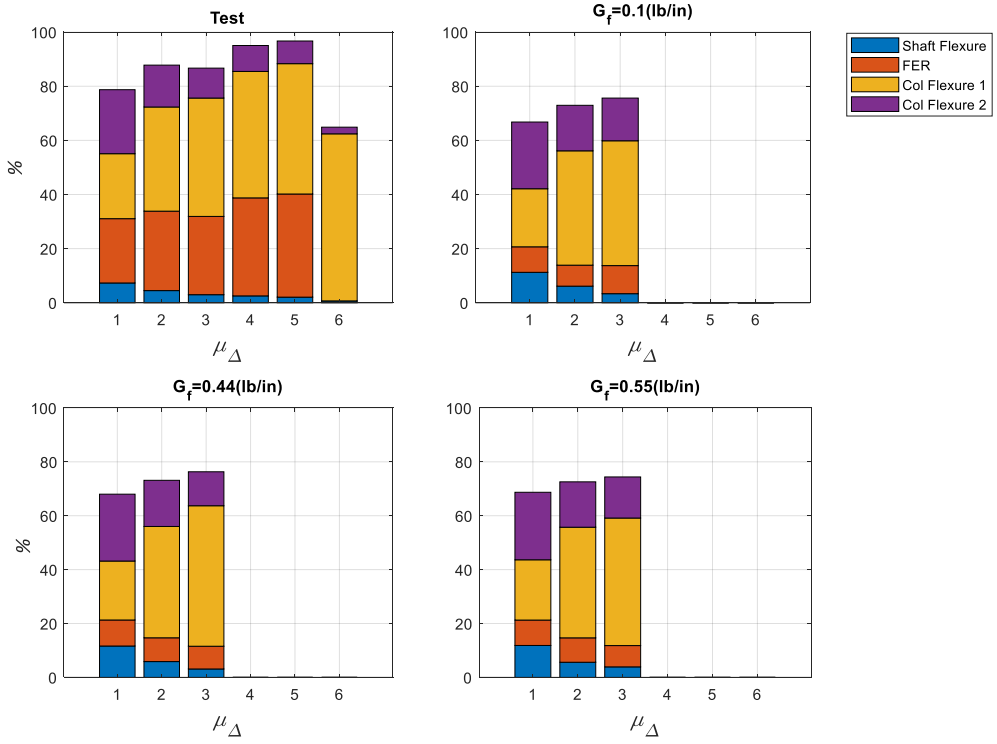

Figure 6–26: Comparison of displacements contributions, for different fracture energy parameters.

Table 6-13: Displacement contributions in %, for different fracture energy parameters

	G_{ft} = 0.1[lb/in.]			M/Test			G_{ft} = 0.55[lb/in.]			M/Test		
CDR (%)	1.98	4.01	6.64	1.98	4.01	6.64	1.98	4.01	6.64	1.98	4.01	6.64
μ_Δ	1	2	3	1	2	3	1	2	3	1	2	3
Shaft	11.2	6.14	3.35	1.54	1.37	1.13	11.9	5.63	3.9	1.62	1.25	1.31
FER	9.42	7.75	10.4	0.4	0.26	0.36	9.43	9.05	7.9	0.4	0.31	0.27
Col1	21.5	42.2	46.1	0.89	1.1	1.05	22.4	41.1	47	0.93	1.07	1.08
Col2	24.7	16.8	15.8	1.04	1.09	1.43	25.1	16.8	15	1.06	1.09	1.38

6.1.6 Fixed-crack Model

The base model used a rotated cracked model since a fixed-crack model gave convergence issues. In the following, the convergence problems are evident by showing the response for three different values of this parameter. Table 6-13 gives the variation in the parameters used, and the time that the analysis took to run. From the table models without the fully rotated crack model crushed at μ_{Δ}=1 (CDR=1.98%).

Table 6-14: Fixed-crack models and run time.

Model	Modifications	Run Time [hrs.]	Last Step	Run Time [hrs.] @ 300 steps
M1	Fixed-crack set to 0	10.75	427	7.27
M2	Fixed-crack set to 1	13.07	120	-
M3	Fixed-crack set to 0.5	14.65	130	-

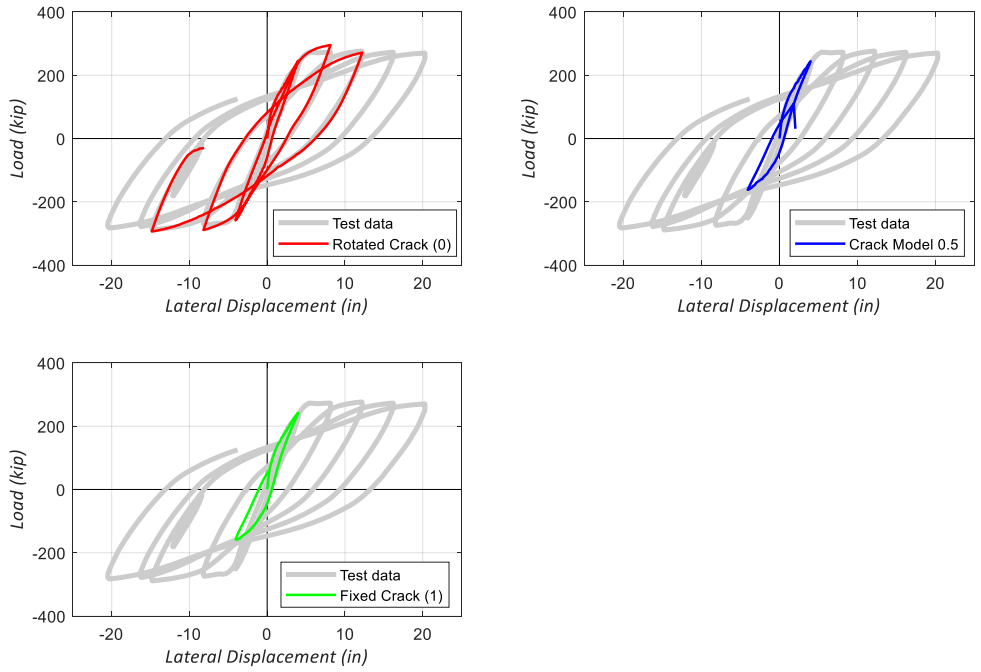

Figure 6–27: Comparison of curve load versus lateral displacement, for different crack models.

Figure 6–27 shows the comparison of the overall behavior of the test and the analytical models. From this, it is clear that a fixed-crack model was unsuccessful for this work.

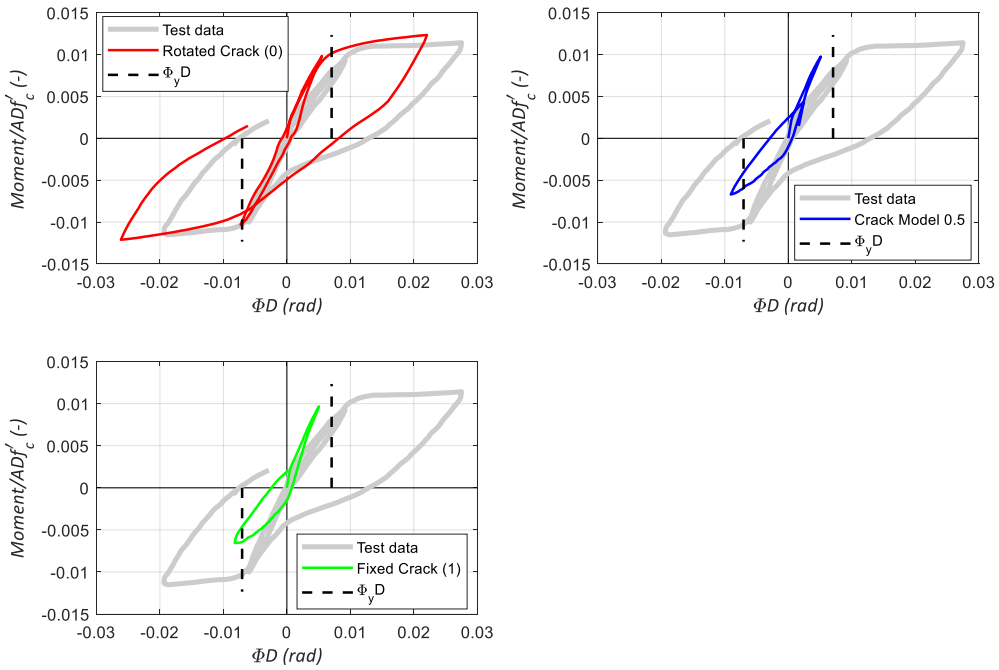

Figure 6–28: First cycles of normalized moment-curvature at PH region, for different crack models.

Since the models added to the base model only could run within the first displacement ductility cycle, just the comparison of the moment-curvature for the first two cycles is given in Figure 6–28. From this, it is clear that a poor prediction of the plastic hinge region is the result of considering crack models that are not the rotated one.

Figure 6–29 presents the normalized moment-rotation for the shaft-column interface. From this, the models are not capable of predicting the rotation at the interface.

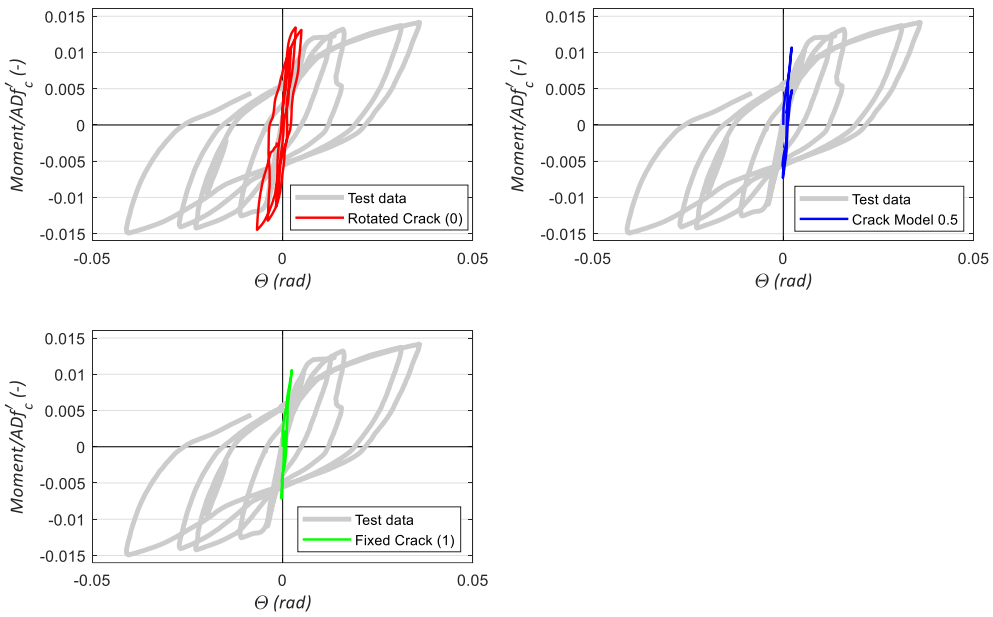

Figure 6–29: Normalized moment-rotation at the shaft-column interface, for different crack models.

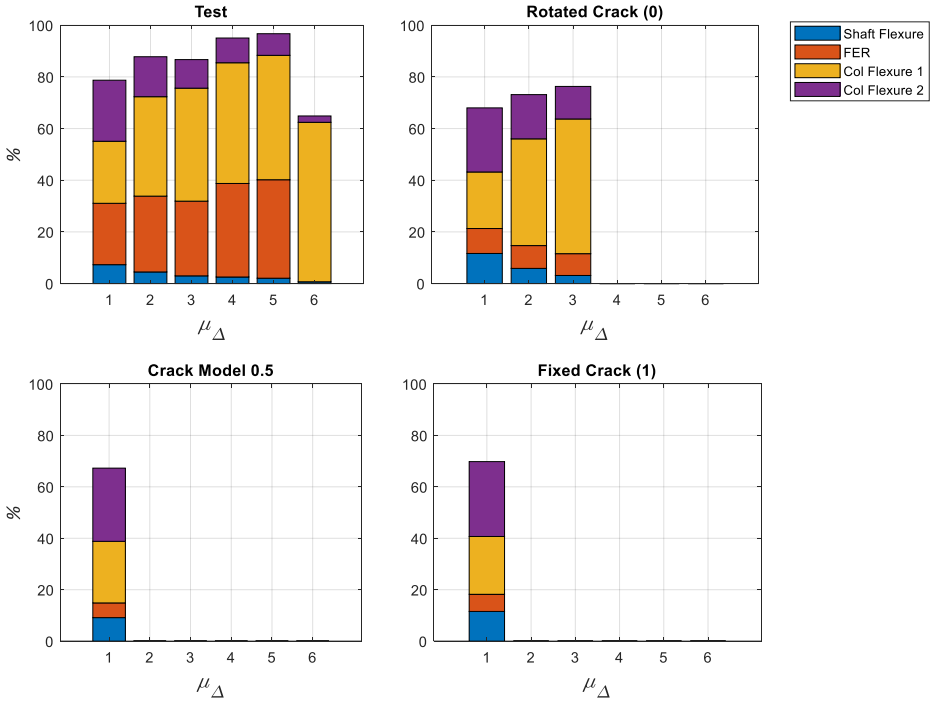

Figure 6–30: Lateral displacements contribution calculated for test specimen and thorough analysis for different crack models.

Table 6-15: Displacement contributions in %, for different crack models.

	Value=1	M/Test	Value=0.5	M/Test
CDR (%)	1.98	1.98	1.98	1.98
μ_Δ	1	1	1	1
Shaft	11.6	1.58	9.15	1.25
FER	6.66	0.28	5.72	0.24
Col1	22.5	0.94	23.9	1
Col2	29.1	1.23	28.5	1.2

Figure 6–30 shows the percentage of the displacement contributions given in numeric values in Table 6-15. Modifying this parameter does not affect the displacement contribution of the fixed end rotations, where the predictions are worst.

The author suggests the use of a rotated crack model instead of the fixed-crack model to avoid convergence issues with cyclic analysis.

6.1.7 Critical compression displacement (w_d)

Three values, additional to the one used in the base model, were employed to review the effect of the critical compression displacement in the model predictions. Table 6-16 presents the values used and the process time for these models. From it, the model that went further into the displacement cycles was the base model. The base model had a higher value of w_d, which is ten times the value recommended by Cervenka Consulting (2018).

Table 6-16: Critical compression displacement models and run time

Model	Modifications	Run Time [hrs.]	Last Step	Run Time [hrs.] @ 300 steps
M1	w_d =-0.197[in.]	10.75	427	7.27
M2	w_d =-0.0197[in.], recommended per Cervenka Consulting (2018)	10.3	221	-
M3	w_d =-0.0984[in.], found by Nakamura & Higai (2001).	15.96	390	11.5
M4	w_d =-0.0295[in.], value from Round Robin test. (Van Mier, 1984)	12.77	230	-

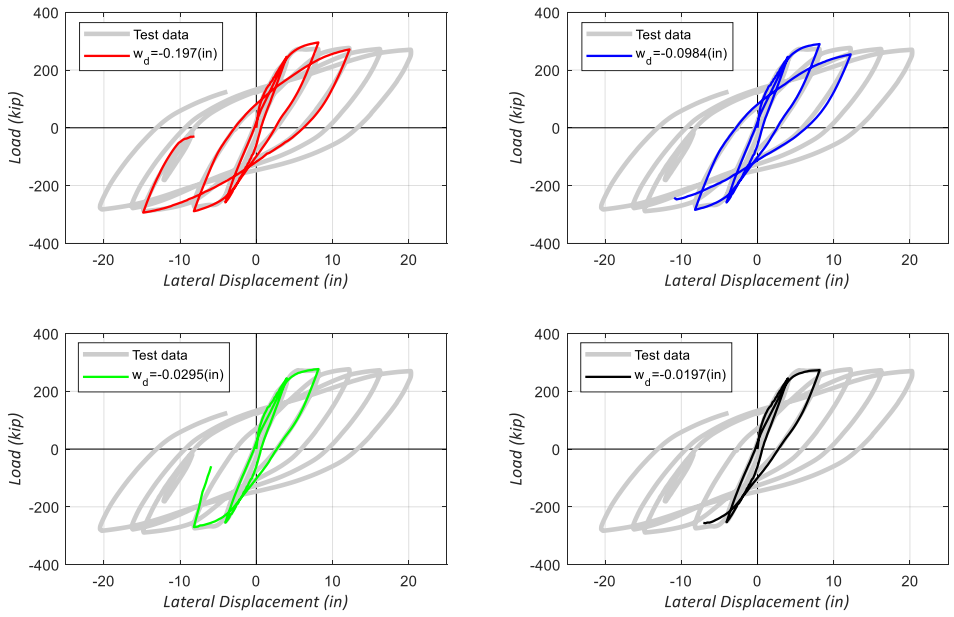

Figure 6–31: Comparison of curve load versus lateral displacement, for different critical compression displacement values.

Figure 6–31 shows the overall behavior of the test with the predictions of the models. From this the model that represents better the curve if the one with w_d= -0.0295 in. For this model the strength and curvature matches within 2% of error. Figure 6–32 displays the close up of this mode for the first two cycles.

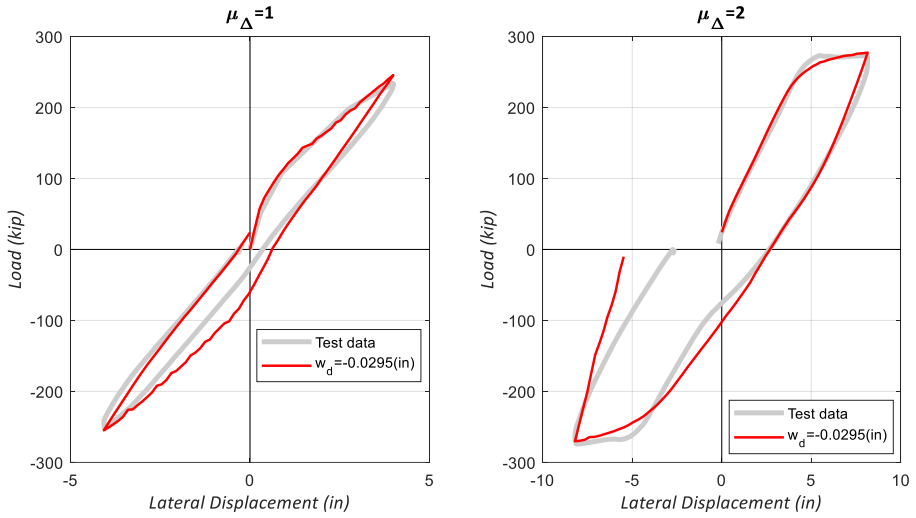

Figure 6–32: First two cycles of curve load versus displacement, for w_d=-0.0295in.

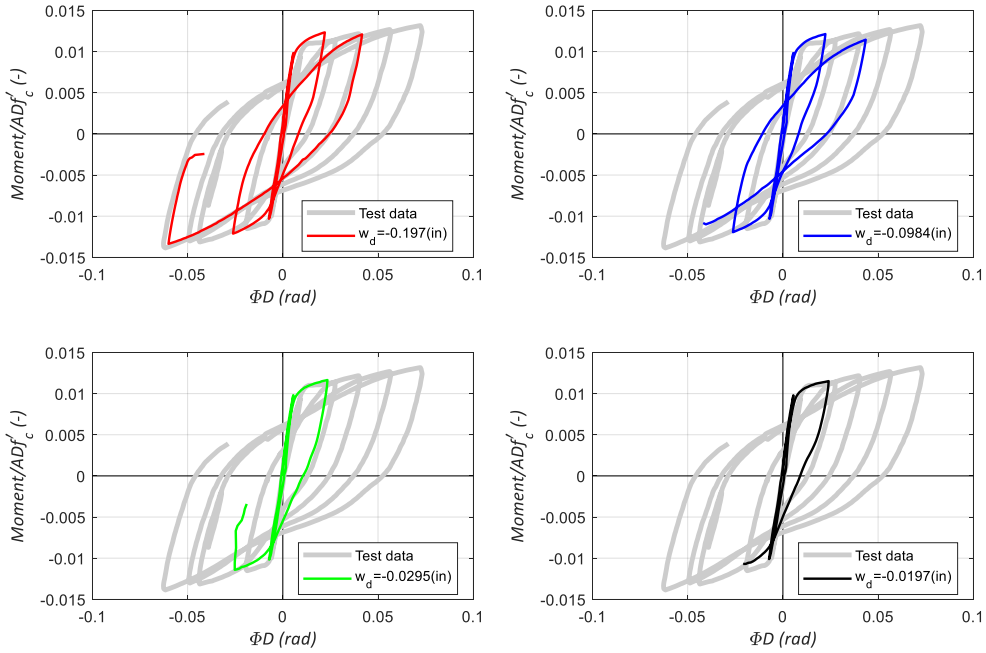

Figure 6–33: Normalized moment-curvature at PH, for different critical compression displacement values.

Figure 6–33 presents the normalized moment-curvature for the plastic hinge region. All the models over-estimate the curvature at the end of the negative loading of μ_Δ=2 (CDR=4.01%). The lesser the value of w_d was taken the smaller was the over-estimation. Also, the lower the value of w_d the less the flexural capacity at peak displacement.

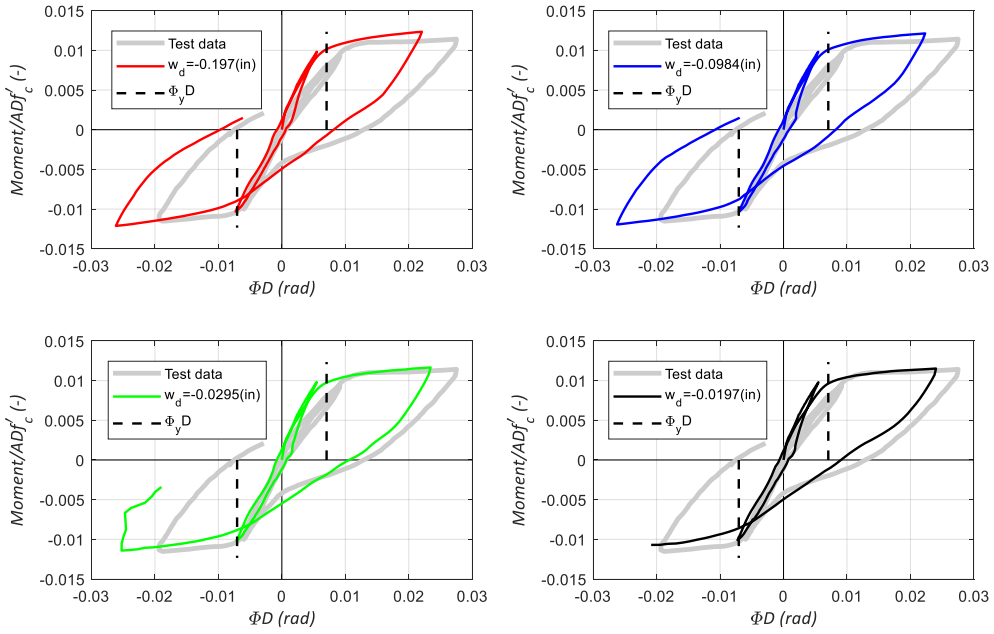

Figure 6–34: First cycles of normalized moment-curvature at PH region, for different critical compression displacement values.

Figure 6–34 gives the first two cycles of the normalized moment-curvature with the yield curvature predicted by Priestley (2003). The test specimen in the positive loading direction is more flexible than the predictions by the models and by Priestley's formulation. As already mentioned, the strength in the projection is lower by reducing the values of w_d.

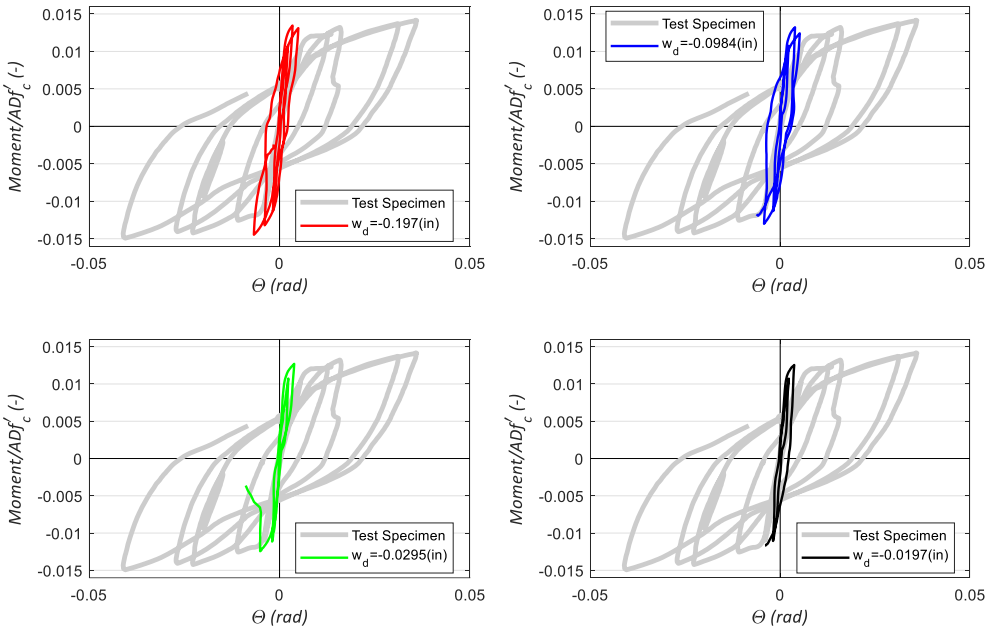

Figure 6–35: Normalized moment-rotation at shaft-column interface, for different critical compression displacement values.

Shown in Figure 6–35 is the normalized moment-rotation at the shaft-column interface. None of the models can capture the displacement capacity of this region.

Figure 6–36 gives in percentages the displacement contributions. Changing the parameter does not change much of the overall response. The models over predict the shaft flexural displacement contribution and under-predict the capacity of the shaft-column interface. The graph in Figure 6–36 is based on the values given in Table 6-17 and Table 6-18.

In light of the results, the parameter does not change much the predictions. However, the author recommends the use of the value -0.0295 in. due to the fitting of the overall behavior for the first two cycles.

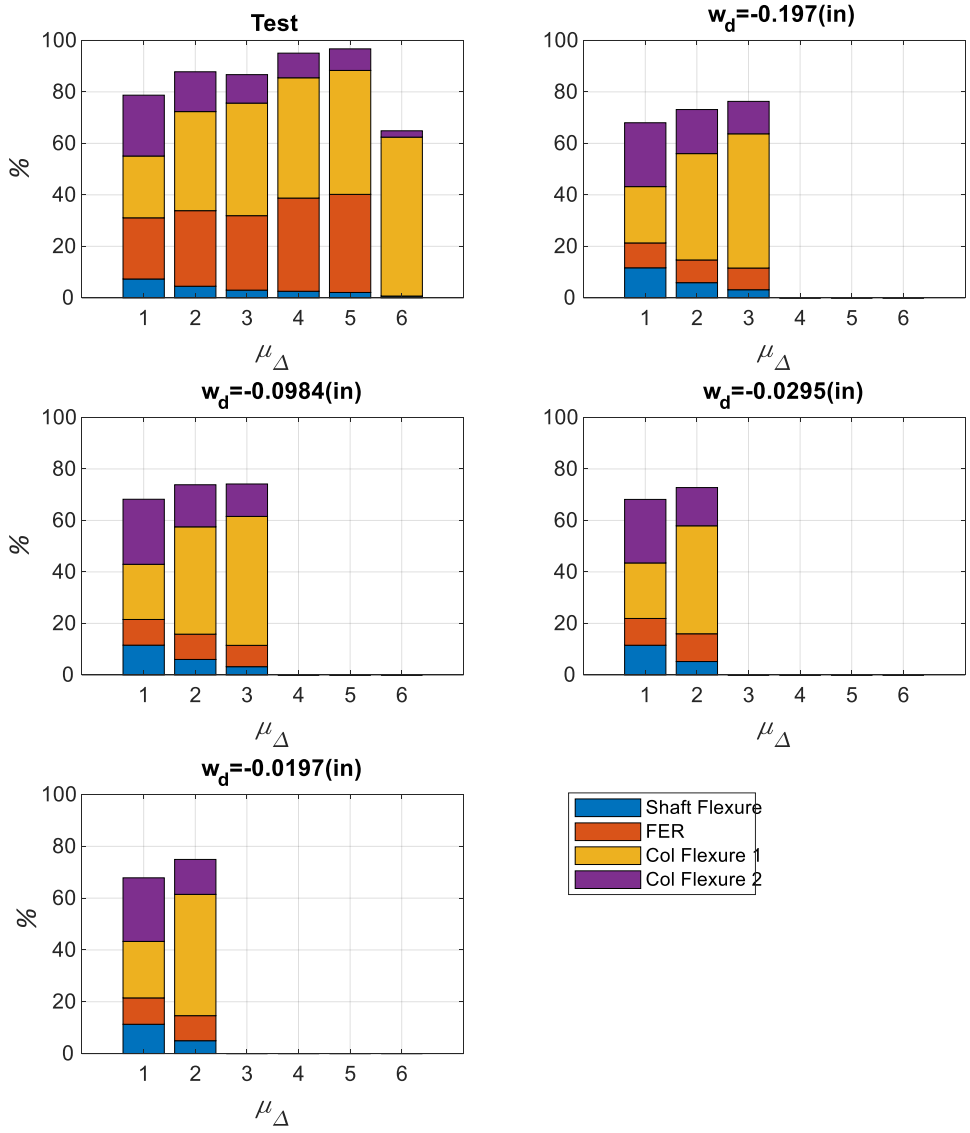

Figure 6–36: Lateral displacements contribution calculated for test specimen and thorough analysis for different critical compression displacement values.

Table 6-17: Displacement contributions in %, for different critical compression displacement values.

	w_d=-0.0984[in.]			M/Test		
CDR (%)	1.98	4.01	6.64	1.98	4.01	6.64
μ_Δ	1	2	3	1	2	3
Shaft	11.5	5.99	3.17	1.58	1.33	1.07
FER	9.98	9.82	8.29	0.42	0.33	0.29
Col1	21.4	41.7	50.1	0.89	1.08	1.15
Col2	25.3	16.3	12.6	1.07	1.06	1.14

Table 6-18: Displacement contributions in %, for different critical compression displacement values.

	w_d=-0.0295[in.]		M/Test		w_d=-0.0197[in.]		M/Test	
CDR (%)	1.98	4.01	1.98	4.01	1.98	4.01	1.98	4.01
μ_Δ	1	2	1	2	1	2	1	2
Shaft	11.5	5.2	1.57	1.15	11.3	5.0	1.55	1.1
FER	10.4	10.8	0.44	0.37	10.2	9.7	0.43	0.33
Col1	21.6	41.9	0.90	1.09	21.8	46.8	0.91	1.22
Col2	24.7	14.9	1.04	0.96	24.6	13.5	1.04	0.87

6.1.8 Fc Reduction

As mentioned earlier, Fc reduction is a parameter that reduces the compressive strength due to imposed tensile strain following the Modified Compression Field Theory (Collins and Mitchell, 1991). The value of the compressive strength cannot drop further than f'_c times r_c. Table 6-19 gives the different reduction values used and the time that the analysis took. From the table, the fastest model was the base model.

Table 6-19: Fc reduction models and run times.

Model	Modifications	Run Time [hrs.]	Last Step	Run Time [hrs.] @ 300 steps
M1	Fc=1	10.75	427	7.27
M2	Fc=0.6	18.25	407	13.85
M3	Fc=0.2	22.22	374	14.41

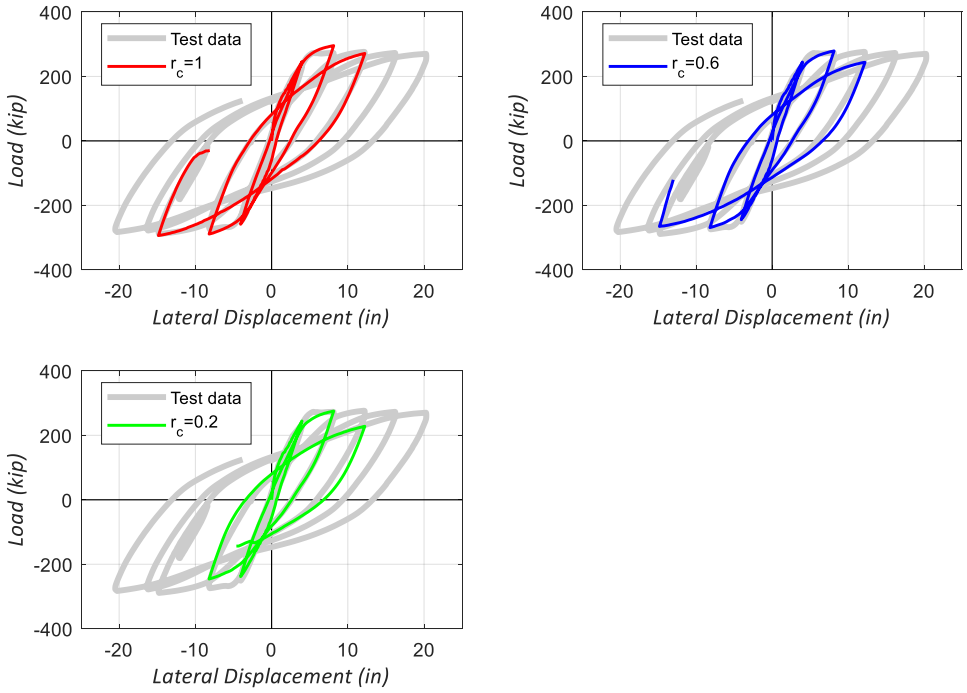

Figure 6–37: Comparison of curve load versus lateral displacement, for different r_c values.

Figure 6–37 shows the effect that the reduction on the compressive strength has on the prediction of the cyclic response. As lower the value, the loss of strength at the subsequent cycles increases. Leading into a better match at the peak strength of the second cycle, but it diverges at the peak of the third cycle. Considering a value of 0.2 for r_c, gives convergence issues after the positive cycle of μ_Δ=3 (CDR=6.64%).

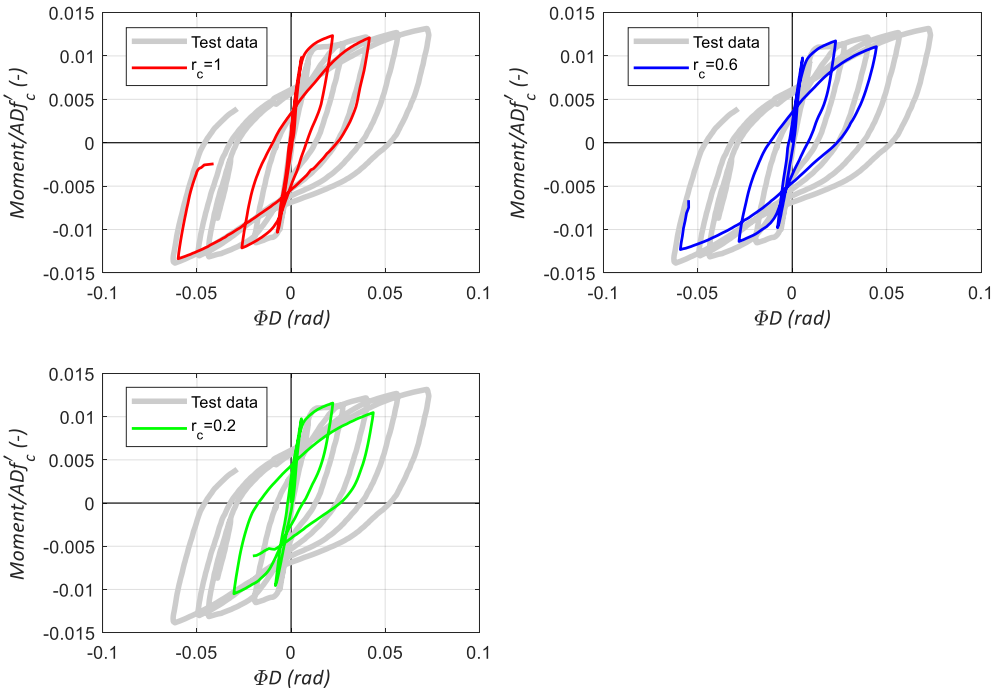

Figure 6–38: Comparison of normalized moment-curvature at PH, for different r_c values.

Figure 6–38 shows the normalized moment curvature of the plastic hinge region. As it was expected changing the value of the reduction factor affects the flexural capacity of the plastic hinge at higher displacement ductility cycles, but the curvature at the peak displacement does not change dramatically.

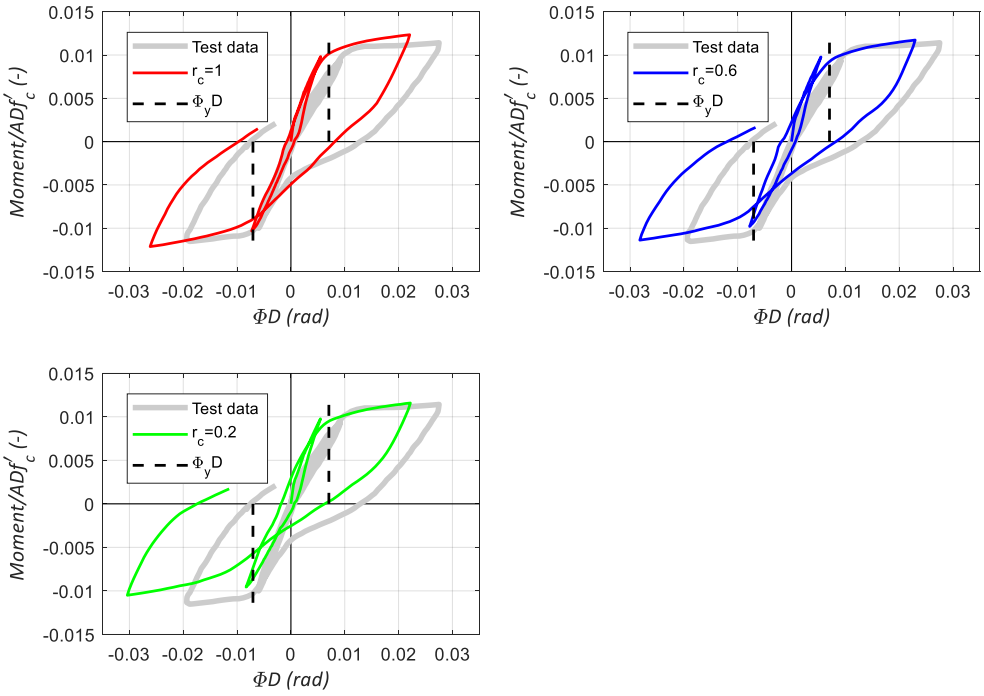

Figure 6–39: First cycles of normalized moment-curvature at PH, for different r_c values.

Figure 6–39 shows the normalized moment-curvature for the first two displacement ductility cycles, with Priestley's formulation for the yield curvature. The model that has a better agreement with Priestley's yield curvature is the one that does not consider the reduction of the compressive strength. However, using a value of less than one gives a better agreement on the flexural capacity at the end of the second cycle. The models do not predict well the curvature of the specimen.

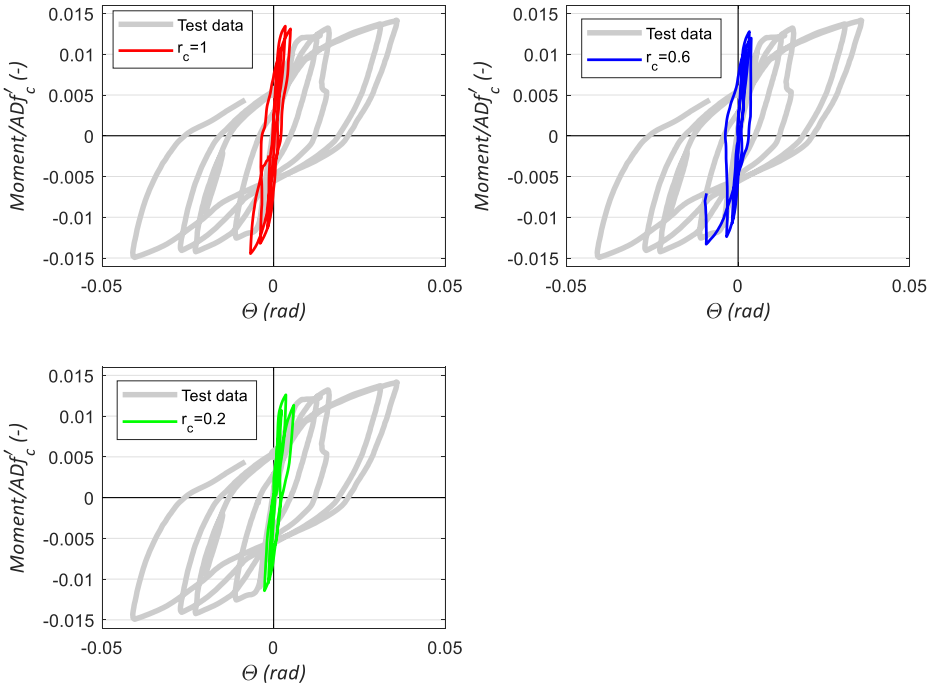

Figure 6–40: Normalized moment-rotation at the shaft-column interface, for different r_c values.

The comparison presented in Figure 6–40 shows that any model can predict the displacement capacity at the shaft-column interface. All the models underestimate the rotation capacity; however, the flexural capacity at the peaks is well captured.

Figure 6–41 compares the distributions of the displacements through the specimen. And Table 6-20 gives the values in percentages of the displacement contributions shown in the figure. The parameter does not have a significant impact on the distribution. Also, this parameter does not have a great effect on the contribution of the displacement of the fixed end rotation.

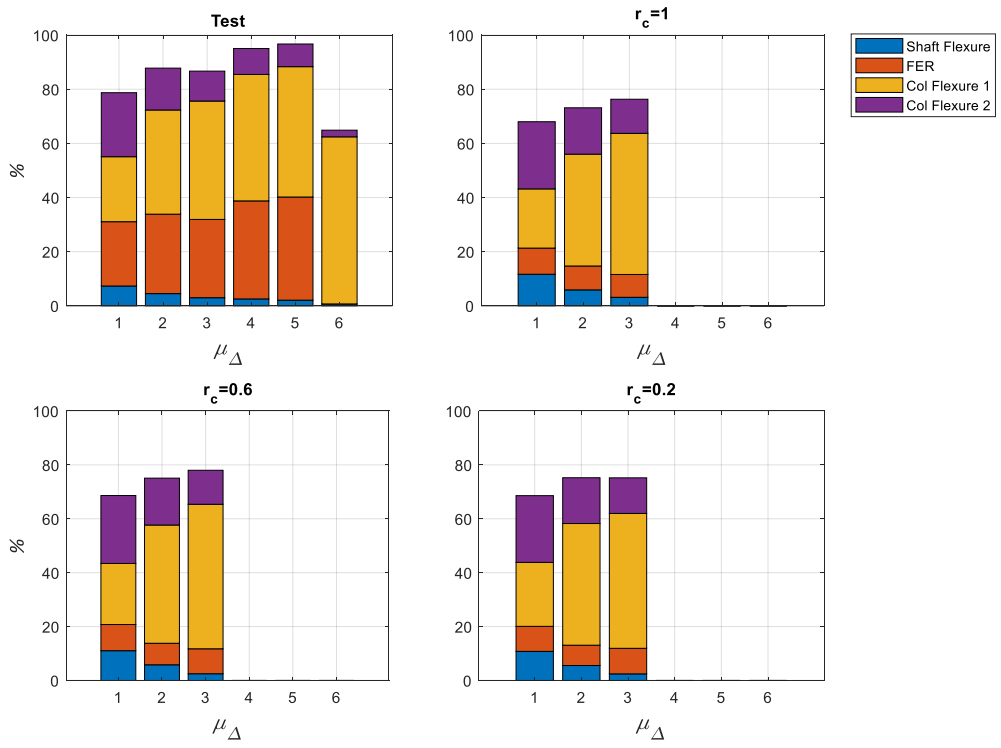

Figure 6–41: Lateral displacements contribution calculated for test specimen and thorough analysis for different r_c values.

Table 6-20: Displacement contributions in %, for different r_c values.

	r_c = 0.6			M/Test			r_c = 0.2			M/Test		
CDR (%)	1.98	4.01	6.64	1.98	4.01	6.64	1.98	4.01	6.64	1.98	4.01	6.64
μ_Δ	1	2	3	1	2	3	1	2	3	1	2	3
Shaft	11	5.82	2.5	1.51	1.3	0.84	10.8	5.55	2.5	1.48	1.24	0.82
FER	9.72	7.99	9.26	0.41	0.27	0.32	9.29	7.54	9.5	0.39	0.26	0.33
Col1	22.7	43.9	53.6	0.94	1.14	1.23	23.7	45.2	50	0.99	1.17	1.14
Col2	25.2	17.4	12.6	1.07	1.12	1.14	24.8	17	13	1.05	1.1	1.19

In conclusion, this parameter should not be taken less than 0.6 to improve the fitting of the strength reduction over cycles. It is important to notice that using a value of 0.6 might come with a decrease in the incursion in the displacement cycles due to convergence problems.

6.1.9 Direction of plastic flow (β)

The plastic flow parameter controls the direction of return of the plastic flow. It is related to the expansion or contraction of the material. The program supports values between -5 and 5. However, values greater than 0.5 gave convergence issues at early stages of the analysis, so they were not considered.

From Table 6-21 the fastest model was the base model, with β set as zero. Then considering β as 0.1 or -0.1 had the same rate of the process, but if the material accepted contraction, the program could go further in the steps analyzed.

Table 6-21: Direction of plastic flow models and run times.

Model	Modifications	Run Time [hrs.]	Last Step	Run Time [hrs.] @ 300 steps
M1	β =0	10.75	427	7.27
M2	β =0.5	9.27	200	-
M3	β =0.1	12.25	320	11.71
M4	β =-0.1	18.67	463	11

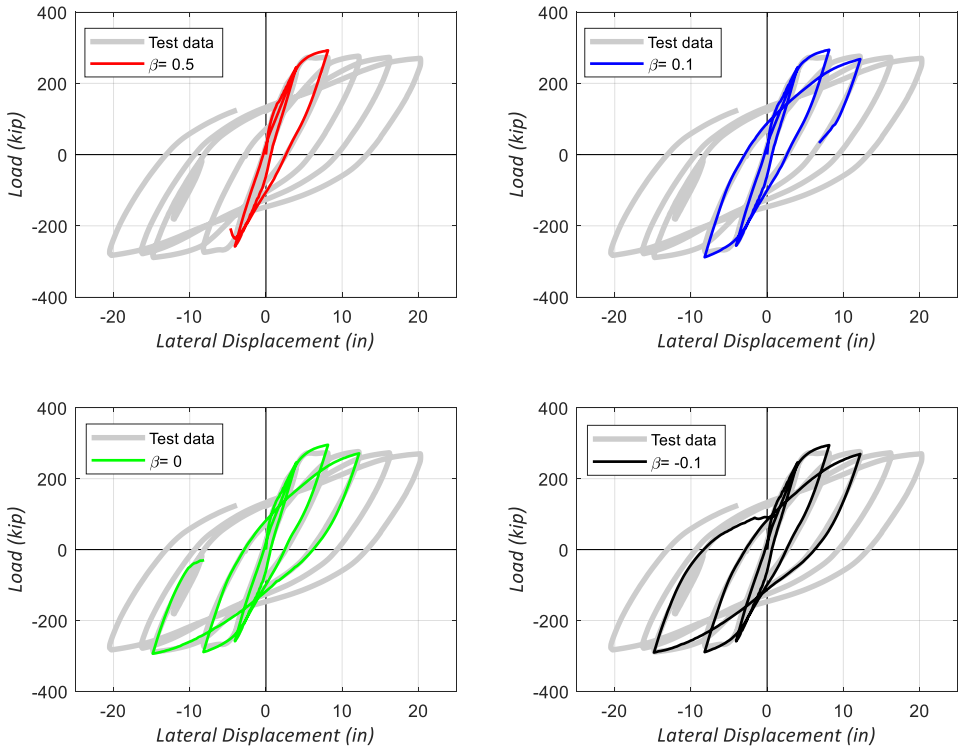

Figure 6–42: Comparison of curve load versus lateral displacement, for different β values.

From the overall predicted behavior shown in Figure 6–42, it is clear that changing the capacity of the material to contract or expand does not changes the response of the model at this displacement levels.

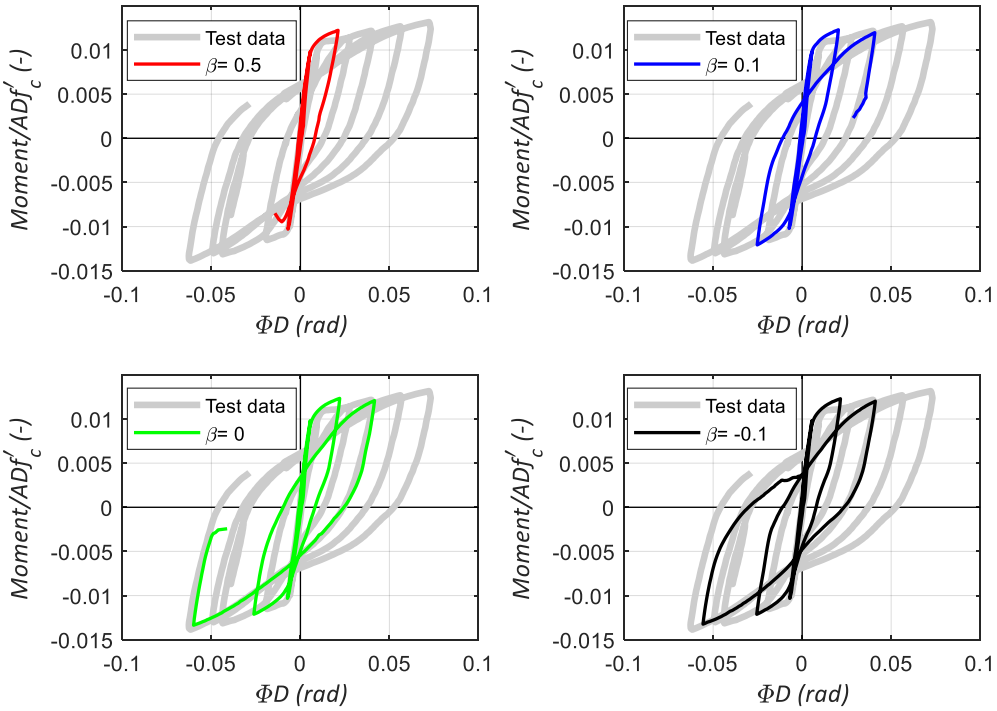

Figure 6–43: Comparison of normalized moment-curvature at PH region, for different β values.

In Figure 6–43 the normalized moment-curvature of the plastic hinge region is presented. Differences between the model that considers contraction and the model that considers β as zero are clear starting at μ_Δ=3 (CDR=6.64%). For this cycle, the model with contraction had less curvature capacity at the negative branch, with an error of 28% instead of 38%. Also, in this cycle, the model that can contract has less energy dissipation than the one with β equals zero.

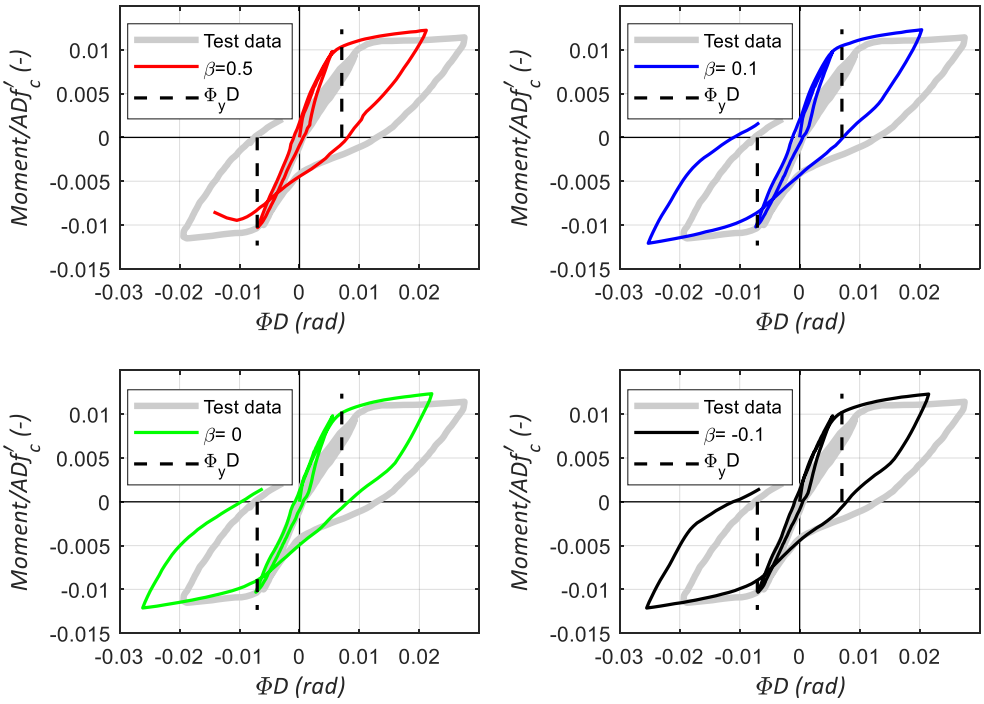

Figure 6–44: First cycles of normalized moment-curvature at PH region, for different β values.

Figure 6–44 gives the first two cycles of the normalized moment-curvature at the plastic hinge with the predicted yield curvature from Priestley (2003). The variation between the models for this displacement level is minor. The model predictions for the yield curvature match the one given by Priestley. The test specimen was more flexible for the positive cycle than for the negative.

In Figure 6–45 the normalized moment-rotation at the shaft-column interface is shown. The model that allows contraction of the material at μ_Δ=3 (CDR=6.64%) gives a higher rotation capacity than the other models. However, no models can capture the behavior observed in the test specimen.

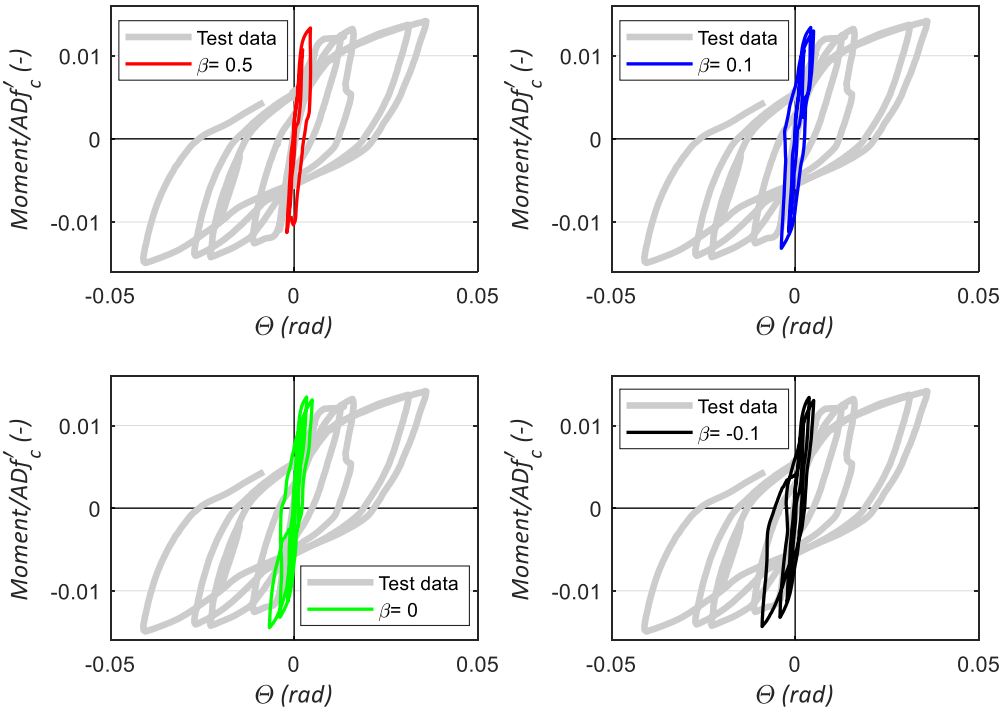

Figure 6–45: Normalized moment-rotation at the shaft-column interface, for different β values.

Figure 6–46 presents the distribution of the lateral displacement capacity within the element height. The values are shown in Table 6-22 and Table 6-23, given in percentages of the total displacement at the cycle. From this, the model that offers a better match with the fixed end rotation displacement contribution is the model that considers contraction of the concrete. Due to this improvement, the author recommends the use of β= -0.1.

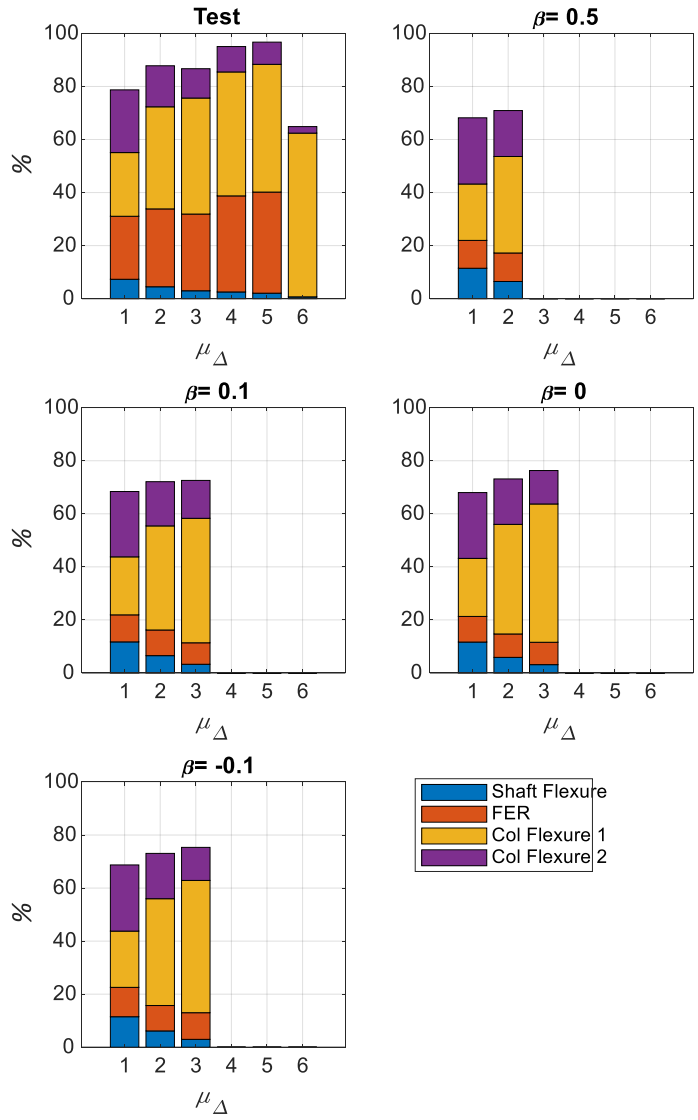

Figure 6–46: Lateral displacements contribution calculated for test specimen and thorough analysis for different β values.

Table 6-22: Displacement contributions in %, for different β values.

	β = 0.5		M/Test		β = 0.1			M/Test		
CDR (%)	1.98	4.01	1.98	4.01	1.98	4.01	6.64	1.98	4.01	6.64
μ_Δ	1	2	1	2	1	2	3	1	2	3
Shaft	11.5	6.48	1.57	1.44	11.71	6.52	3.27	1.60	1.45	1.10
FER	10.5	10.8	0.44	0.37	10.19	9.67	8.10	0.43	0.33	0.28
Col1	21.3	36.4	0.89	0.95	21.87	39.24	46.93	0.91	1.02	1.07
Col2	25	17.3	1.06	1.12	24.63	16.67	14.29	1.04	1.08	1.29

Table 6-23: Displacement contributions in %, for different β values.

	β = -0.1			M/Test		
CDR (%)	1.98	4.01	6.64	1.98	4.01	6.64
μ_Δ	1	2	3	1	2	3
Shaft	11.5	6.15	2.97	1.57	1.37	1
FER	11.1	9.58	10	0.47	0.33	0.35
Col1	21.2	40.3	49.9	0.88	1.05	1.14
Col2	24.9	17.1	12.5	1.06	1.1	1.13

6.2 STEEL PARAMETERS

6.2.1 Menegotto-Pinto

The parameters of the Menegotto-Pinto (M-P) formulation implemented in the program correspond to R, c_1 and c_2. Table 6-24 shows the values used for analysis and the time that the program took to process. The model that ran further into the displacement ductility cycles was Model 4. The model that had the shortest incursion in the displacement ductility cycles was Model 3. The fastest model was the based model.

Table 6-24: Menegotto-Pinto models and run time.

Model	Modifications	Run Time [hrs.]	Last Step	Run Time [hrs.] @ 300 steps
M1	R=2 c_1=5000 c_2=20	10.75	427	7.27
M2	R=4 c_1=500 c_2=50	18.13	450	10.5
M3	R=4 c_1=5000 c_2=20	18.58	360	10.43
M4	R=2 c_1=500 c_2=20	18.82	470	10.65
M5	R=2 c_1=5000 c_2=50	14.32	410	10.86

Figure 6–47 shows the overall behavior of the analytical models and the test specimen. From the graphs, if c_1 is reduced the strength at the peak displacement increases by 3% for the second cycle and 7% for the third cycle. By increasing c_2, the strength increases at the peak

displacement by 1% for the second cycle and less than 1% for the third cycle. Increasing R to the double also gave a higher strength at the peak displacements, in 4% and 6% for the second and third cycles.

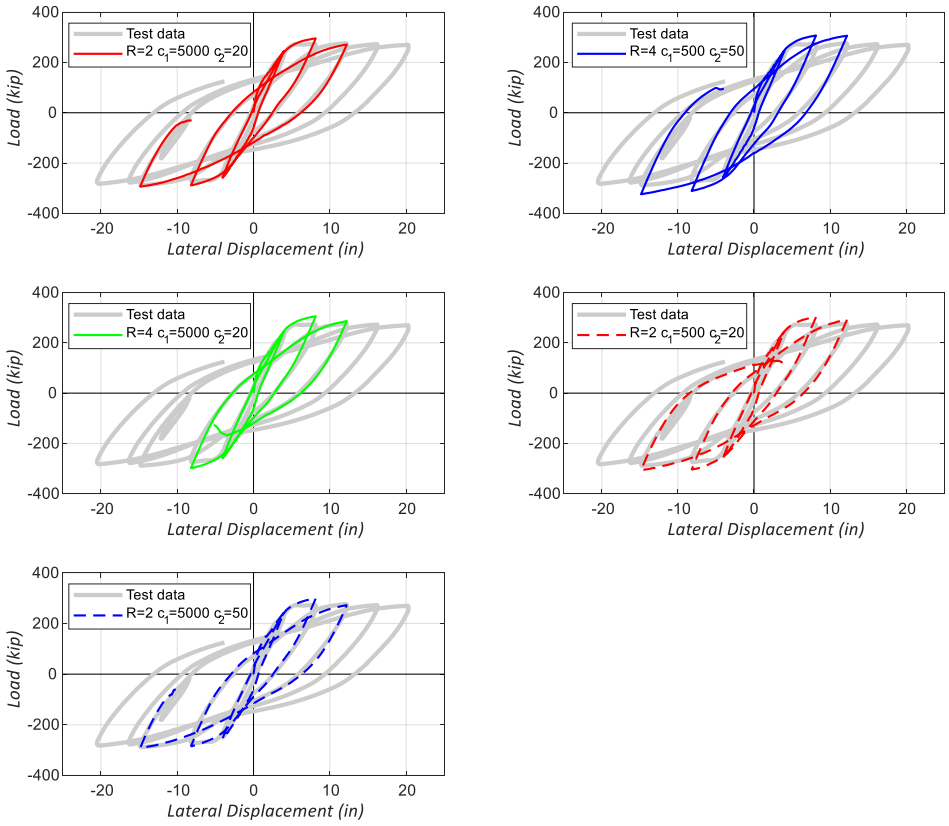

Figure 6–47: Comparison of curve load versus lateral displacement, for different M-P Parameters.

Figure 6–48 presents the normalized moment-curvature for the plastic hinge region. The initial positive stiffness of the models is higher than the specimen; this also holds for the second displacement ductility in the second quadrant. However, for μ_{Δ}=3 (CDR=6.64%), in the same quadrant, the prediction from the models' suites well for all the models except Model 2, which gives a higher flexural capacity and a lower ductility. For the fourth quadrant, it is noticeable that

all the models from μ_Δ=2 (CDR=4.01%) on over-estimate the ductility capacity of the test specimen.

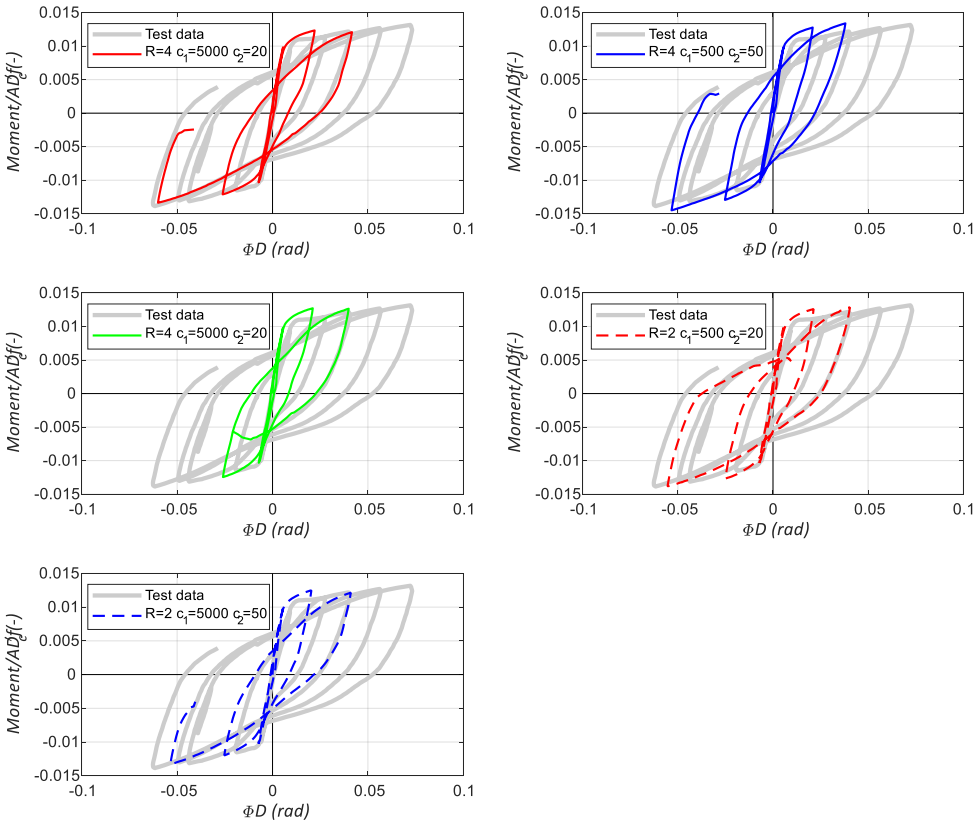

Figure 6–48: Comparison of normalized moment-curvature at the PH region, for M-P parameters values.

Figure 6–49 shows the first two cycles of the normalized moment curvature, with the yielding curvature given by Priestley's formulation. All the models agree well with the prediction given by Priestley's prediction, but this does not fit with the specimen behavior for the positive cycles.

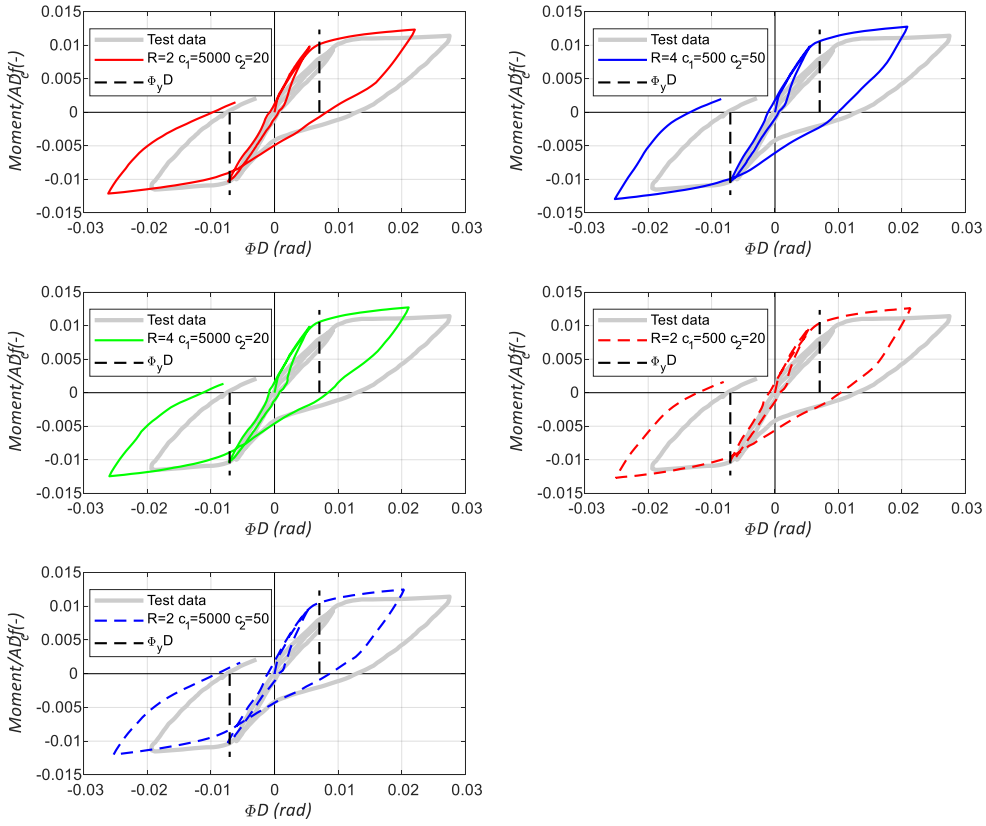

Figure 6–49: First cycles of normalized moment-curvature, for different M-P parameters.

Figure 6–50 presents the normalized moment-rotation at the shaft-column interface. From the figure, it is clear that the reinforcement in this region plays a significant role in the prediction of the behavior. In Chapter 3.2 the author compared the stress-strain curve for a bar with the parameters presented here. The one that gave a wider loop (R=4 c_1=500 c_2=50) is the one that offers the more full loop for the response.

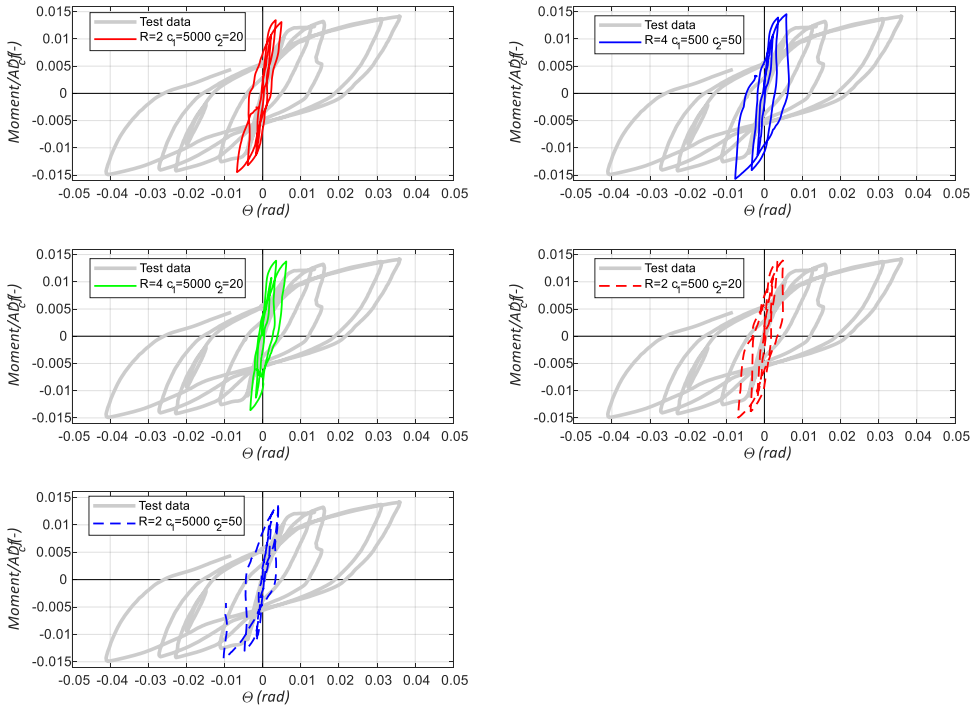

Figure 6–50: Normalized moment-rotation at the shaft-column interface, for different M-P parameters.

Figure 6–51 gives the lateral displacement contribution of each region of the test specimen as well as the predicted by the models. Table 6-26 presents the values in percentages shown in the figure. It is clear that all the models under-estimate the rotation at the interface between the shaft and the column. The model that gives a better agreement on the distribution of the displacement is Model 1.

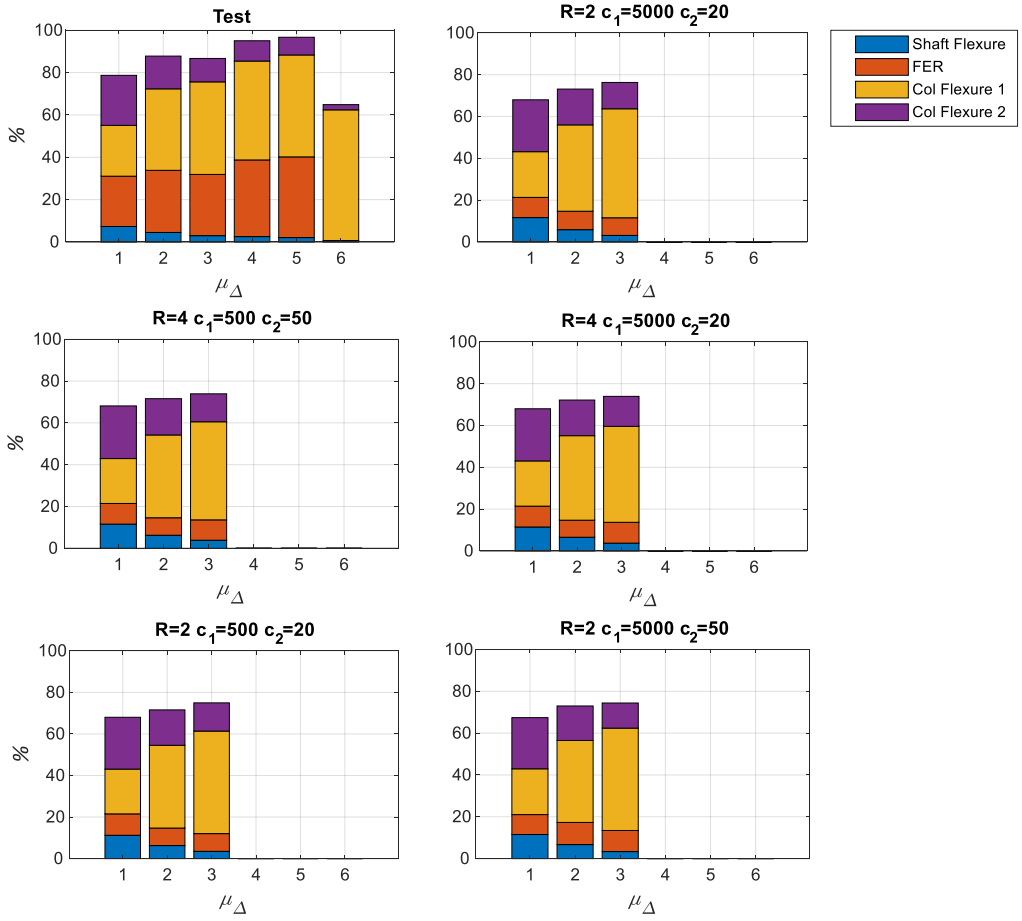

Figure 6–51: Lateral displacements contribution calculated for test specimen and thorough analysis for different M-P parameters.

Table 6-25: Displacement contributions in %, for different M-P parameters.

	R=4 c_1=500 c_2=50			M/Test			R=4 c_1=5000 c_2=20			M/Test		
CDR (%)	1.98	4.01	6.64	1.98	4.01	6.64	1.98	4.01	6.64	1.98	4.01	6.64
μ_Δ	1	2	3	1	2	3	1	2	3	1	2	3
Shaft	11.6	6.25	3.86	1.58	1.39	1.3	11.5	6.55	3.732	1.57	1.46	1.25
FER	9.88	8.36	9.73	0.42	0.28	0.34	9.97	8.16	9.959	0.42	0.28	0.34
Col1	21.5	39.6	46.9	0.89	1.03	1.07	21.6	40.4	45.91	0.9	1.05	1.05
Col2	25.2	17.4	13.4	1.07	1.12	1.21	24.9	17	14.35	1.06	1.10	1.30

Table 6-26: Displacement contributions in %, for different M-P parameters.

	R=2 c1=500 c2=20			M/Test			R=2 c1=5000 c2=50			M/Test		
CDR (%)	1.98	4.01	6.64	1.98	4.01	6.64	1.98	4.01	6.64	1.98	4.01	6.64
μ_Δ	1	2	3	1	2	3	1	2	3	1	2	3
Shaft	11.2	6.26	3.48	1.53	1.39	1.17	11.5	6.7	3.3519	1.58	1.49	1.13
FER	10.3	8.43	8.53	0.43	0.29	0.29	9.53	10.6	10.091	0.4	0.36	0.35
Col1	21.6	39.8	49.4	0.9	1.04	1.13	21.9	39.2	48.959	0.91	1.02	1.12
Col2	24.9	17	13.6	1.06	1.1	1.23	24.5	16.5	12.021	1.04	1.07	1.09

6.2.2 Activation of reinforcement in compression

ATENA provides a manual activation of the rebar in compression. Assessment of the activation is presented. Table 6-27 shows the time that the models took to process. The program was able to run into further steps by activating the compression.

From Figure 6–52, it is clear that there is no considerable change in the overall behavior considering or not the compression, for this displacement ductility range.

Table 6-27: Activation of compression models and run time.

Model	Modifications	Run Time [hrs.]	Last Step	Run Time [hrs.] @ 300 steps
M1	Compression activated	10.75	427	7.27
M2	Compression not activate	14.42	410	10.63

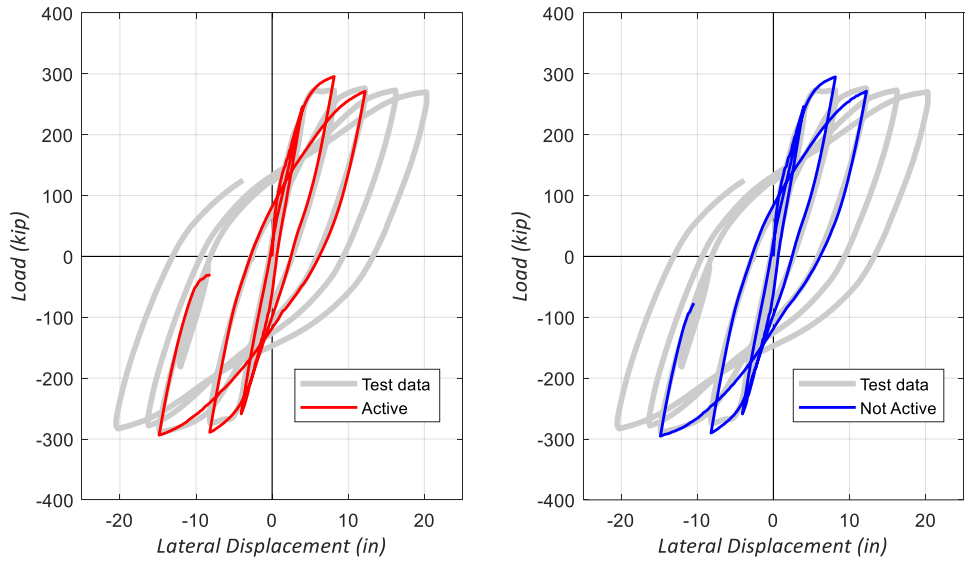

Figure 6–52: Comparison of curve load versus lateral displacement, for active/inactive rebar compression.

Figure 6–53 shows the normalized moment-curvature graph. By not activating the compression, there is a slight reduction in energy dissipation (2%) at the third displacement ductility cycle. Figure 6–54 shows the first two cycles of the normalized moment-curvature with the yield curvature given by Priestley's formulation. There is no change in the predictions of the models at this stage. Also, both models agree well with the yielding curvature provided by Priestley and fail to predict the flexibility at the positive first cycles of the test specimen.

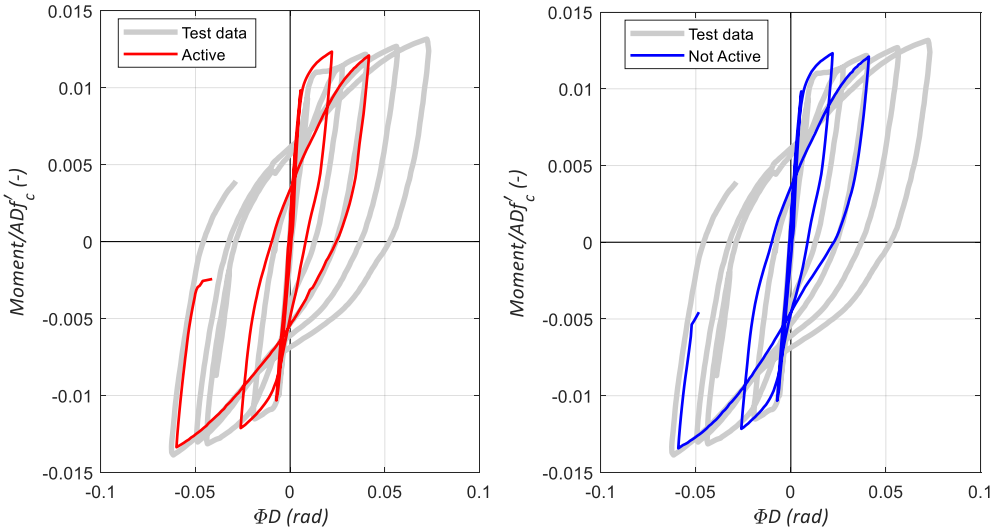

Figure 6–53: Comparison of normalized moment-curvature at PH region, for active/inactive rebar compression.

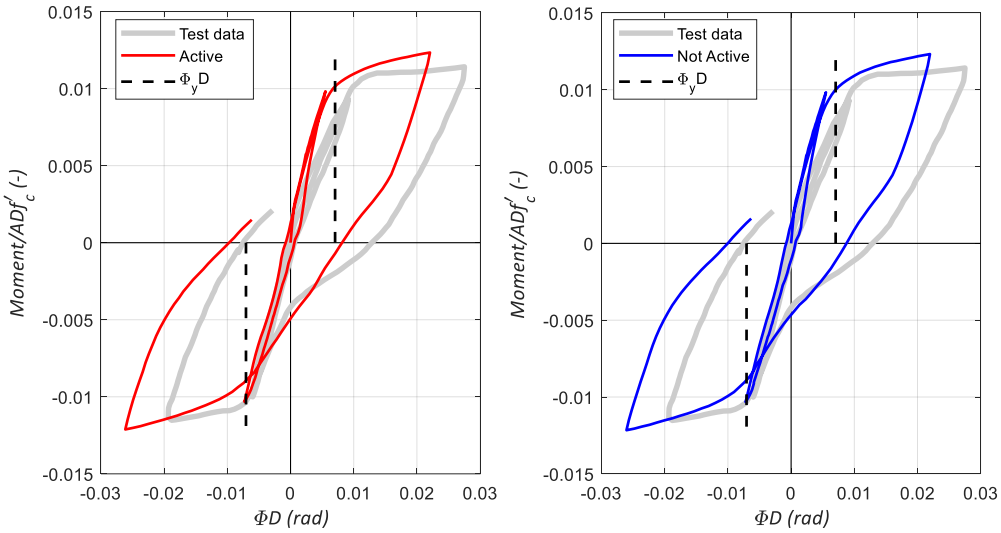

Figure 6–54: First cycles of normalized moment-curvature at PH region, for active/inactive rebar compression.

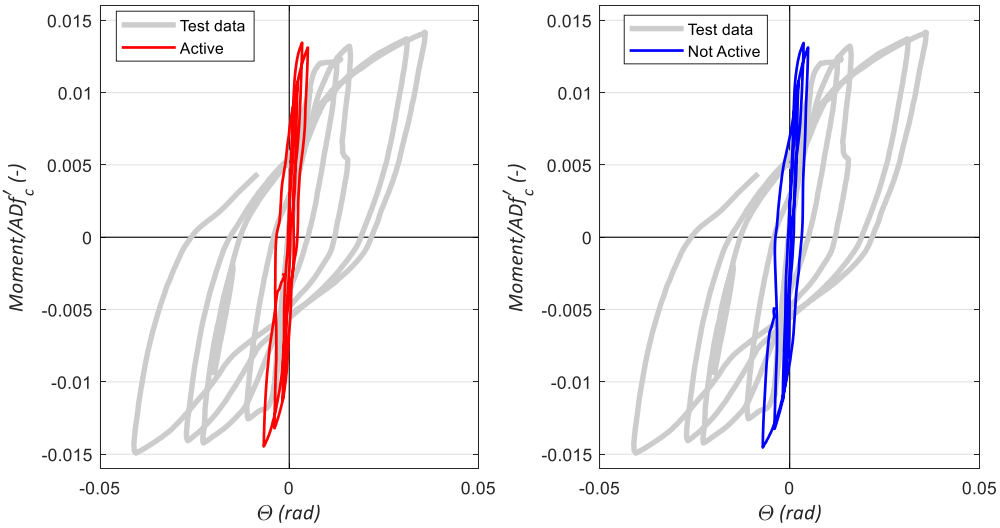

Figure 6–55: Normalized moment-rotation at shaft-column interface, for active/inactive rebar compression.

Figure 6–55 presents the normalized moment-rotation at the shaft-column interface. The activation of the parameter does not change the behavior of this region at this level of displacement regarding the peak values of strength and rotation capacity. At μ_Δ=3 (CDR=6.64%) the loop given by the model without the activation of the compression provides a fuller loop.

From Figure 6–56 and Table 6-28, it is clear that there is no significant change in the results by activating or deactivating the compression on the rebar. However, since it gives a slight improvement in the contribution of the displacement at the fixed end rotations, it is advisable to consider it.

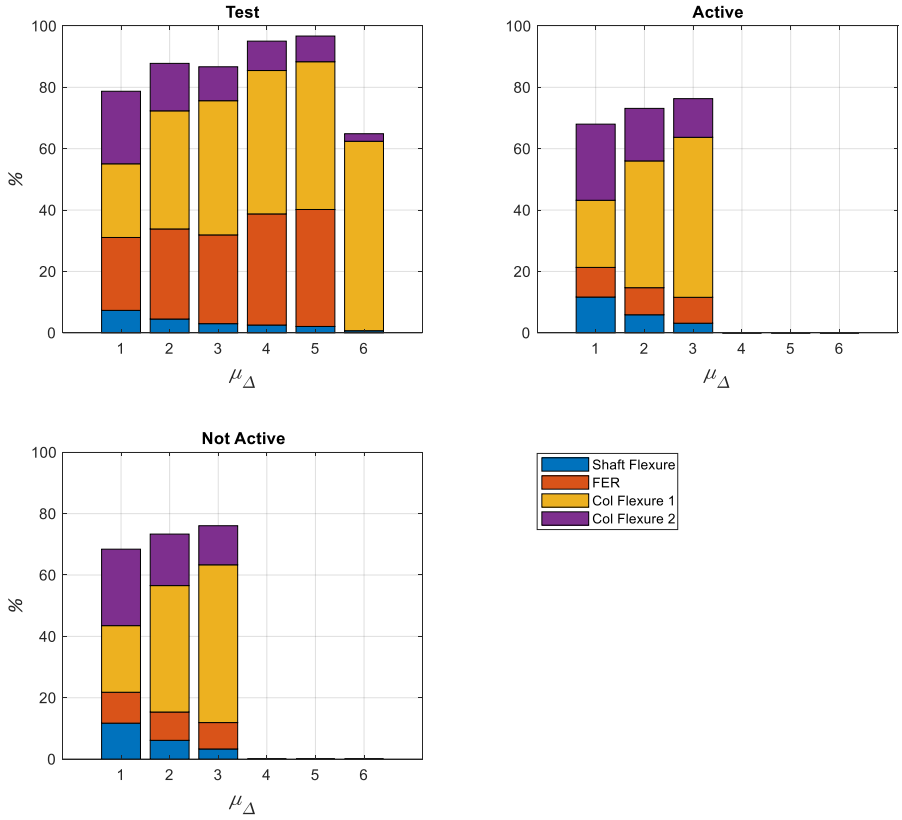

Figure 6–56: Lateral displacements contribution calculated for test specimen and thorough analysis for active/inactive rebar compression.

Table 6-28: Displacement contributions in %, for active/inactive rebar compression.

	Compression inactive			M/Test			Compression active			M/Test		
CDR (%)	1.98	4.01	6.64	1.98	4.01	6.64	1.98	4.01	6.64	1.98	4.01	6.64
μ_Δ	1	2	3	1	2	3	1	2	3	1	2	3
Shaft	11.7	6.12	3.31	1.60	1.36	1.11	11.7	5.87	3.1295	1.59	1.31	1.05
FER	10.1	9.23	8.6	0.42	0.31	0.30	9.66	8.82	8.437	0.41	0.3	0.29
Col1	21.7	41.2	51.4	0.90	1.07	1.18	21.9	41.3	52.14	0.91	1.07	1.19
Col2	24.9	16.8	12.7	1.05	1.09	1.15	24.8	17.1	12.603	1.05	1.11	1.14

6.2.3 Bond-Slip Law

Reviews of three bond-slip laws are presented, i.e., user-defined, CEB-FIP code and Bigaj(1999) (see Chapter 3.2). For the user-defined law change in the maximum bond strength and friction unloading parameter was made, as established in Table 6-29.

Table 6-29: User Defined Laws used.

	Max Bond Strength [psi]	Friction Unloading [psi]
Memory bond user-defined law 1a	1000	50
Memory bond user-defined law 1b	2200	50
Memory bond user-defined law 1c	1000	200

Table 6-30 presents the models and the time that the analysis took. The fastest process was the one with Bigaj (1999) bond-slip law.

Table 6-30: Bond-Slip models and run times.

Model	Modifications	Run Time [hrs.]	Last Step	Run Time [hrs.] @ 300 steps
M1	Memory bond user-defined law 1a (BS1a)	10.75	427	7.27
M2	Memory bond user-defined law 1b (BS1b)	14.37	361	11.06
M3	Memory bond user-defined law 1c (BS1c)	14.42	407	11.06
M4	Memory bond CEB-FIP law	15.13	383	11.17
M5	Memory bond Bigaj (1999).	9.88	415	7.16
M6	Fixed bar	15.88	420	9.33

Figure 6–57 shows the overall behavior predicted by the models with different bond-slip laws and the results from the test specimen. The prediction fits well the response; however, it is

not capable of capturing the opening and closure of the flexural cracks. The curve is not affected by the change in the parameters of the bond slip at this displacement level.

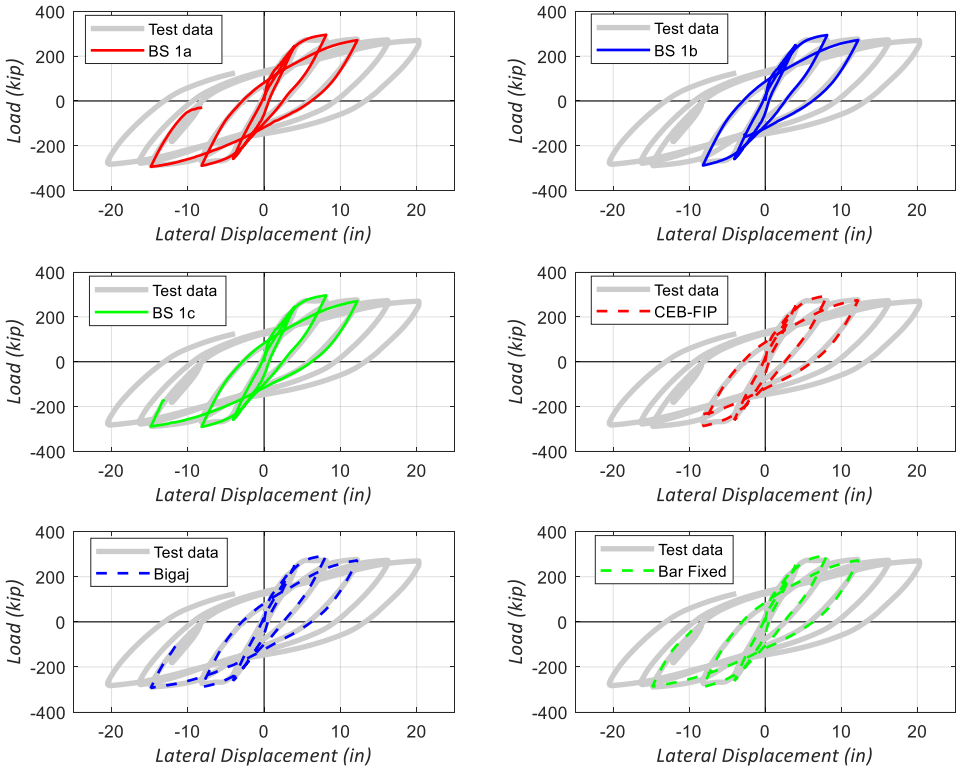

Figure 6–57: Comparison of curve load versus lateral displacement, for different bond-slip laws.

Figure 6–58 displays the comparison of the normalized moment-curvature for the plastic hinge region. For the first two ductility cycles, the models predict the same behavior. For the third displacement cycle, the base model (BS 1) is the one that predicts the higher ductility at the negative peak displacement (38% of error), the models that predict the lower ductility are BS1c, Bigaj and fixed bar with 26% of error.

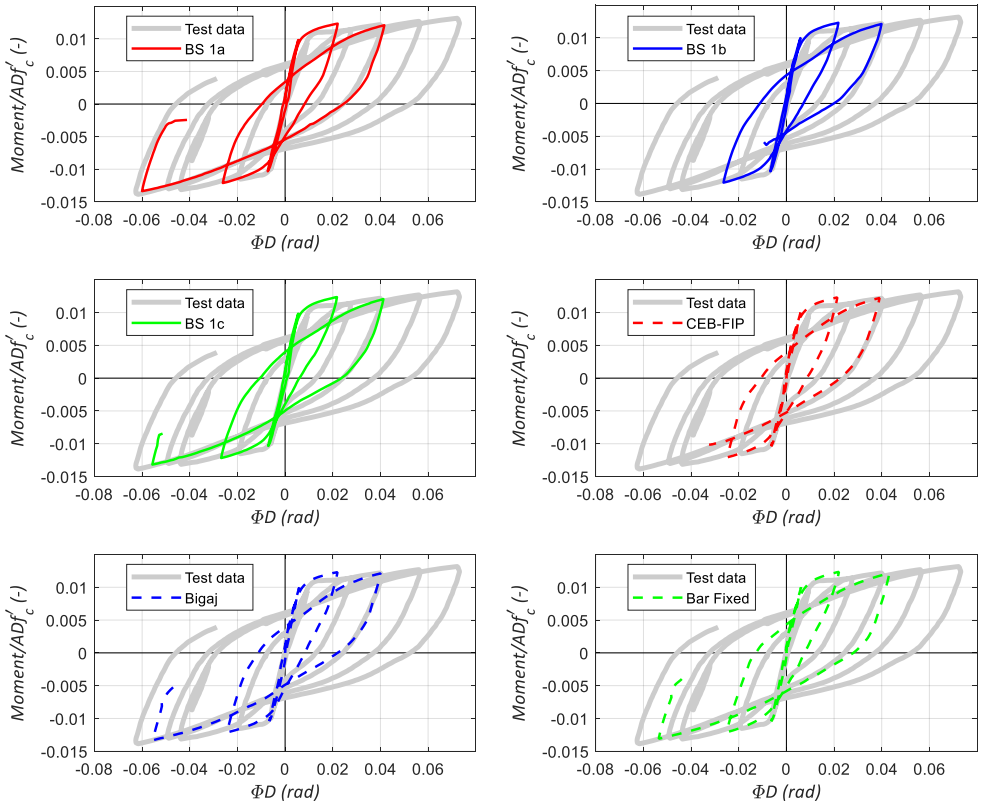

Figure 6–58: Comparison of normalized moment-curvature at PH region, for different bond-slip laws.

Figure 6–59 shows the first two cycles of the normalized moment-curvature at the plastic hinge region, with the yield curvature predicted by Priestley (2003). The models give a good correlation with the prediction of Priestley, but for the positive cycle, the structure is more flexible, which leads to higher yield ductility.

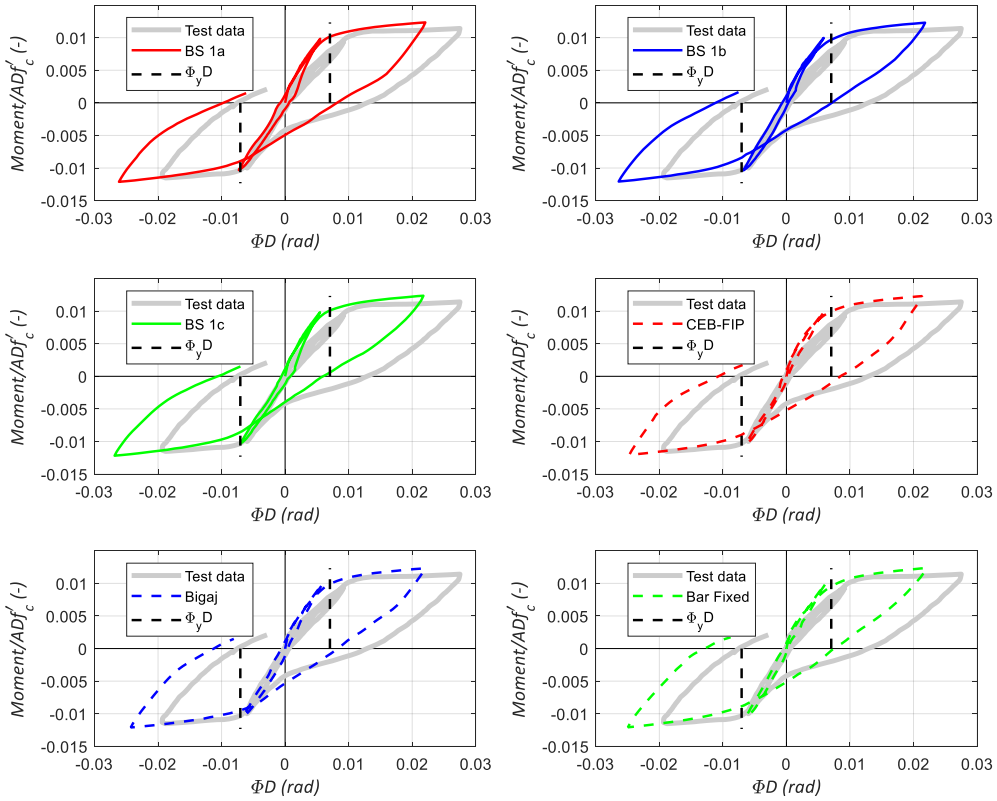

Figure 6–59: First cycles of normalized moment-curvature at PH region, for different bond-slip laws.

Figure 6–60 presents the normalized moment-rotation at the shaft-column interface. The model that gives the higher energy dissipation is BS1b. Increasing the friction parameter in the user-defined bond-slip law provides a higher rotation capacity at the end of μ_Δ=3 (CDR=6.64%). From these curve the one that fits better is BS1c.

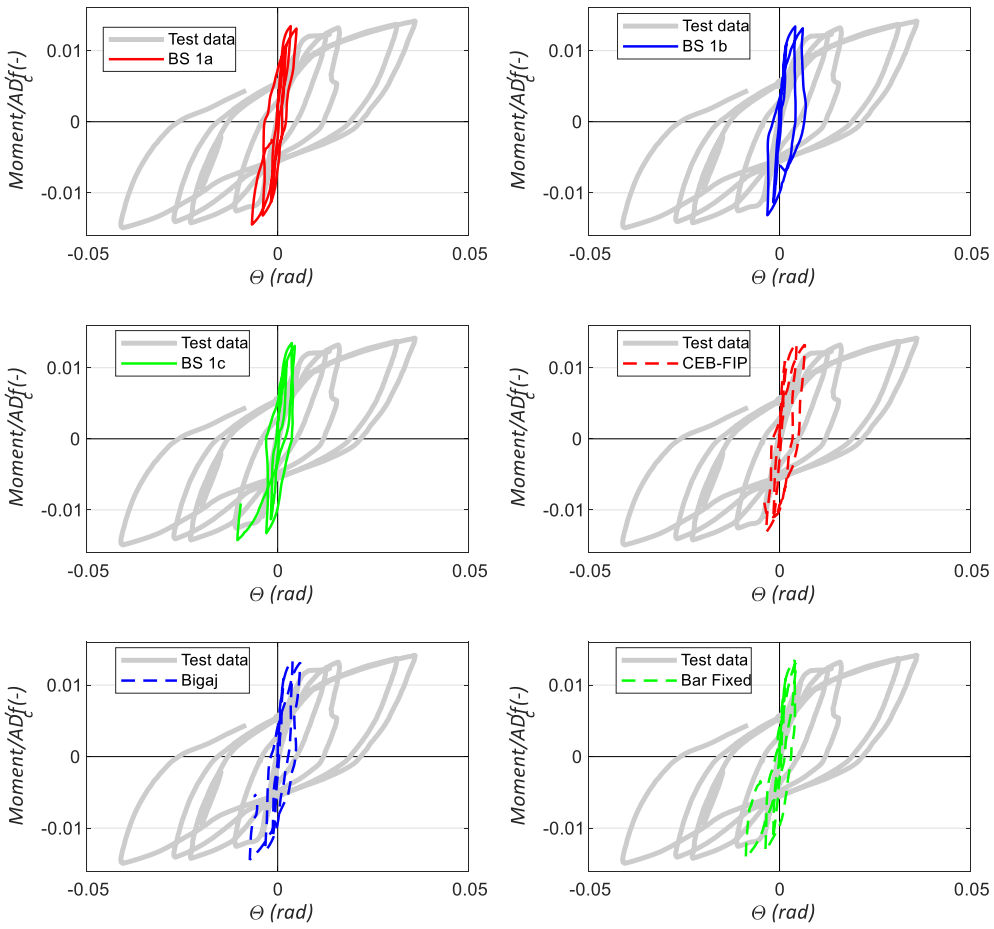

Figure 6–60: Normalized moment-rotation at the shaft-column interface, for different bond-slip laws.

Figure 6–61 displays the displacement distribution over the height of the specimen. Moreover, in Table 6-31 through Table 6-33, the percentage of the contribution of the total displacement by the regions of the test specimen is provided. From the figure, the bond-slip model that offers the best prediction for the displacement contribution of the shaft-column interface is BS1c.

After a review of the results, the author recommends the use of the model BS1c.

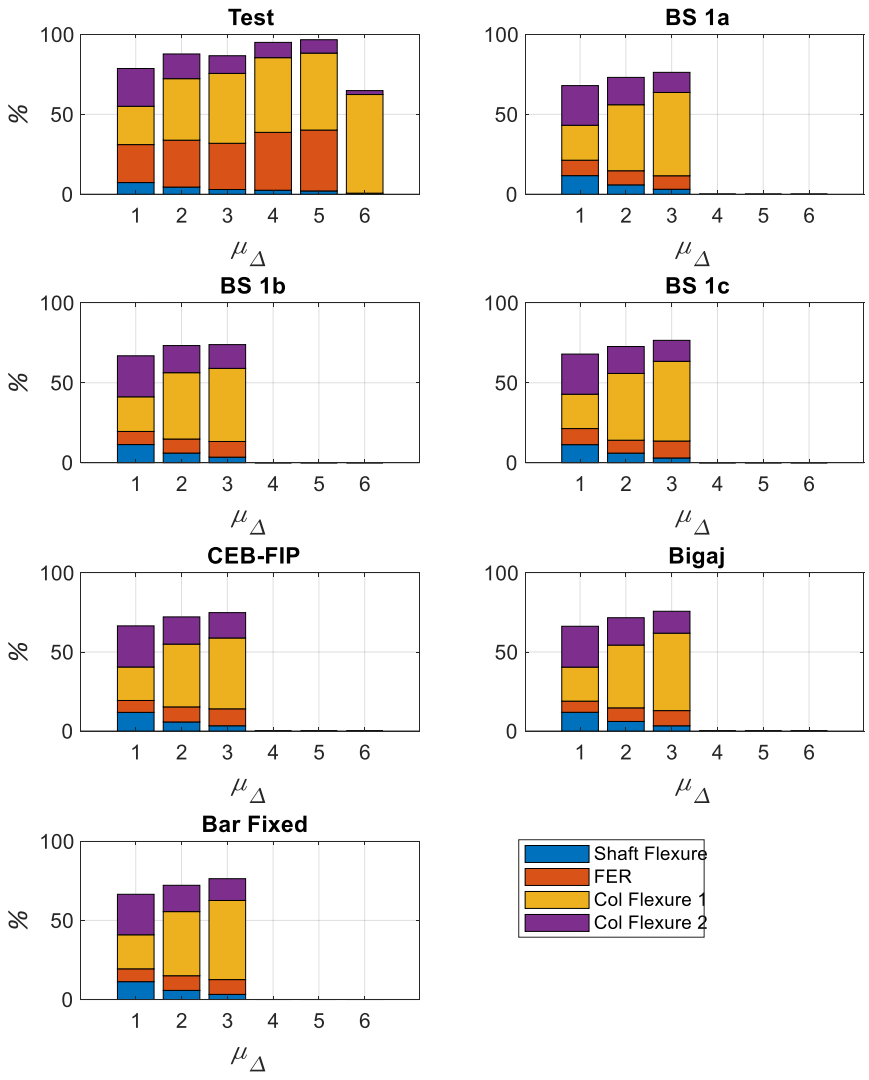

Figure 6–61: Lateral displacements contribution calculated for test specimen and thorough analysis for different bond-slip laws.

Table 6-31: Displacement contributions in %, for different bond-slip laws.

	BS 1b			M/Test			BS 1c			M/Test		
CDR (%)	1.98	4.01	6.64	1.98	4.01	6.64	1.98	4.01	6.64	1.98	4.01	6.64
μ_Δ	1	2	3	1	2	3	1	2	3	1	2	3
Shaft	11.3	6.0	3.4	1.55	1.34	1.16	11.3	6.0	2.9	1.54	1.34	0.99
FER	8.2	8.8	9.8	0.35	0.30	0.34	10.1	8.1	10.6	0.42	0.27	0.37
Col1	21.7	41.5	45.8	0.90	1.08	1.05	21.5	41.8	49.9	0.90	1.09	1.14
Col2	25.7	17.0	14.9	1.09	1.10	1.34	25.1	16.9	13.1	1.06	1.09	1.19

Table 6-32: Displacement contributions in %, for different bond-slip laws.

	CEB-FIP			M/Test			Bigaj			M/Test		
CDR (%)	1.98	4.01	6.64	1.98	4.01	6.64	1.98	4.01	6.64	1.98	4.01	6.64
μ_Δ	1	2	3	1	2	3	1	2	3	1	2	3
Shaft	11.8	5.8	3.4	1.62	1.29	1.13	11.9	6.1	3.3	1.63	1.36	1.12
FER	7.5	9.5	10.7	0.32	0.32	0.37	7.1	8.6	9.6	0.30	0.29	0.33
Col1	21.2	39.7	44.8	0.88	1.03	1.02	21.5	39.7	49.0	0.90	1.03	1.12
Col2	26.0	17.2	16.0	1.10	1.11	1.45	25.8	17.3	13.8	1.09	1.12	1.25

Table 6-33: Displacement contributions in %, for different bond-slip laws.

	Fixed Bar			M/Test		
CDR (%)	1.98	4.01	6.64	1.98	4.01	6.64
μ_Δ	1	2	3	1	2	3
Shaft	11.3	5.76	3.23	1.54	1.28	1.08
FER	8.12	9.27	9.36	0.34	0.32	0.32
Col1	21.5	40.5	50	0.90	1.05	1.14
Col2	25.6	16.6	13.8	1.08	1.08	1.24

6.3 SUMMARY

Activating the tension stiffening (c_{ts}) parameter allows the program to run further into the displacement cycles. A value of 0.6 gave a better fit with the overall as well as the components.

The activation of aggregate interlock, the shear factor and the reinforcement active in compression did not add a better fitting to the response, and it made it, in some cases, harder to converge. This is also the case of modifying the fracture energy.

The unloading factor set to zero capture some opening and closure effect; however, it is minor in comparison to the c_{ts} parameter. Considering that the concrete can contract (β) also provided some necking into the hysteresis.

For cyclic analysis, the author advises using a rotated crack model instead of a fixed-crack model, since the latest has convergence issues at an early stage.

Accounting for a reduction in the compressive strength due to cracking (Fc) as 0.6 provided a better fit of the strength at the peak displacements of the second and third cycles.

Using a critical compression value of -0.0295 in. rather than -0.197 in. provides a better agreement on the overall curve for the first two cycles, but it shortens the steps that the program can run before experiencing convergence problems.

For the Menegotto-Pinto (M-P) settings, the values used in the base model gives a reasonable match. The M-P has an impact on the response of the fixed end rotation region. For the bond-slip law considering a user-defined law with a maximum bond strength of 1 ksi and unloading friction of 200 psi gave a well fit. However, the maximum bond strength provided is lesser than the value found by Lotfizadeh (2019) on his research.

The model that gave a better fit in the overall behavior and the local behavior was the base model with the tension stiffening active set as 0.6. The strains at the peak displacements of the most north and most south bar of the column were obtained from the model, and are presented in Figure 6–62 and Figure 6–63. B1 corresponds to the bar at the north that is shown with a continuous line, and B3 is the bar at the south shown with a segmented line. In black, line the experimental data measured with electrical foil strain gauges for these bars is displayed. Also, in red are the base model strains and in blue the model that fits best.

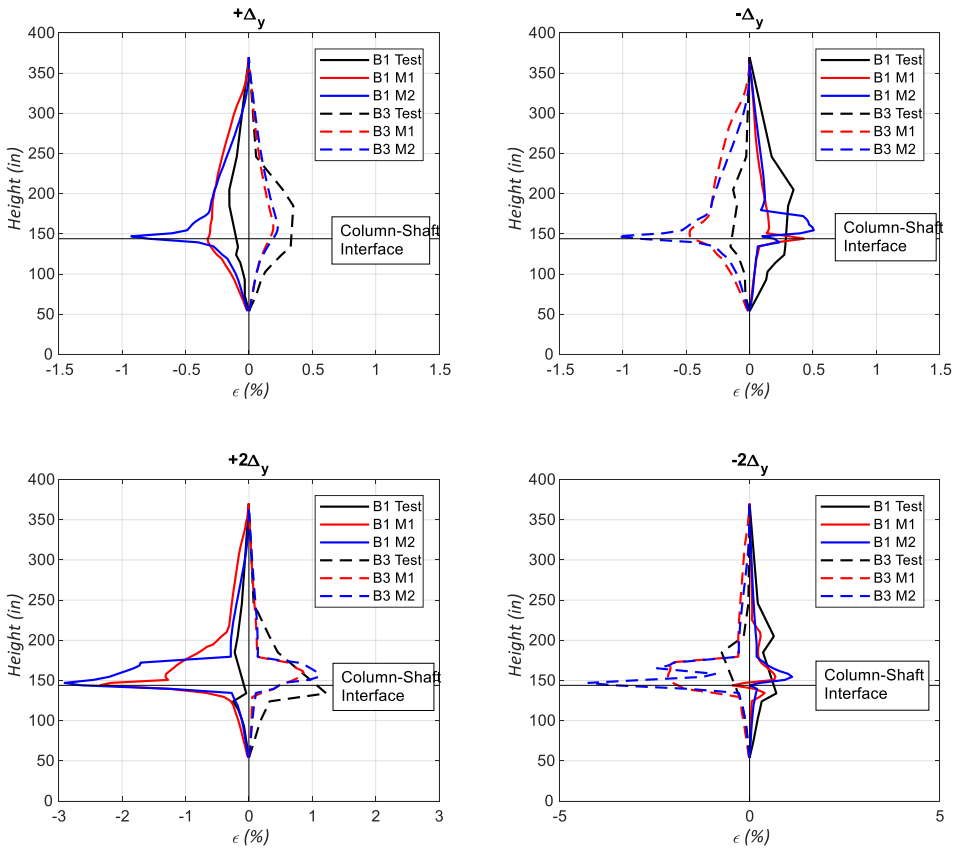

Figure 6–62: Strain distribution over height at peak displacements.

For the first cycle, in the positive loading direction, the tensile strains in bar 3 in the test specimen are higher than the predicted. For the bar that is under compression (bar 1), the models

predict higher strains. For the second cycle, in the positive loading direction, the models predict localization of the plasticity for both bars, which in the test was more noticeable for the bar in tension. In the negative direction, the localization in compression strain predicted by the models is higher than the seen in the tests. For the third cycle in the positive loading direction, the models gave a relatively good fit. However, for the negative direction, the test results show negative strains for the bar under tension which the models predicts not in magnitude but the change of sign.

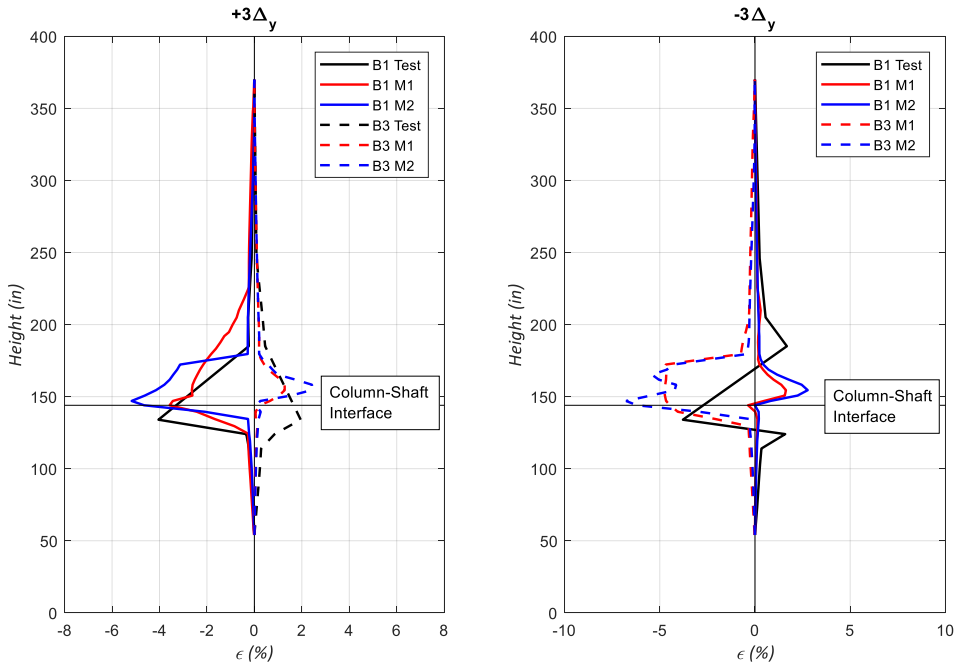

Figure 6–63: Strain distribution over height at peak displacements.

CONCLUSIONS

This thesis describes the calibration and validation of a detailed nonlinear finite element model of a reinforced concrete Type II shaft built at full scale and tested by Lotfizadeh (2019) in the Charles Lee Powell Structural Research Laboratories. ATENA was the computer software of choice used throughout in this work with the concrete modeled with a fracture-plasticity constitutive model available in the library of constitutive material relationships in this software.

An extensive parametric work was carried out to calibrate the model. Computed overall lateral displacement-lateral deflection responses and local normalized moment-normalized curvature and normalized moment and column fixed-end were compared with experimental measurements reported by Lotfizadeh (2019).

One of the greatest difficulties observed in the computational work is convergency. Many models ran partially and then stopped converging. Convergence problems were acute when using a fixed-crack model.

This research successfully predicted the overall response of the test specimen, and predicted well some local responses but felt somewhat short in reproducing accurately the fixed-end rotation at the column to shaft interface due to bar bond slip (strain penetration) of the column longitudinal bars which where lap-spliced with the pile longitudinal reinforcement via a non-contact lap-splice.

BIBLIOGRAPHY

A706/A706M-16, A. (2016). *Standard Specification for Deformed and Plain Low-Alloy Steel Bars for Concrete Reinforcement.* A706/A706M-09b, West Conshohocken, PA.

Bigaj, A. J. (1999). Chapter 4 Bond of Ribbed Bars in Concrete. In A. J. Bigaj, *Structural Dependence of Rotation Capacity of Plastic Hinges in RC Beams and Slabs.* the Netherlands: Delft University Press.

Caltrans. (2006). *Seismic Design Criteria.* Sacramento: Caltrans.

CEB-FIP. (1990). *CEB-FIP Model Code 1990 Design Code.* Trowbridge, Wiltshire: Redwood Books.

Cervenka, J., Cervenka , V., & Laserna, S. (2018). On Crack Band Model in Finite Element Analysis of Concrete Fracture in Engineering Practice. *Engineering Fracture Mechanics*, 27-47.

Cervenka, J., Cervenka, V., & Laserna, S. (2014). On Finite Element Modeling of Compressive Failure in Brittle Materials. In *Computational Modelling of Concrete Structures Volume I* (pp. 273-281). Ed. Bicanic, Mang, Meschke , de Borst CRC Press.

Cervenka, V., Cervenka, J., Pukl, R., & Sajdlova, T. (2016). Prediction of shear failure of large beam based on fracture mechanic. *9th International Conference on Fracture Mechanics of Concrete and Concrete Structures*.

Cervenka, V., Jendele, L., & Cervenka, J. (2018). *ATENA Program Documentation, Part 1, Theory.* Prague: Cervenka Consulting, January 26, 2018.

Collins , M., & Mitchell, D. (1991). *Prestressed Concrete Structures.* Englewood Cliffs NJ: Prentice Hall.

Consulting, C. (n.d.). ATENA Studio 32bit.

Havlásek, P., & Kabele, P. (2017). *A Detailed Description of the Computer Implementation of SHCC Material Model in OOFEM.* Prague, Czech Republic: Czech Technical University in Prague.

Hordijk, D., & Reinhardt , H. (1991). *Local Approach to Fatigue of Concrete.* Netherlands: Dissertation , Delft University of Technology.

Kupfer, H., Hilsdorf, H., & Rusch, H. (1969). Behavior of Concrete under Biaxial Stresses. *ACI Journal, Title no66-52, August 1969*, 656-666.

Lotfizadeh, K. (2019). *High-Strength Steel Reinforcement in Critical Regions of Earthquake-Resistant Bridges.* in preparation.

Mander, J., Priestley, M., & Park, R. (1988). Observed Stress-Strain Behavior of Concrete. *Journal of Structural Engineering, Vol 114 No8, August 1988*, 1827-1849.

Menegotto, M., & Pinto, P. (1973). Method of analysis of cyclically loaded RC plane frames including changes in geometry and non-elastic behavior of elements under normal force and bending. . *Preliminary Report IABSE, vol 13*.

Menetrey, P., & Willam, K. J. (1995). Triaxial Failure Criterion for Concrete and its Generalization. *ACI Structural Journal, Title no 92-S30*, 311-318.

Moharrami, M., & Koutromanos, I. (2017). Finite Element Analysis of Damage and Failure of Reinforced Concrete Members under Earthquake Loading. *Earthquake Engineering and Structural Dynamics*, 46: 2811-2829.

Murcia-Delso, J. (2013). *Bond-Slip Behavior and Development of Bridge Column Longtudinal Reinforcing Bars in Enlarged Pile Shafts.* San Diego: Dissertation, University of California San Diego.

Nakamura, H., & Higai, T. (2001). Compressive Fracture Energy and Fracture Zone Length of Concrete. *ASCE*, 471-487.

Officials, A. A. (2010). *AASHTO LRFD Bridge Design Specifications.* Washington DC: American Association of State Highway and Transportation Officials.

OpenSees, M. F. (2013). Open system for earthquake engineering simulation. . *Pacific Earthquake Engineering Research Center, University of California Berkeley, CA.*

Priestley, M. (2003). *Myths and Fallacies in Earthquake Engineering,Revisited The Ninth Mallet Milne Lecture.* Pavia, Italy: Rose School.

Rashid, J., Dameron, R., & Dowell, R. (2000). RECENT ADVANCES IN Concrete Material Modeling and Application to the Seismic Evaluation and Retrofit of California Bridges. *12WCEE*.

Test 670, C. (2013). *Method of Tests for Mechanical and Welded Reinforcing Steel Splices.* California Test Methods.

Van Mier, J. (1984). *Strain-Softening of Concrete under Multiaxial Loading Conditions.* Eidhoven, The Netherlands: Dissertation, Eindhoven University of Technology.

Van Mier, J., Shah , S., Arnaud, M., Balaysaac, J., Bascoul, A., Choi, S., et al. (1997). Strain-Softening of Concrete in Uniaxial Compression. In *RILEM Technical Committees: Materials and Structures , Vol, 30 May 1997* (pp. 195-209). RILEM.

Vos, E. (1983). *Influence of Loading Rate and Radial Pressure on Bond in Reinforced concrete - A Numerical and Experimental Approach.* Delft University Press.